HIGH PRECISION OPTICAL INTERFEROMETRY
AND
APPLICATION TO BE STARS

by

Christopher Tycner

A thesis submitted in conformity with the requirements
for the degree of Doctor of Philosophy,
Graduate Department of Astronomy & Astrophysics,
University of Toronto

High Precision Optical Interferometry and Application to Be Stars

Doctor of Philosophy, 2004
Christopher Tycner
Graduate Department of Astronomy and Astrophysics
University of Toronto

Abstract

A new technique for calibrating optical long-baseline interferometric observations is developed where both the calibration corrections and the source characteristics are obtained from the observations of a program star. This calibration technique can only be applied to certain classes of objects, such as emission line sources or binary systems, where the parameters describing the characteristics of the source have different functional dependence than the calibration parameters. To demonstrate its effectiveness, the technique is applied to observations of four different Be stars obtained with the Navy Prototype Optical Interferometer. The interferometric observations utilize measurements obtained simultaneously in many spectral channels covering a wide spectral range, where only two channels contain a strong signal due to the circumstellar envelope in the Hα emission line. The calibrated observations in Hα allow modeling of the circumstellar envelopes of all four stars with circularly symmetric and elliptical Gaussian models. The best-fit model parameters are then combined with similar results for other Be stars, already published in the literature, to study the relationship between the Hα emission and the physical extent of the Hα-emitting circumstellar region. For the first time, a clear dependence of the net Hα emission on the extent of the circumstellar region is demonstrated. These results are consistent with an optically thick line emission that is directly proportional to the effective area of the emitting disk. Within the small sample of stars considered in this analysis, no clear dependence on the spectral type or stellar rotation is established, although the results do suggest that hotter stars might have more extended circumstellar regions.

To my family

A man is a small thing,
and the night is very large
and full of wonders.

— Lord Dunsany “The laughter of the gods”

Acknowledgments

This dissertation is dedicated to my family, whom I owe the greatest debt of gratitude. To my parents Aleksandra and Stefan, for valuing education and for the unconditional support I receive from them until this day. To my wife Karina, whose love, patience, guidance and unwavering support have not only carried me throughout my undergraduate and graduate studies, but kept me focused, motivated and most of all happy — I could not have done it without her. To my daughter Jennifer, for the inspiration and for reminding me of the little things in life. To my sister Joanna, for watching out for me since the "beginning", and my brother Slavek, for the first astronomy book that helped me decide who I want to become when I grow up. To the rest of the family and friends, I send a heartfelt thank you for being there for me whenever I needed them.

It has been a great privilege to work under the supervision of John Lester, whose enthusiasm for research and teaching inspired me throughout my graduate studies. I would also like to thank John Lester for creating a supportive research environment for me and for introducing me to the field of optical interferometry. I wish to thank the members of my committee, Tom Bolton and John Percy, who overlooked the progress of this thesis. Special thanks to Tom Bolton for the long discussions on hot stars and stellar winds, and to John Percy who has helped me foster my love for teaching astronomy.

Without the generous assistance of Arsen Hajian it would not have been possible to complete this thesis. Arsen has not only supported the work presented in this dissertation from the inception of the original ideas, but played a major role as a guide, source of knowledge and encouragements, and whenever necessary being simply a friend. For the endless hours spent talking to me over the phone and answering my e-mails, for making me feel so welcome during my stays at the USNO, offering a simple thank you is an understatement.

This thesis has greatly benefited from productive discussions with Dave Mozurkewich, Tom Armstrong, Charmaine Gilbreath, Tom Pauls, Don Hutter, and Jim Benson. I also wish to thank my first mentor, David F. Gray, for introducing me to the world of astronomical research. Many thanks to my fellow graduate students, especially to my office-mate Arno Dirks, who always listened when I had something to say. To those I have not explicitly mentioned, I offer my apologies and my thanks.

This work was funded by NSERC, the Department of Astronomy and Astrophysics at the University of Toronto, the Government of Ontario Graduate Scholarship fund in Science and Technology, and the Walter C. Sumner Fellowship Foundation.

Table of Contents

List of Tables

List of Figures

Chapter 1

Introduction

Over the years, numerous observational and theoretical studies have shown that nearly all stars lose mass in the form of stellar winds. Although the details associated with the wind formation can be quite different from one star to another, and could involve a number of different physical processes, the most common driving force is that due to the stellar radiation field. In fact, the radiation alone can be responsible for driving the stellar wind as the photon momentum is absorbed by the outflowing material. In cool stars, where the conditions in the wind are cool enough for dust to form, the photons are absorbed by the dust particles, and in the case of hotter stars the photon momentum is transferred to the wind by excitation of the atomic gas, resulting in what is known as line-driven wind.

Among the B-type stars, which have effective temperatures in the range of 10,000 to 30,000 K, there exists a very interesting class of stars that possess circumstellar regions with much higher densities than expected for line-driven winds of stars of similar effective temperatures and masses. These stars are known as *Classical Be Stars*, or Be stars for short, and although these stars have been studied for more than a century, many unresolved issues still exist.

1.1 General Characteristics of Be Stars

The main general characteristic that defines a Be star is that its spectrum shows, or has shown in the past, at least one Balmer line in emission. Typically, the Be notation is reserved for non-supergiant B-type stars with line-emitting circumstellar material. For supergiants that show line emission, a designation of B[e] is used instead. It is sometimes necessary to emphasize the difference between Be stars with circumstellar envelopes that are thought to be formed by an outflowing material and B-type stars with circumstellar regions that are formed by accretion of the surrounding material, as in the case of Herbig Ae/Be stars, or semi-detached (Algol type) binary systems. In such case, the term "classical" Be star is used to explicitly identify Be stars with line-emitting circumstellar regions that are thought to be caused by stellar *decretion* (see also the discussion of this definition in a recent review paper by Porter & Rivinius, 2003).

The discovery of the Balmer emission in the star γ Cassiopeiae by Secchi (1867) marked one of the first documented cases of emission-line stars, as well as the beginning of the study of Be stars. Because of its interesting spectroscopic characteristics, γ Cas was a subject of numerous observational studies since the discovery of its line emission (see Cowley & Marlborough, 1968, and references therein). The discovery of similar systems followed relatively quickly and by now it is known that at least 15% of all non-supergiant B-type stars have Balmer lines in emission (Cote & van Kerkwijk, 1993). Because there are documented cases of normal B-type stars, which over a period of time became Be-type stars with Hα emission, the above fraction is possibly only a lower limit (see also § 1.1.6).

1.1.1 Emission Lines

The Hα emission line is by far the most commonly observed feature in classical Be stars. Other emission lines, particularly those of the remaining Balmer series as well as lines due to Fe II, Si II, O I, and He I can also be detected (Hanuschik, 1987; Saad et al., 2004). The observed equivalent widths (EW) of the metallic emission lines are known to be correlated with the EW of the Hα emission line, which is also known to be the strongest line emission in Be stars (Hanuschik, 1986, 1987). This means that the Hα line is one of the strongest observational indicators for overall emission strength and for detecting any spatial density asymmetries, including possible variability. Therefore, the Hα emission line is of primary interest to many studies, including the one presented here.

The profiles of the Hα emission lines in Be stars are relatively smooth and a spectral resolving power (R) of 50,000 is more than sufficient to resolve all of the intrinsic structure (Hanuschik, 1986). Despite the fact that at high enough resolution no two stars will appear to have exactly the same Hα emission profiles, they still can be described by only few *representative* profiles (Hanuschik et al., 1996). Figure 1.1 shows the schematic representation of the typical Hα profiles observed for Be stars at $R \lesssim 50,000$. These representative profiles can be further

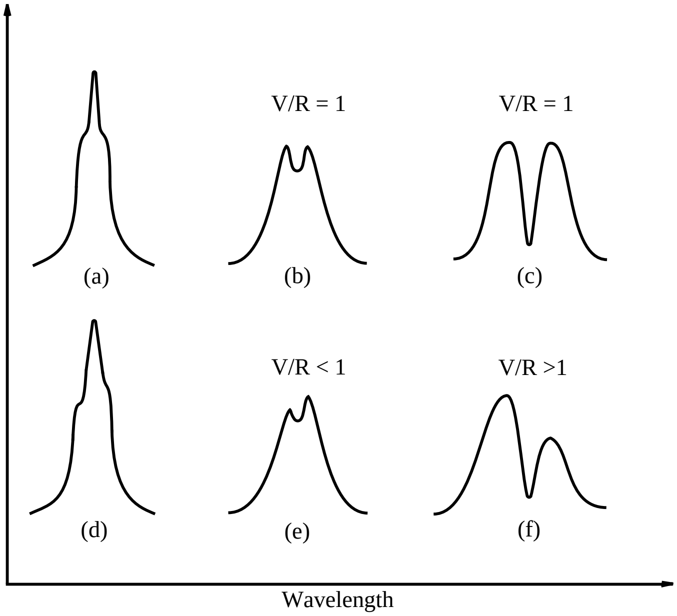

FIGURE 1.1: Schematic representation of the typical Hα emission profiles observed for Be stars at a moderate spectral resolution. Shown are symmetrical (*top*) and asymmetrical (*bottom*) profiles. The wavelength axis is only used to indicate the value of the V/R ratio.

separated into different classes, such as symmetric versus asymmetric profiles, or those that show a clear double-peaked structure and those that do not.

It was first suggested by Struve (1931), who noticed the apparent correlation between the width of the Hα emission line and the stellar projected rotational velocity (i.e., the $v \sin i$ value derived from photospheric lines), that the emission originates from a rotating disk-like envelope and that the difference between the single- and double-peaked profiles can simply be attributed to variations in the inclination angle, i, of star's rotational axis to the line-of-sight. This general idea is now widely accepted, in part due to the more recent modeling of the line radiation transfer in circumstellar disks around hot stars, initially assuming Keplerian orbital motions (Horne & Marsh, 1986), and later extended to other velocity structures and with corrections for the finite size of the central star (Hummel & Vrancken, 2000). The models demonstrated that the transition from a single-peaked to a double-peaked emission profile can be attributed to a changing inclination angle, for both optically thin and thick lines.

The details associated with line formation in the optically thin and thick cases are different, but the general reasoning behind the formation of double-peaked emission can be explained as follows. The double-peaked emission arises because various parts of the disk (with different projected orbital velocities) contribute to different parts of the emission profile, unless the line-of-sight is perpendicular to the disk ($i \approx 0$), in which case the models produce a single-peaked emission profile with a width set by the thermal broadening. More specifically, if the circular Keplerian velocity[1] at the edge of the disk is $v_{\rm K}$, then the line-emission is greatest at wavelengths corresponding to Doppler shifts of approximately $\pm v_{\rm K} \sin i$, which correspond to the largest regions of the disk that have the same projected radial velocities with respect to the line-of-sight (see, for example, Fig. 1 in Horne & Marsh, 1986).

The difference between the optically thin and thick lines arises because in the optically thin case the line photons emitted in the disk can escape easily in all directions, but the optically thick photons are trapped in the disk. Therefore, in the case of optically thick lines, the anisotropic line-emission becomes more important with increasing inclination angles (Horne & Marsh, 1986; Hummel & Vrancken, 2000). This phenomenon is also known as shear broadening and can be explained as the tendency of the photons trapped in the disk to escape in directions along which the Keplerian velocity field provides largest velocity gradients. Therefore, at relatively low inclinations ($10^\circ \lesssim i \lesssim 30^\circ$) both optically thin and thick lines show a similar double-peaked structure with a U-shaped central depression (like the one shown in Fig. 1.1*b*). At intermediate and high inclinations ($i \gtrsim 30^\circ$) the separation of the peaks increases with i, as the projected Keplerian velocity increases, but as the optically thin line retains its relatively shallow U-shaped depression, optically thick lines show a distinct V-shaped depression like the one shown in Fig. 1.1*c* (see also Fig. 4 in Horne & Marsh, 1986). Hummel & Vrancken (2000) argue that this V-shaped depression is not only due to the shear broadening, but that the stellar obscuration of the disk material behind the star and the shell absorption by the material in-front of the star is also important.

Another difference that arises between the optically thin and thick lines, for systems viewed at very low inclinations ($i < 10^\circ$), is that the optically thick emission lines can show distinct inflections on both sides of the emission profile, like the ones illustrated in Figure 1.1*a* (see also Hanuschik, Kozok, & Kaiser, 1988). These extra shoulders in the Hα emission line (also known as the wine-bottle shapes) are explained as being caused by non-coherent scattering in an optically thick disk (Hummel & Dachs, 1992; Hummel, 1994). This can be described as more efficient photon scattering (in the direction perpendicular to the plane of the disk) by the material closer to the star that has higher orbital speed and thus contributes to the flux in the wings of the Hα profile.

---

[1] Circular Keplerian velocity is given by $v_{\rm K} = \sqrt{GM_\star/r}$ where r is the radial distance from the star.

We can conclude that because the strong Hα emission lines typically observed in spectra of Be stars are optically thick, and because they are the strongest line emission, they are excellent probes of the surface emission from the circumstellar disks around Be stars.

1.1.2 UV Lines

Many Be stars show UV absorption lines due to highly ionized metals, an indication of low density, high velocity (700–1100 km/s), superionized wind, which results in an estimated mass loss rate ($\dot{M}$) of approximately $10^{-10} M_{\odot}$ yr^{-1} (Snow, 1981). Although there does not appear to be a clear correlation between $\dot{M}$ and the stellar $v \sin i$ values, systems which are thought to be viewed edge-on, do show much higher density and low velocity outflow (as derived from the emission lines in the optical part of the spectrum; Merrill, 1952), in agreement with the expected disk-like circumstellar envelope.

There also seems to be no correlation between the strength of the Hα emission and the strength of the UV absorption lines. This is commonly interpreted as evidence that the hot stellar wind, responsible for the superionized UV lines, has no direct influence on the higher density circumstellar disk-like envelope (Prinja, 1989). However, there appears to be a connection between the number of the observed discrete absorption component (DACs) in the UV lines and the shape of the Hα emission line (Telting & Kaper, 1994). More specifically, a larger number of DACs is observed whenever a double-peaked Hα emission shows a stronger emission on the violet side. This has been explained as one-armed global density wave (responsible for the asymmetric Hα profile) in the circumstellar disk that causes the column densities of the wind structures responsible for the DACs to be increased (Telting & Kaper, 1994).

1.1.3 Continuum Emission

An IR excess is commonly detected in Be stars. This has been attributed to free-bound and free-free emission from their circumstellar envelopes. This envelope is typically modeled with a circumstellar disk of a fixed radius and opening angle, and where the density distribution as a function of radial distance, r, can be described with

$$\rho(r) = \rho_0 (r/R_\star)^{-n}, \tag{1.1}$$

where $R_\star$ is the stellar radius and ρ_0 is the density at the stellar surface. Based on the IR observations of four Be stars with the IRAS satellite, Waters (1986) obtained values for n in the range of 2.4–3.1, as well as deduced that the circumstellar disks must extend at least 6 to 8 $R_\star$. Waters (1986) also concluded that the matter is very gradually accelerated outwards and that the density in the regions producing the IR excess is much higher than in the regions probed with the UV observations. The mass loss rates derived from the IR observations are in the range of $10^{-8} M_\odot$ yr^{-1} and thus are 50–100 times larger than those derived for the high velocity wind. This is an additional evidence of very different, and perhaps independent, physical conditions in different regions of the winds around Be stars.

1.1.4 The Circumstellar Disk

The observed correlation between the emission line-widths, of both the metallic and Balmer lines, and the $v \sin i$ values derived from the photospheric lines is the strongest spectroscopic evidence for disk-like structure around Be stars (Dachs, Hanuschik, Kaiser, & Rohe, 1986; Hanuschik, 1987, 1996). This correlation can be established using either the FWHM measure of the emission line, or in the case of double-peaked profiles using the separation of the peaks. Because spherical envelopes with predominantly rotational or radial outflow velocity fields would not produce the above correlations, it is now widely accepted that the majority of Be stars possess axisymmetric rotating disk-like envelopes. The detected linear polarization in Be stars also suggests that the circumstellar envelopes are indeed flattened (Quirrenbach et al., 1997).

If double-peaked emission profiles are observed in Be stars they can be used to obtain estimates for the disk radii (Huang, 1972; Hummel, 1994). Although some assumptions need to be made about the state of the disk, like Keplerian versus angular momentum conserving rotation, the typical radii obtained from Hα lines range from a few to tens of stellar radii (Hanuschik, 1986; Hanuschik, Kozok, & Kaiser, 1988). Because metallic emission lines, if detected, are known to be twice[2] as wide as the Hα emission line, the corresponding disk radii derived from the metallic lines are smaller (Hanuschik, 1987). This implies that the metallic emission lines originate in an inner (most likely denser) component of the larger Hα-emitting disk. Similar arguments apply to higher-order Balmer emission lines which are also known to be broader than the Hα emission line (Hanuschik, Kozok, & Kaiser, 1988).

If the circumstellar disk paradigm is accepted for Be stars then the thickness of these disks in the direction perpendicular to the plane of the disk (also referred to as the z-direction)

---

[2] This is not necessarily true for the Hα wings which can be very extended due to broadening by electron scattering (Poeckert & Marlborough, 1979).

becomes an important parameter to investigate. Furthermore, if the disk is in hydrostatic equilibrium,[3] it might be expected that the disk gets thicker with increasing radial distance from the central star, and in such case it might be more appropriate to specify the opening angle of the disk. One way to investigate this issue is to look at systems with large inclination angles ($i > 80°$) so that the material in the disk can absorb the continuum radiation from the central star. For this purpose, the study of Be-shell stars is very valuable since these stars have Hα emission profiles similar to those illustrated in Figure 1.1*c* (or Fig. 1.1*f*), which are thought to be produced when the systems are viewed edge-on. Such systems are also known to show absorption cores embedded into certain emission lines, such as Fe II lines, that go below the stellar continuum level (Hanuschik, 1996). The difference between the Be-shell stars and the more classical Be stars is typically assumed to be due to a geometrical projection effect and not due to different intrinsic properties of the objects.

Hanuschik (1996) measured the fraction of Be-shell stars among the Be stars and assuming random distribution of inclination angles derived an average effective half opening angle of 13°. This opening angle is in agreement with a thin disk model in vertical hydrostatic equilibrium which is thinnest at the innermost radius and becomes thicker with increasing radius. Hanuschik (1996) also argues that this model explains the Be-shell transitions (i.e., when a star is observed to switch from a classical Be type spectrum to a Be-shell type) as being caused by an increase of outer disk radius for stars viewed at an inclination angle close to $\sim 70°$.

1.1.5 Rapid Rotation

Rapid rotation is another characteristic of Be stars. The fact that most, if not all, Be stars are rapid rotators suggests that rotation is directly connected to the process, or processes, responsible for the formation of the circumstellar envelope. At the same time, because the observed mean $v \sin i$ values for Be stars show very little variation with spectral type, or between the luminosity classes III, IV and V (Slettebak, 1982), it is possible that the stellar rotation plays only a very indirect role in the disk formation.

Originally, Struve (1931) proposed that all Be stars rotate very close to, or even at the *critical velocity*[4], so that the material near the stellar equator is ejected and forms a circumstellar ring-like structure. This simple idea has been slowly abandoned with time as there was more

---

[3] When the z-component of gravity is balanced by the vertical component of the gas pressure.

[4] Critical velocity is defined as the equatorial spin velocity at which the magnitude of the centrifugal force equals the surface gravity (i.e., $v_{\rm crit} = \sqrt{GM_\star/R_\star}$ where $R_\star$ is the equatorial radius).

spectroscopic evidence that Be stars rotate at rates significantly below the critical limit (Porter, 1996). Currently, the importance of rotation in the formation of the disk-like circumstellar envelope is being reassessed, partly due to the very recent detection of highly oblate Be star by long-baseline interferometry (see § 1.2), as well as, due to the possibility that the published $v \sin i$ values for the fastest rotating stars might be actually underestimated (Townsend, Owocki, & Howarth, 2004).

Another reason rapid rotation of Be stars is an issue is that basic stellar parameters of the central Be star, such as the effective temperature ($T_{\rm eff}$), the luminosity ($L_\star$), and perhaps even the radius ($R_\star$), which are typically assumed to be the same as those of a normal B-type star of the same spectral type, can be affected by the rapid rotation (see also the discussion by Slettebak, 1987).

1.1.6 Variability

The variability associated with the circumstellar environments of Be stars is a major area of active study. One of the more interesting aspects of the variability is that some Be stars, over a time scale of few years, can change into normal B-type stars (Bjorkman, Miroshnichenko, McDavid, & Pogrosheva, 2002). Similarly, B-type stars without previously known line emission can become Be stars (see Miroshnichenko et al., 2003, and references therein). The observations of Miroshnichenko et al. (2003) and Rivinius et al. (1998a) suggest that a Be star can re-build its circumstellar disk on relatively short time scales (of few years), both continuously, as well as in a series of matter ejection episodes. Although the above described variation will result in the most extreme variation of the EW of the Hα emission line, less extreme cases (where EW changes by a few to tens of percent) are also commonly observed (see, for example, Horaguchi et al., 1994).

Variations in the Hα EW are usually associated with broadband photometric variations (Božić et al., 2004; Saad et al., 2004). The photometric variations at the long time scales (years to tens of years) have typically the largest magnitude, but the variations at the shorter time scales (hours to days) appear to be more common (Percy et al., 1997; Percy, Harlow, & Wu, 2004). These short-term photometric variations are thought to be caused by non-radial pulsations (NRPs), which are detected through detailed line-profile analysis (Rivinius, Baade, & Štefl, 2003), and are thought to play a crucial role in the formation of the circumstellar disk (see also § 1.3.2). There is also a possibility that at least in some stars, both the photometric and the spectroscopic variability at the short time scales is due to the rotational modulation of stellar spots or corotating clouds, which would presumably require the presence of the magnetic fields (Balona, 1995).

Changes in the shape of the line emission in Be stars can also be observed, which might not necessarily affect the EW measure, and these are more commonly associated with asymmetric profiles (for example like the ones illustrated in the bottom part of Fig. 1.1). Asymmetric double-peaked profiles are usually characterized with a V/R ratio that measures the ratio of the strengths of violet and red peaks. Single-peaked Hα profiles can also be asymmetric, for example when the inflection due to the non-coherent scattering appears predominantly on one side. For such systems, optically thin Fe II lines show a stronger peak on the same side (Hanuschik, 1987), but this is not generally true for stars with the double-peaked profiles. In fact, the V/R characteristics of double-peaked Fe II and Hα emission lines observed for a given star can be completely different (Slettebak, 1982). This is most likely a direct result of the fact that Fe II emission is sensitive to the physical conditions in a different (smaller) region of the more extended Hα-emitting circumstellar disk.

The V/R variability in the Hα profiles has been a subject of many spectroscopic studies that resulted in a number of different, and at times competing, interpretations. For example, the variability has been explained with elliptical rings where the apsidal motion changes the orientation of the rings which in turn results in density variations in the disk (Huang, 1973; Kříž, 1979). Currently, the most promising explanation for the asymmetry, as well as the variability, is that the symmetric and asymmetric classes of profiles relate to the unperturbed and perturbed states of the same underlying structure, a quasi-Keplerian disk (Hanuschik, Hummel, Dietle, & Sutorius, 1995). This is in agreement with models that predict a formation of global density waves in quasi-Keplerian circumstellar disks, such as the ones constructed by Kato (1983) and Okazaki (1991, 1997).

1.2 Interferometric Studies

The analysis of emission line shapes, like the ones discussed in § 1.1.1, can be quite valuable because the line shapes contain information about the geometry, density, and kinematic structure of the circumstellar material. At the same time, because all of this information is convolved into a single emission profile, it is a challenging, and in some cases might be even an impossible task to separate all of this information unambiguously. What is needed then is a separate observational technique that can directly provide information about the spatial structure of the envelope. Because the angular diameters of these envelopes are smaller than the diffraction limits of the largest optical telescopes in existence today, long-baseline optical interferometers are the only instruments that can spatially resolve the circumstellar regions of Be stars at the visible wavelengths.

Although the radii of the Hα-emitting disks around Be stars can be estimated using the observed separation of the peaks (in the case of double-peaked profiles), this approach requires one to make assumptions about the stellar mass and the velocity law in the disk (Huang, 1972). The presence of non-coherent scattering can also influence the measurements and in that case, a correction factor might be necessary to obtain an estimate on the radius (see Hummel, 1994, and references therein). The situation is much different for optical interferometric observations, where even if the baselines are not long enough to resolve the inner part of the Hα-emitting disk, but are long enough to resolve the outer extent, they can still provide an accurate measurement of the disk radius. Furthermore, if the interferometric observations are obtained on two, or more, appropriately oriented baselines (so that the source structure is resolved at different positional angles), not only the size of the region can be determined, but also the deviation from circular symmetry.

The initial attempts to apply optical interferometry to Be stars have been quite promising. One of the first interferometric observations that resolved the circumstellar envelope of a Be star was that of γ Cas with the I2T interferometer (Thom, Granes, & Vakili, 1986). Shortly thereafter, the Mark III interferometer was used to obtain the first direct measurements of the asymmetry of the Hα emitting region for γ Cas and ζ Tau (Quirrenbach et al., 1993, 1994). Interferometric observations that divide the Hα emission line into a number of spectral channels have also been obtained with the GI2T interferometer, and they resulted in the first detection of a rotational signature in an envelope of a Be star (Mourard et al., 1989; Stee et al., 1995). The combination of the linear polarization studies with the interferometric observations of a number of Be stars, that have shown that the Hα-emitting envelopes are flattened, is the strongest observational evidence to date for the presence of relatively-thin circumstellar disks (Quirrenbach et al., 1997).

The only interferometric studies to date that were truly aimed at the detection of the temporal variability in the circumstellar envelopes of Be stars were done by Vakili et al. (1998)

on ζ Tau, and Berio et al. (1999) on γ Cas. These studies suggest that an apparent one-armed over-density region in a circumstellar disk is responsible for the commonly observed changes in the V/R ratio. These results are generally consistent with the current theoretical picture that explains these variations as one-armed oscillations in nearly Keplerian circumstellar disks. At the same time, the possibility still exists that the density wave is more like a spiral structure rather than a simple one-armed over-density region, at least in some stars (Porter & Rivinius, 2003).

The study of the stellar rotation and its connection to the mechanisms involved in the formation of the disks around Be stars is another area where long-baseline interferometry will most likely play a crucial role. In fact, the recent interferometric detection of a high degree of oblateness in the Be star α Eridani by Domiciano de Souza et al. (2003), compounded with the possibility that most $v \sin i$ values for Be stars could be significantly underestimated (Townsend, Owocki, & Howarth, 2004), has started to shift the focus back onto stellar rotation and its connection to the Be phenomenon. The investigation of the relationship between the physical extent of the circumstellar region and the stellar rotation could prove very valuable in establishing its role in the disk formation.

1.3 Disk Formation Theories

The mechanisms responsible for the formation of the circumstellar disks of Be stars are not fully understood, although a number of theories have been proposed (see Bjorkman, 2000, for a review). The theoretical models can be divided between those that describe the accretion of the circumstellar material, or decretion of the material from the surface of the star.

1.3.1 Accretion Disks

The accretion models are usually explained with mass infall from circumstellar disk, either due to a remnant protostellar disk, or due to a mass-transfer from a binary component. Because the remnant protostellar disk is unlikely to survive for any significant fraction of the main-sequence life-time of a Be star, it is typically assumed that such models could only be applied to the youngest Be stars. At the same time, there is some observational evidence that Be stars first appear in clusters some 10^7 yr after birth (Fabregat & Torrejón, 2000).

The accretion due to the mass-transfer from a secondary might be applicable to a much wider range of Be stars, as long as a large fraction of Be stars exist in close binary systems. The binary mass-transfer requires one of the components to evolve off the main-sequence, fill its Roche lobe, and consequently transfer some mass to the Be companion through an accretion disk. In the process, the mass-receiving star gains angular momentum and therefore this naturally explains the rapid rotation rates observed for Be stars. However, in almost all classical Be stars there is no evidence for a cool giant that overflows its Roche lobe, so if binary evolution is responsible for formation of Be stars it is more likely that the Be stars are post-mass-transfer binary systems where the secondary is a Helium star, white dwarf, or a neutron star (see Pols, Cote, Waters, & Heise, 1991, and references therein). In this case the spin-up process (due to the mass transfer) alone is responsible for the formation of Be stars by increasing their rotation rates close to the critical values, which consequently initiates some type of outflow from the Be star (see also the discussion in Gies, 2000). It is unclear at the moment what fraction of Be stars could actually be created in binaries, but it is commonly accepted that this process will not be applicable to all Be stars (Bjorkman, 2000).

1.3.2 Decretion Disks

The decretion models describe the mass loss in the form of continuous outflow, as in a stellar wind, or in the form of discrete ejection episodes. One of the more successful models predicting a circumstellar disk for rapidly rotating stars is the Wind Compressed Disk (WCD) model (Bjorkman & Cassinelli, 1993). The WCD is formed by supersonic wind that originates at high stellar latitudes, but travels along orbital trajectories that carry it down to equatorial plane, where it collides with the wind originating from the opposite hemisphere. The result is a compressed (by the ram pressure) higher density disk with significant density enhancement and an opening angle of few degrees (Bjorkman & Cassinelli, 1993; Owocki, Cranmer, & Blondin, 1994).

The recently reported discrete mass-loss events in the early-type Be stars, triggered by the beating of nonradial pulsation modes, might also be responsible for the formation of the Be disks (Rivinius et al., 1998a,b). It is not yet known if such a mechanism plays a general role in all Be stars, especially since spectroscopic evidence for NRP has not been demonstrated for all stars. Other mechanisms for ejecting matter from the stellar surface into the circumstellar disk have also been proposed. These range from gravitational tidal torques due to binary companions, to explosive events such as stellar flares (see Bjorkman, 2000, and references therein). Of course, without observational constraints, most of these ideas remain only speculative.

1.4 Unresolved Issues

One of the major unresolved issues related to our understanding of the Be-phenomenon is the process of mass ejection (either as a continuous mass loss or in the form of discrete events) from the stellar surface, and the subsequent formation of the disk. Optical interferometric observations might prove to be critical in our understanding of this phenomenon since they have the potential of directly imaging the mass ejection episodes. For example, spectroscopic observations suggest that the circumstellar envelopes could be evolving from disk-like to ring-like structures on time scales of months (Rivinius et al., 2001). Spatially resolving such changes in the circumstellar disk with an optical interferometer would provide indispensable observational evidence for the evolution of the material in the circumstellar disk.

Another area that requires further investigation is the connection between the rapid rotation of Be stars and the formation of circumstellar disk. In fact, this fundamental area of astrophysics that describes rotationally enhanced mass loss is waiting to be explored by optical interferometers. Also, the importance of magnetic field on the formation and stability of the Be star disks, is not fully understood. If magnetic fields in Be stars are common, they must be relatively weak, since they have eluded most observational campaigns, and to date only one unconfirmed report of weak magnetic field detection exists (Neiner et al., 2003).

There are also a number of issues that, even if resolved by themselves, might not be able to explain the origin of the circumstellar disks around Be stars, but in conjunction with other observations might end up playing a critical role in our understanding of these objects. Some of these issues are: investigating the importance of binarity on Be phenomenon (including the possible connection to disk distortions), constraining the degree of flattening of the disks (including the possibility of detection of warping), and probing the velocity structure in the circumstellar disk. Also, many models of line formation in Be star envelopes assume that the disk starts with some initial non-zero density immediately at the stellar surface. The hydrodynamical simulations of wind-compressed disks by Owocki, Cranmer, & Blondin (1994) suggest that there is no detachment of the disk from the star, in fact they predict an inflow of mass at the inner disk. Other models, such as those of Bjorkman & Cassinelli (1993) predict a detachment of the disk from the stellar surface. A direct detection of an inner radius of the line-emitting disk would definitely play an important role in constraining the current models.

The study of Be star disks not only contributes to our understanding of these interesting and not fully understood objects, but it can also make significant contributions to other branches of stellar astrophysics. For example, the investigation of disk formation mechanism(s) will contribute to our understanding of asymmetric mass-loss processes including stellar angular momentum distribution (especially in the context of rapidly rotating stars). The apparent outflow of the material in the circumstellar disk and its possible eventual dispersal, is an excellent test ground for examining theories related to angular momentum transfer in outflowing disks. The processes involved in such angular momentum transfer (most likely requiring significant viscosity in the disk) might be very similar to those occurring in the accretion disks around young stars, even though the physical conditions might be different in the two environments.

Observational studies aimed at investigating the central stars can also be valuable to other branches as astronomy. For example, non-radial pulsations are detected in many Be stars, and therefore these type of observations contribute to the much wider field of astroseismology, which applies to a wide variety of stars including neutron and solar-type stars. Because stellar magnetic fields might be necessary to explain most of the variability associated with the circumstellar disks of Be stars, studies related to the connection between stellar magnetic activity and the circumstellar material will contribute to our understanding of magnetic field evolution. Also, the decretion disks around Be stars can be used to probe unseen binary companions, such as neutron stars and black holes, through direct detection of X-ray emission as well as through detection of disk truncation due to tidal interaction (see, for example, Zhang, Li, & Wang, 2004).

1.5 Outline

It is quite clear that long-baseline optical interferometry will play a critical role in providing the observations needed to constrain the models describing the Be phenomenon. Although to date optical interferometric observations have already contributed to the study of Be stars, further observations are necessary. The new observations need to cover not only a number of different objects at different epochs (to investigate the variability), but they also need to be of high enough quality so that specific model constraints can be obtained. In fact, the accuracy of most interferometric observations of Be stars published in the literature is limited by the calibration of the interferometric observables.

This dissertation describes how high precision optical interferometry can be applied to classical Be stars. First, we introduce the basic concepts of Michelson stellar interferometry in the context of the Navy Prototype Optical Interferometer (Ch. 2). We then present a new technique for internally calibrating multi-spectral optical interferometric observations of Be stars. The new technique can calibrate interferometric data without the need of an external calibrator, and in Chapter 3 we demonstrate its usefulness on observations of a well known Be star γ Cassiopeiae. In subsequent chapters (Chs. 4 through 6) we present our analysis and modeling of the Hα-emitting circumstellar envelopes of another three Be stars, ζ Tauri, η Tauri, and β Canis Minoris. In Chapter 7 we investigate the properties of the Hα-emitting regions, and in Chapter 8 we conclude with a summary and a discussion of future directions.

Chapter 2

Optical Interferometry

We begin with a brief introduction to the basic concepts of stellar interferometry. Our discussion will concentrate on the source characteristics and the interferometric observables that are most relevant to the work presented in the subsequent chapters. A more complete discussion of the theory of interferometry (in the context of both radio and optical interferometers) can be found in Thompson, Moran, & Swenson (2001), as well as in the excellent review papers[1] of optical interferometry by Shao & Colavita (1992), Quirrenbach (2001), and Monnier (2003a).

2.1 Basic Theory of Interferometry

2.1.1 Monochromatic Case

To illustrate the basic interference phenomenon we will consider a simple two-element interferometer that receives radiation from a distant astronomical source. We assume that the emitting source is at a large enough distance that the wave-fronts arriving at the interferometer can be described by plane waves. Figure 2.1 illustrates a simple model of an interferometer with the centers of the apertures separated by a vector $\boldsymbol{B}$, also known as the *baseline* vector. The two apertures are pointed at the same celestial point in the direction of the unit vector $\hat{\mathbf{s}}_0$ and thus they sample the same incident wave-front (this is also known as the division of the wave-front). More specifically, if we assume that the two apertures are at positions $\boldsymbol{s}_1$ and $\boldsymbol{s}_2$ with respect to the source, then the electric field[2] vector of a plane monochromatic electromagnetic field of

---

[1] See also the *Principles of Long Baseline Stellar Interferometry*, Course Notes from the 1999 Michelson Summer School held at the CALTECH in Pasadena, California, Editor Peter R. Lawson.

[2] We are using the convention that the physical electric field is obtained by taking the real part of a complex quantity (see also Jackson, 1999, p. 296).

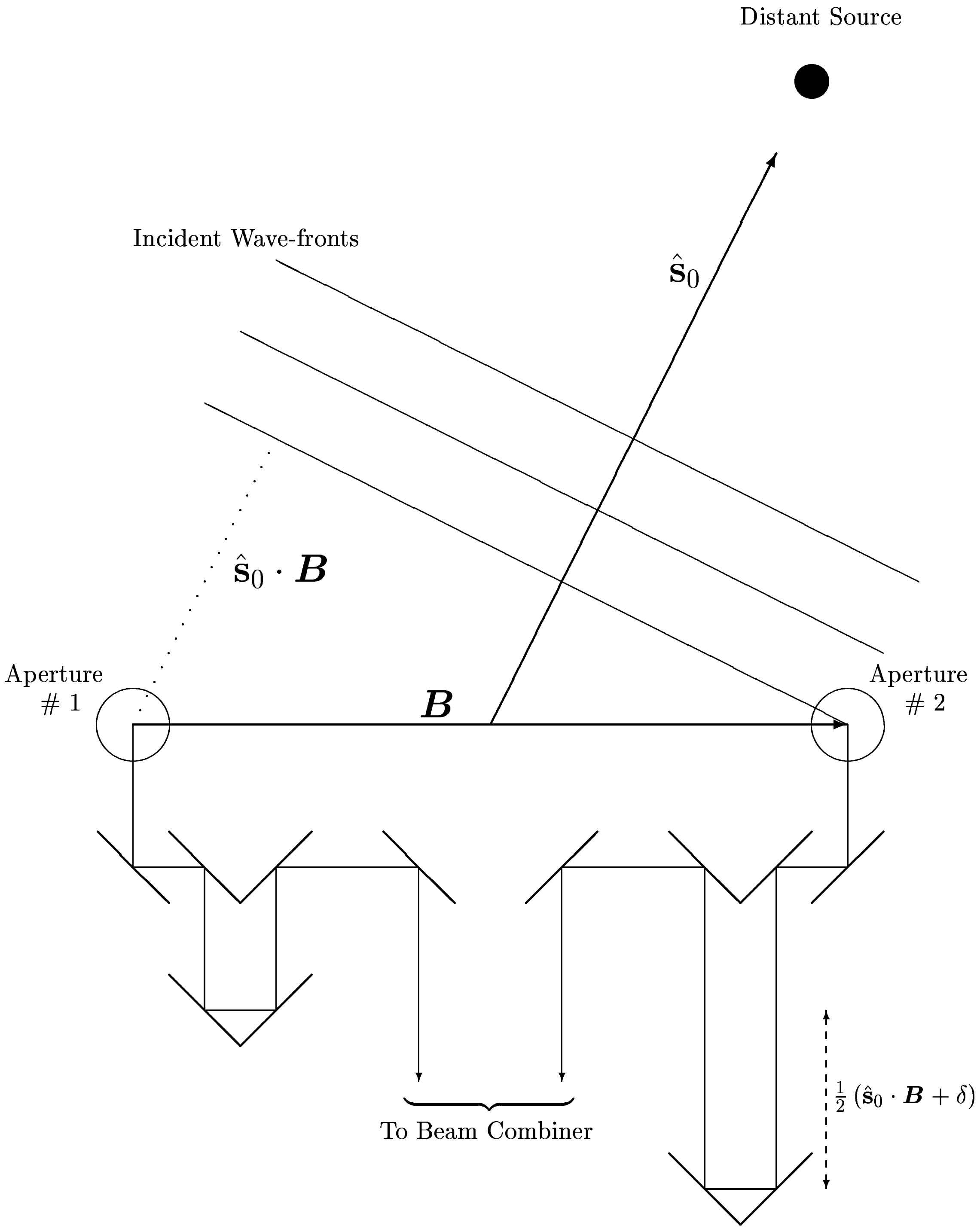

FIGURE 2.1: A simple representation of a two-element interferometer. The beams from the two apertures are send to the beam combiner where they can be superposed in an image- or a pupil-plane (see, for example, Fig. 13 in Monnier, 2003a).

frequency ν at the two apertures can be expressed as

$$\boldsymbol{E}_1(t) = \boldsymbol{A}_1 \mathrm{e}^{\mathrm{i}(\boldsymbol{k}\cdot\boldsymbol{s}_1 - 2\pi\nu t)} \qquad \text{and} \qquad \boldsymbol{E}_2(t) = \boldsymbol{A}_2 \mathrm{e}^{\mathrm{i}(\boldsymbol{k}\cdot\boldsymbol{s}_2 - 2\pi\nu t)}, \tag{2.1}$$

where $\boldsymbol{k}$ is the wavenumber $(2\pi/\lambda)$ in the direction of the propagation (which in our case is the same as direction of vectors $\boldsymbol{s}_1$ and $\boldsymbol{s}_2$), and $\boldsymbol{A}_1$ and $\boldsymbol{A}_2$ are the amplitude vectors in the direction perpendicular to the propagation vector (i.e., the electric field is transverse). The individual amplitudes A_1 and A_2, although intrinsically the same, may actually differ because of the different transmission properties of the atmosphere above the two apertures.

Generally, the distance from the source to each aperture will not be the same, but we can express the distance $|\boldsymbol{s}_1|$ as a sum of the distance $|\boldsymbol{s}_2|$ and an extra distance (also known as the geometric delay) given by $\hat{\mathrm{s}}_0 \cdot \boldsymbol{B}$ (see the dotted line in Fig. 2.1). After the wave-fronts reach the two apertures they are further propagated through a series of optics to a place where they are combined (for example, using a beam splitter), and thus the distance in the optical path of each beam increases by an additional length d_1 and d_2, respectively. Therefore, the electric fields at the position of the beam combiner can be written as

$$\boldsymbol{E}_1(t) = \boldsymbol{A}_1 \mathrm{e}^{-2\pi\mathrm{i}\nu t} \mathrm{e}^{\mathrm{i}k(s_1 + d_1)} = \boldsymbol{A}_1 \mathrm{e}^{-2\pi\mathrm{i}\nu t} \mathrm{e}^{\mathrm{i}k(s_2 + \hat{\mathrm{s}}_0\cdot\boldsymbol{B} + d_1)}, \tag{2.2}$$

and

$$\boldsymbol{E}_2(t) = \boldsymbol{A}_2 \mathrm{e}^{-2\pi\mathrm{i}\nu t} \mathrm{e}^{\mathrm{i}k(s_2 + d_2)}, \tag{2.3}$$

where the amplitudes, A_1 and A_2, now include the losses due to the transmission and the reflection properties of all the optical components in the system. The net electric field, $\boldsymbol{E}$, of the combined beams can be expressed as a vector superposition and therefore has the form

$$\boldsymbol{E} \equiv \boldsymbol{E}_1 + \boldsymbol{E}_2 = \mathrm{e}^{-2\pi\mathrm{i}\nu t} \mathrm{e}^{\mathrm{i}ks_2} \mathrm{e}^{\mathrm{i}kd_2} \left[\boldsymbol{A}_1 \mathrm{e}^{\mathrm{i}(k\delta \pm \pi/2)} + \boldsymbol{A}_2 \right], \tag{2.4}$$

where $\delta = \hat{\mathrm{s}}_0 \cdot \boldsymbol{B} + d_1 - d_2$, which represents the optical path difference (OPD) between the two beams. We have also added a $\pm\pi/2$ phase term in the above equation to account for the phase difference between the reflected and transmitted beams at the beam splitter (see, for example, Traub, 1999).

The intensity I of the light beam (averaged over time) can be expressed as (Born & Wolf, 1999, p. 287):

$$I \propto \langle \boldsymbol{E}^2 \rangle = \frac{1}{2} \boldsymbol{E} \cdot \boldsymbol{E}^*. \tag{2.5}$$

Neglecting a few constants in the above equation (which are not relevant in this discussion), allows us to write the intensity of the combined beams as

$$\begin{aligned} I(\delta) &= \frac{1}{2}A_1^2 + \frac{1}{2}A_2^2 + \frac{1}{2}\boldsymbol{A}_1 \cdot \boldsymbol{A}_2 \left[\mathrm{e}^{\mathrm{i}(k\delta \pm \pi/2)} + \mathrm{e}^{-\mathrm{i}(k\delta \pm \pi/2)}\right] \\ &= 2I_0 \left[1 + \cos(k\delta \pm \pi/2)\right] \\ &= 2I_0 \left[1 \pm \sin(k\delta)\right], \end{aligned} \tag{2.6}$$

where in the last step we have assumed that the intensity of each beam is the same and equals I_0, as well as that the beams have the same linear polarization (i.e., $\boldsymbol{A}_1 \cdot \boldsymbol{A}_2 = A_1 A_2$).

The sign in front of the sine function in equation (2.6) is not arbitrary, because the energy must be conserved between the two outputs from the beam combiner, and therefore one of the outputs will have a positive sign, and the other negative. Each output receives on average half of the photons, and therefore in an actual experiment the intensity variations from both outputs of the beam splitter need to be recorded. For simplicity of our discussion we will concentrate only on one of the outputs from the beam splitter (the one with a positive sine function). Figure 2.2 shows the intensity pattern that would be observed as a function of δ at one of the outputs from the beam splitter. The smooth sinusoidal brightness variation as a function of OPD, caused by the constructive and destructive interference between the beams, is typically known as the *fringe* pattern.

2.1.2 Polychromatic Case

The discussion of the monochromatic wave-front in previous section resulted in a rather unrealistic fringe pattern that extends from $-\infty$ to $+\infty$ (which is directly related to the fact that purely monochromatic waves by definition must be coherent over infinite scales). Nevertheless, the result from equation (2.6) can be used to describe a more realistic case where the spectral bandpass has a finite width. Because stellar sources emit photons which are mutually incoherent, then the intensity of the interference pattern at one wavelength will be independent of another. Therefore, an interference pattern of a light beam with a finite spectral bandpass can be represented by a simple sum of fringe patterns, each corresponding to a different monochromatic beam.

We now consider a case where the source emits electromagnetic radiation that can be described as a flux per unit frequency, F_ν, over a spectral bandpass, $\Delta\nu$, centered at ν_0. Without much loss of generality we assume that the flux is constant over the range of the bandpass and

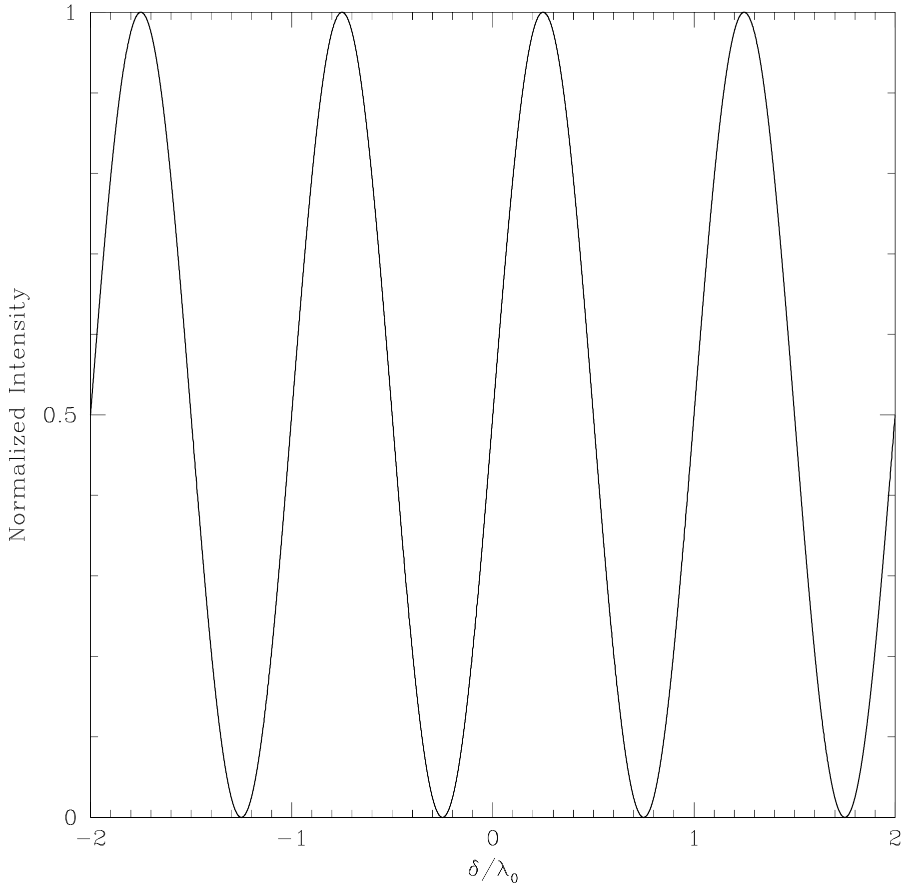

FIGURE 2.2: Model fringe pattern for a monochromatic light (of wavelength λ_0) from a point-source. The horizontal axis represents the optical path difference between the two beams (in units of λ_0).

thus $I_0 = F_\nu \Delta\nu$. Using equation (2.6) we can express the interference pattern for an unresolved source of finite spectral bandpass as:

$$\begin{aligned} I(\delta) &= \int_{\nu_0-\Delta\nu/2}^{\nu_0+\Delta\nu/2} F_\nu \left[1 + \sin(2\pi\delta\nu/c)\right] \mathrm{d}\nu \\ &= F_\nu \left[\Delta\nu + \frac{\cos\left(2\pi\delta[\nu_0 - \Delta\nu/2]/c\right) - \cos\left(2\pi\delta[\nu_0 + \Delta\nu/2]/c\right)}{2\pi\delta/c}\right]. \end{aligned} \tag{2.7}$$

With the help of a trigonometric relation[3] we can rewrite the above equation to have the form,

$$\begin{aligned} I(\delta) &= F_\nu \Delta\nu \left[1 + \frac{\sin(\pi\delta\Delta\nu/c)}{\pi\delta\Delta\nu/c} \sin(2\pi\delta\nu_0/c)\right] \\ &= I_0 \left[1 + \mathrm{sinc}(\pi\delta\Delta\nu/c) \sin(k_0\delta)\right], \end{aligned} \tag{2.8}$$

or with an introduction of a constant $L_{\mathrm{coh}} = \lambda_0^2/\Delta\lambda$, known as the *coherence length*, and using the fact that $|\Delta\nu| = |c\Delta\lambda/\lambda^2|$, it becomes

$$I(\delta) = I_0 \left[1 + \mathrm{sinc}(\pi\delta/L_{\mathrm{coh}}) \sin(k_0\delta)\right]. \tag{2.9}$$

By comparing equations (2.6) and (2.9), we can conclude that the fringe pattern in the case of a polychromatic wave-front is the same as in the monochromatic case, except for the extra modulation envelope (given by a sinc function for a top-hat flux distribution) that multiplies the sinusoidally varying fringes (see also Figure 2.3). The expression for the intensity of the interference pattern observed in a more general case can be written as

$$I(\delta) = I_0 \left[1 \pm M(L_{\mathrm{coh}}, \delta) \sin(k_0\delta)\right], \tag{2.10}$$

where M is the modulation function, which is related (through a Fourier transform) to the shape of the spectral region. Therefore, recording the interference pattern, as a function of OPD, and taking the inverse Fourier transform allows the reconstruction of the spectrum. This is in fact a basic principle of a Fourier transform spectrometer.

2.1.3 The van Cittert-Zernike Theorem

An optical interferometer measures the net degree of coherence between two or more light beams from different array elements. The degree of coherence is reduced by two main physical effects. The first effect, already discussed in previous section, is due to the width and shape of the spectral region, and results in a decreasing fringe contrast with increasing OPD. On the other

---

[3] Trigonometric relation given by $\cos(A - B) - \cos(A + B) = 2 \sin A \sin B$.

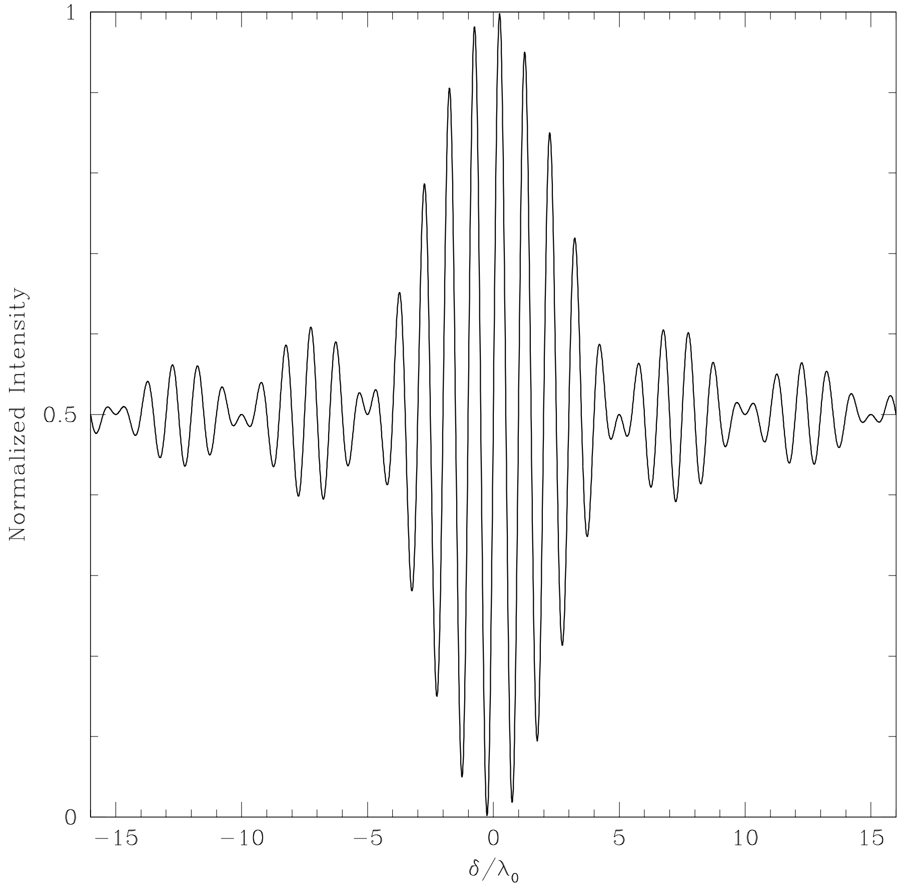

FIGURE 2.3: Same as Fig. 2.2, but for a polychromatic light with a central wavelength at λ_0 and a 20% bandwidth ($\Delta\lambda = \lambda_0/5$).

hand, at the zero optical path difference (ZOPD) the interference patterns for all wavelengths are in phase and no apparent loss of coherence is observed.

The second effect responsible for reducing the degree of coherence between two beams is due to the extended (resolved) structure of the emitting source. This is a direct consequence of the fact that to achieve a ZOPD for two point-sources located in slightly different directions requires different path compensations (to correct for the extra geometrical distance above the elements). This results in a general loss of coherence at all values of OPD (including the ZOPD). Because an extended source can be treated as a sum of incoherent point-sources, the resulting interference pattern due to an extended source can be treated as a sum of individual interference patterns for point sources, each in slightly different direction. This is very similar to the treatment of the polychromatic source that we have discussed in the previous section, where the interference pattern for a polychromatic source was expressed in terms of a sum of interference patterns for monochromatic beams.

We have discussed in § 2.1.2 how the modulation function, which represents the loss of coherence due to the polychromatic light, is related to the shape of the spectral bandpass through a Fourier transform. Similarly, in the case of a resolved source structure, the loss of coherence is also related to the Fourier transform of the intensity distribution of the source on the sky. We can introduce a quantity known as the complex visibility ($\mathcal{V} = V\mathrm{e}^{-\mathrm{i}\Phi}$), which is directly related to the degree of coherence between two beams, and its visibility amplitude (V) is given by

$$V = \frac{I_{\mathrm{max}} - I_{\mathrm{min}}}{I_{\mathrm{max}} + I_{\mathrm{min}}}, \tag{2.11}$$

where I_{max} and I_{min} are the maximum and minimum intensities observed in the fringe pattern for a combined beam. The visibility phase (Φ) corresponds to the displacement of the center of the fringe packet from some reference point along the OPD. This reference point is usually the position of the ZOPD that corresponds to the center of the field being observed (defined to be in the direction of the unit vector $\hat{\mathbf{s}}_0$). It can be shown that $\mathcal{V}$ is related to the structure of the emitting source on the sky $I(\lambda, \boldsymbol{s})$ through an integral of the form

$$\mathcal{V}(\lambda, \boldsymbol{B}) = \int_{\mathrm{source}} I(\lambda, \hat{\mathbf{s}}_0 + \delta\boldsymbol{s}) \exp[-\mathrm{i}2\pi\lambda^{-1}\boldsymbol{B}\cdot\delta\boldsymbol{s}]\mathrm{d}\Omega, \tag{2.12}$$

where $\boldsymbol{B}$ is the baseline vector between the elements, λ is the wavelength, and $\delta\boldsymbol{s} \equiv (\theta_x, \theta_y)$ specifies the position on the sky with respect to the center of the field. The relation in equation (2.12) is also known as the van Cittert-Zernike Theorem and the limitation as well as the assumptions behind its formulation are discussed in detail by Thompson, Moran, & Swenson (2001).

Without much loss of generality we can assume that the intensity of the source on the sky does not change with wavelength (or equivalently we can assume that λ is fixed) in which case the intensity of the source will be a function of only the sky coordinates θ_x and θ_y. This allows us to express the dot product in equation (2.12) as

$$\boldsymbol{B} \cdot \delta \boldsymbol{s} = \lambda \left(u\theta_x + v\theta_y + w\theta_z \right), \tag{2.13}$$

where we introduced the notation of spatial frequencies u, v, w (i.e., $u = B_x/\lambda$, $v = B_y/\lambda$, and $w = B_z/\lambda$). Finally the equation (2.12) can be simplified to have a more familiar form of a two-dimensional Fourier transform:

$$\mathcal{V}(u,v) \equiv V(u,v)\mathrm{e}^{-\mathrm{i}\Phi(u,v)} = \int_{-\infty}^{\infty}\int_{-\infty}^{\infty} I(\theta_x,\theta_y)\mathrm{e}^{-\mathrm{i}2\pi(\theta_x u + \theta_y v)}\mathrm{d}\theta_x\,\mathrm{d}\theta_y, \tag{2.14}$$

where we have extended the integration from $-\infty$ to $+\infty$ since the intensity will fall off to zero outside the source (as well as outside the field-of-view), and ignored[4] the dependence on w. Because the complex visibility is typically defined as a normalized dimensionless quantity, we define $I(\theta_x,\theta_y)$ as a normalized source intensity distribution, where

$$\int_{-\infty}^{\infty}\int_{-\infty}^{\infty} I(\theta_x,\theta_y)\mathrm{d}\theta_x\,\mathrm{d}\theta_y = 1. \tag{2.15}$$

2.1.4 Uniform Disk Source

To illustrate the usefulness of the van Cittert-Zernike theorem we illustrate its application on a simple, but very fundamental source structure — the uniform disk. Because a uniform disk is circularly symmetric, the two-dimensional Fourier transform in equation (2.12) can be rewritten so that the two independent variables, θ_x and θ_y, can be replaced with only one variable, r, in the radial direction (where $r^2 = \theta_x^2 + \theta_y^2$). It can be shown[5] that this leads to a Hankel transform:

$$\mathcal{V}(s) = 2\pi \int_0^{\infty} I(r)J_0(2\pi s r)r\mathrm{d}r, \tag{2.16}$$

where $s^2 = u^2 + v^2$.

---

[4] The dependence on w can be ignored in the limit of small field of view, normally encountered in optical interferometry (see also Thompson, Moran, & Swenson, 2001, p. 73).

[5] For a more detailed derivation and discussion one can refer to Bracewell (2000, p. 336).

We now consider a uniform disk (UD) with an angular diameter $\theta_{\rm UD}$ (in radians) for which the source intensity can be written as

$$I(r) = \begin{cases} I_0 & : \quad r \leq \theta_{\rm UD}/2 \\ 0 & : \quad r > \theta_{\rm UD}/2 \end{cases}, \tag{2.17}$$

and in order for equation (2.15) to be satisfied we require $I_0 = 4/(\pi\theta_{\rm UD}^2)$. Now, using the Hankel transform given in equation (2.16) we can calculate the model visibility for a UD

$$\mathcal{V}_{\rm UD}(s) = 2\pi I_0 \int_0^{\theta_{\rm UD}/2} r J_0(2\pi s r) {\rm d}r, \tag{2.18}$$

which with the substitution of $r' = 2\pi s r$, can be rewritten as

$$\mathcal{V}_{\rm UD}(s) = \frac{2}{(\pi\theta_{\rm UD}s)^2} \int_0^{\pi\theta_{\rm UD}s} r' J_0(r') {\rm d}r'. \tag{2.19}$$

The above integral can be evaluated easily using a well-known recurrence relation[6] to give

$$\mathcal{V}_{\rm UD}(s) = 2\frac{J_1(\pi\theta_{\rm UD}s)}{\pi\theta_{\rm UD}s}, \tag{2.20}$$

where J_1 is the first-order Bessel function. It is interesting to note that the visibility in the above equation is real (although it can have positive and negative values). This could have been predicted based on the fact that a Fourier transform of a symmetric function produces a real function. Figure 2.4 illustrates the shape of the first-order Bessel function by showing the visibility as a function of the projected baseline length for $\theta_{\rm UD}$ of 2 mas, and a fixed wavelength of 600 nm. We can see from the figure that indeed the J_1 function has both positive and negative values. The position of the first zero crossing has some historical, as well as practical significance and occurs when the argument of J_1 equals 1.220π (Born & Wolf, 1999, p. 441), and in our case this translates to a projected baseline length of $1.22\lambda/\theta_{\rm UD}$.

2.2 Optical Interferometry in Practice

2.2.1 The Instrument

The Navy Prototype Optical Interferometer (NPOI) is located at the Anderson Mesa near Flagstaff, Arizona. It is a descendant of the Mark I through Mark III phase-tracking optical interferometers developed by Shao and his colleagues on Mount Wilson (Shao & Staelin, 1980;

---

[6] A recurrence relation of $\frac{\rm d}{{\rm d}r'}\left[r' J_1(r')\right] = r' J_0(r')$ (see Born & Wolf, 1999, p. 440 and references therein).

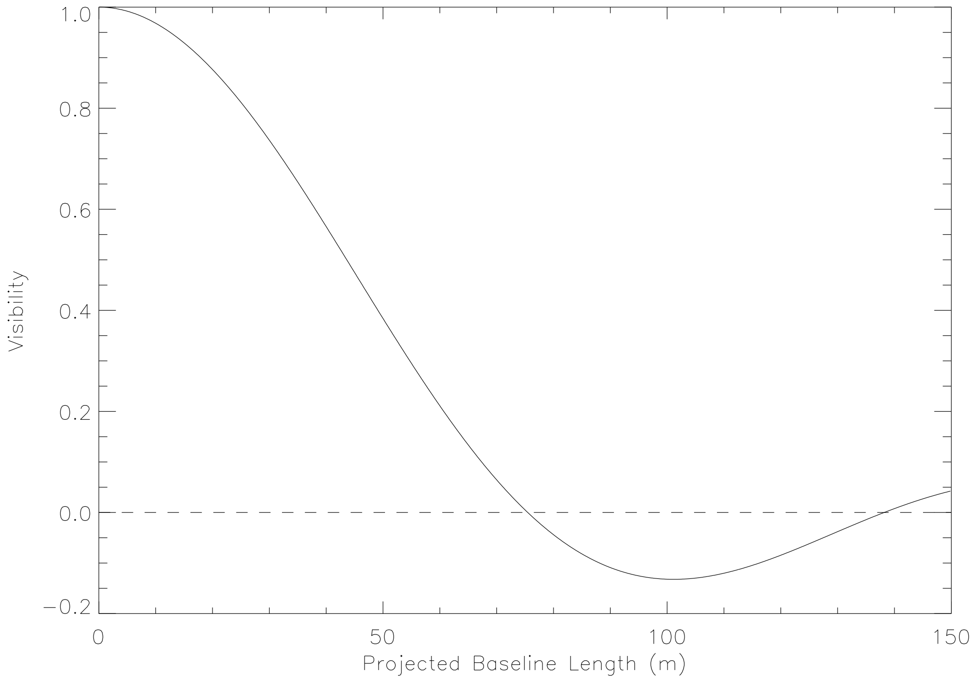

FIGURE 2.4: Model visibility amplitude for a 2 mas diameter uniform disk (*solid-line*). The zero level amplitude is shown with a *dashed-line* and the wavelength is assumed to be fixed at 600 nm.

Shao et al., 1987, 1988). The NPOI consists of many components such as: siderostats[7] that collect the starlight, vacuum pipe-lines that transport the starlight to a beam-combining lab, long and short optical delay lines that compensate for the unequal path-lengths above the elements, and of course the control and maintenance buildings (see the aerial view of the instrument in Fig. 2.5). In this section we will review briefly only those aspects of the instrument which are directly relevant to the discussion presented in the subsequent chapters. For a more detailed discussion of all the critical components, the reader is referred to the excellent description of the NPOI by Armstrong et al. (1998).

The physical layout of the NPOI can be divided between an imaging sub-array, which is the most extended, and an astrometric sub-array, which can be used for both astrometry (its primary purpose) and as a component of the imaging sub-array. The imaging sub-array consists of a total of 30 siderostat locations distributed in a Y-shape configuration, where 6 movable siderostats can be positioned for a desired baseline configuration. The Y-shaped imaging sub-array is shown schematically in Figure 2.6 and the positions of the four astrometric stations,

---

[7] These are flat mirrors with a diameter of 50 cm and a maximum unvignetted aperture of 35 cm. Currently the diameter of the aperture is limited to 12 cm by the feed-system optics.

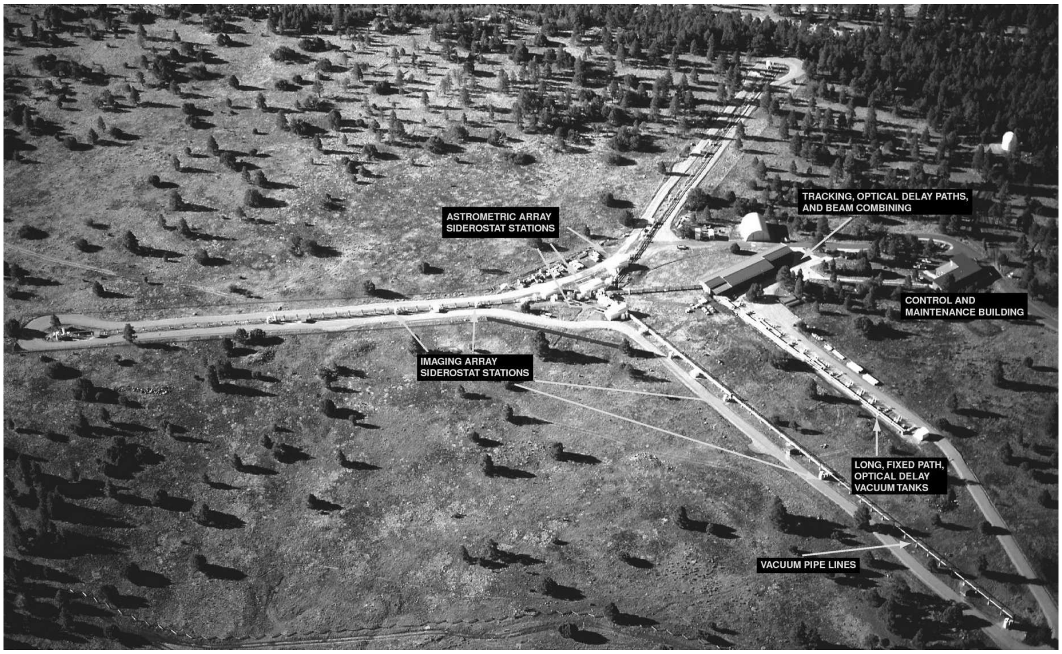

FIGURE 2.5: Aerial view of the Navy Prototype Interferometer. Image Courtesy of the NPOI team.

located in the inner part, are shown in Figure 2.7.

The NPOI was designed to capture beams of light from up to six apertures simultaneously, and to send them to a common place where they can be superposed in a pupil-plane. At the time the interferometric observations presented in this dissertation were acquired, only three beams could be combined simultaneously in a pair-wise beam combination scheme (see Fig. 2.8). In this setup, a separate interference pattern for each of the three baselines was produced as the OPD between the individual beams was varied across the ZOPD using a triangle-wave modulation with an amplitude of a few wavelengths. In order to sample the fringe packet on time scales much shorter than those associated with the delay variations due to the atmospheric turbulence (i.e., so that the fringe packet would appear to be stationary), the frequency of the modulation was set at 500 Hz.

Before the intensity variations as a function of OPD were recorded for each pair of beams, they were dispersed by a prism onto a linear lenslet array. A series of optical fibers glued to the back of each of the three lenslet arrays, for the three pairs of beams, carried the signal to a cluster of photon-counting avalanche photodiodes (APDs), which in turn recorded the intensity variations (photon counts) synchronously with the modulation. Each lenslet array provided 32 spectral channels covering the 450–850 nm spectral region. However, because the number of

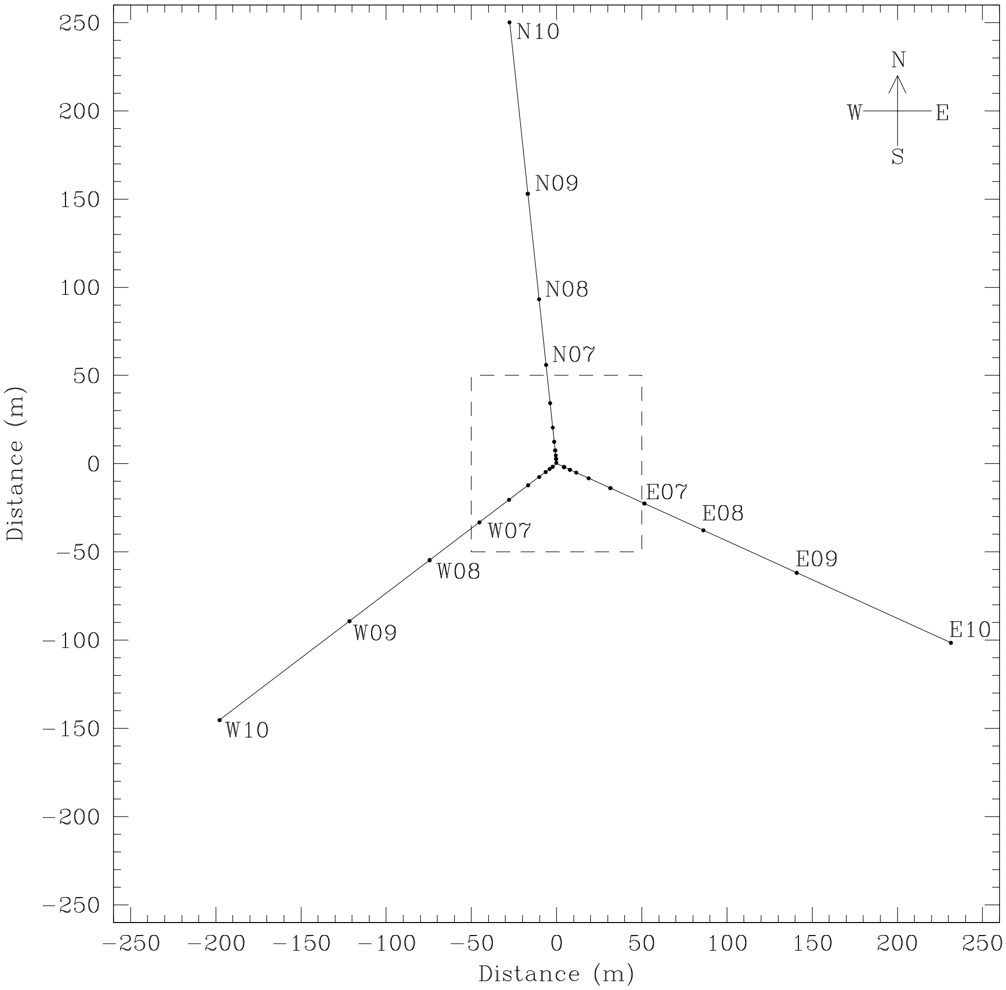

FIGURE 2.6: Layout of the possible positions for the imaging elements (indicated by dots), with the station names indicated only for the outer elements. The inner region of the array (*dashed box*) is shown in Fig. 2.7.

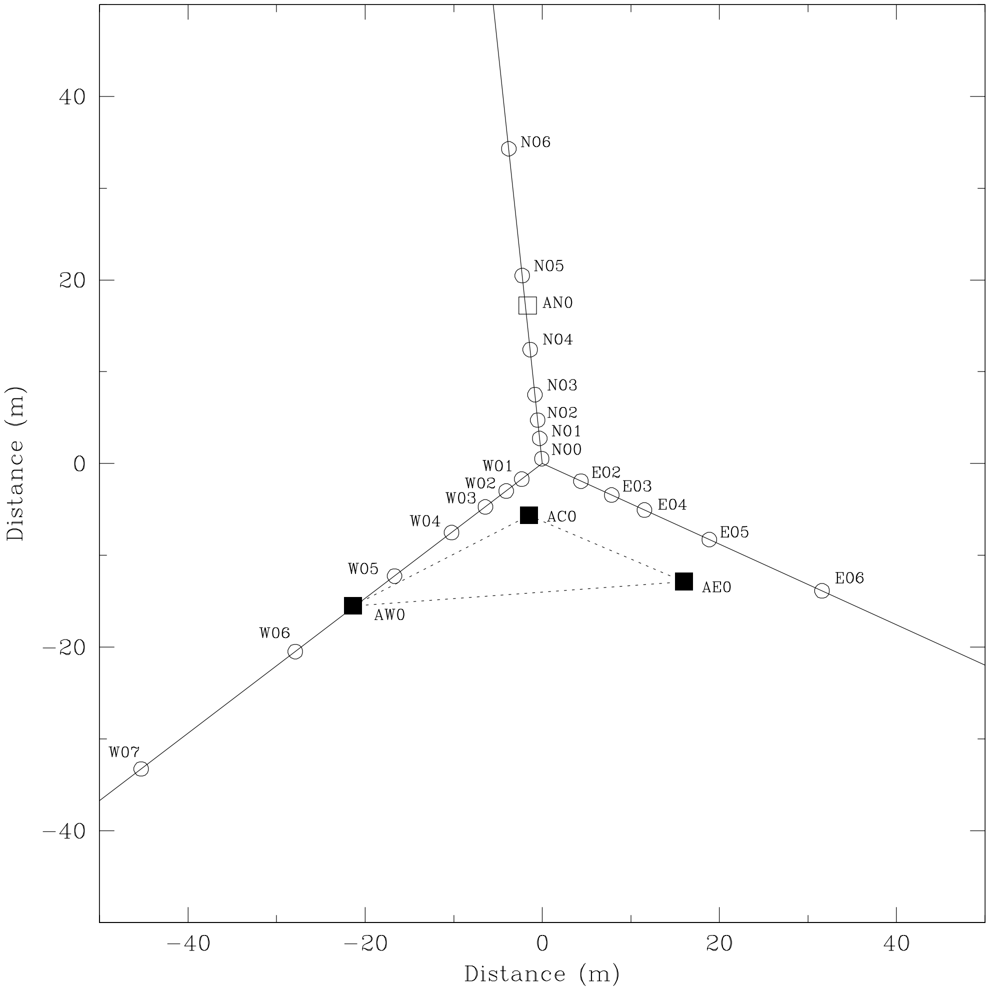

FIGURE 2.7: Same as Fig. 2.6, but concentrating only on the inner region of the layout. The imaging (*circles*) and the astrometric (*squares*) stations are shown. The three astrometric stations used in the observations presented in this dissertation are shown with filled squares. The resulting baselines (*dotted lines*) have lengths of 18.9 m, 22.2 m, and 37.5 m and are at azimuths of $-67\overset{\circ}{.}5$, $63\overset{\circ}{.}6$, and $86\overset{\circ}{.}0$, respectively.

TABLE 2.1: PROPERTIES OF THE ASTROMETRIC ARRAY

Station	Position† (m)		Baseline length (m)			
	East–West	North–South	AN0	AC0	AE0	AW0
AN0	−0.636	17.210	⋯	22.848	34.874	38.293
AC0	−0.504	−5.638	22.848	⋯	18.931	22.237
AE0	16.985	−12.885	34.874	18.931	⋯	37.470
AW0	−20.387	−15.596	38.293	22.237	37.470	⋯

† Positions are measured with respect to the center of the imaging sub-array.

available APDs was limited, not all spectral channels were recorded. Also, one of the spectral channels was reserved for the HeNe delay-line metrology laser, and thus was not available for the detection of the stellar signal.

Because the astrometric sub-array was in operation long before the imaging sub-array[8] or the six-way beam combination (Hummel et al., 2003) were implemented, most of the observations obtained by NPOI were done using only three astrometric stations. The possible baseline lengths that can be constructed using the four astrometric stations are listed in Table 2.1. It can be seen from the table that the astrometric sub-array alone gives access to baselines in the range of ∼19–38 m. For all of the observations presented in this dissertation, the three baselines formed by the AC0–AE0–AW0 triangle were used (see the dotted lines in Fig 2.7).

2.2.2 Interferometric Observables

In § 2.1 we have discussed how the degree of coherence between two beams in a simple interferometer depends on the spectral bandwidth and the spatially resolved structure of the source. Although both effects, at least in principle, can be measured simultaneously with long-baseline stellar interferometers, most instruments concentrate only on detecting the visibility loss due to the spatial structure. In the case of NPOI, only a small portion of the fringe pocket is actually sampled (in 8 bins per cycle of modulation) and thus the signal does not contain any detailed spectroscopic information. Furthermore, because the maximum and minimum intensities are not actually measured, equation (2.11) cannot be used directly to obtain the visibility amplitude from the contrast of the fringe. Instead, a Fourier transform of the photon counts from the 8 bins yields the real (X) and the imaginary (Y) parts of the complex visibility (Hummel

---

[8] The imaging sub-array is only partially implemented, and currently up to two imaging stations can be used in conjunction with the four astrometric stations.

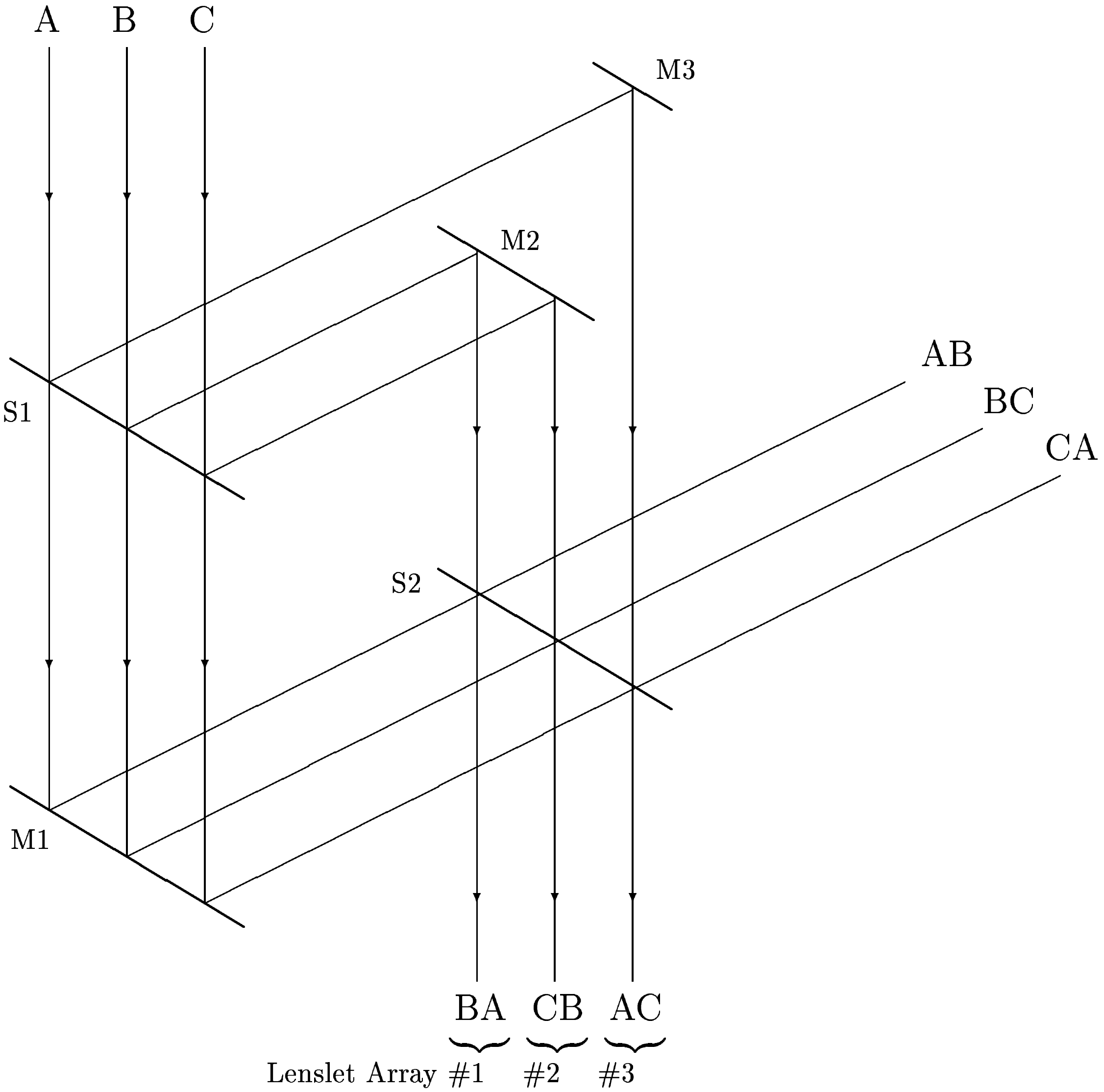

FIGURE 2.8: A pairwise beam combiner with three input beams. For the observations presented here only one side of the output was used. The S1 and S2 denote beam splitters and M1, M2, and M3 denote mirrors.

et al., 1998), which in turn are used to obtain the squared visibility using

$$V^2 = \left[\frac{4}{\mathrm{sinc}^2(\pi/n)}\right] \frac{\langle X^2 + Y^2 - \sigma^2 \rangle}{\langle N \rangle^2}, \tag{2.21}$$

where n is the number of bins across the fringe packet (currently $n = 64$), N is the total photon count rate (corrected for the background rate), and σ^2 is a bias term. Because it is easier to correct V^2 for the bias due to the noise (by subtracting σ^2) than it is to correct V, the V^2 is the preferred interferometric observable (Tango & Twiss, 1980). It is typically assumed that the bias term, σ^2, is solely due to the photon noise, which in the case of Poisson statistics implies that $\sigma^2 = N$. Although in practice this approach can remove a large fraction of the bias term, there are also other sources of non-Poisson noise due to instrumental effects, such as detector read noise, gain, and dead time (see also the discussion in Hummel et al., 2003).

The X and Y values can also be used to obtain the phase of the visibility, $\Phi = \arctan(Y/X)$, which unfortunately is corrupted by the atmosphere, although a significant fraction of the information contained in the phases can be recovered through the closure quantities. A closure quantity is typically calculated by multiplying the complex Fourier components, $X + iY$, from three baselines forming a closed triangle. This produces a triple amplitude ($V^{(3)}$) and a closure phase (Φ_{cl}), which is simply a sum of the phases for the individual baselines and is immune to the atmospheric phase delays affecting the individual elements. Therefore, a typical set of interferometric observables for NPOI consists of V^2, $V^{(3)}$, and Φ_{cl} for each spectral channel of all three baselines.

2.2.3 Initial Data Reductions

The OPD at the NPOI is modulated at 500 Hz, and therefore a different set of X and Y is produced for every 2 ms interval. The first step in the data reduction pipe-line involves averaging the numerator and the denominator in equation (2.21) for every 1 s interval, and computing the corresponding V^2 value (this is also known as incoherent averaging). In the case of the closure quantities, the complex triple product ($V^{(3)} \mathrm{e}^{\mathrm{i}\Phi_{\mathrm{cl}}}$) is first calculated for each 2 ms interval, and then 1 s averages are taken. The above steps are performed by a standalone C program called CONSTRICTOR, which then saves the 1 s records (data points) to a file that is read by the OYSTER[9] software package, where the data is further averaged (with some

---

[9] Optical Interferometer Script Data Reduction (OYSTER) software package written by Christian Hummel.

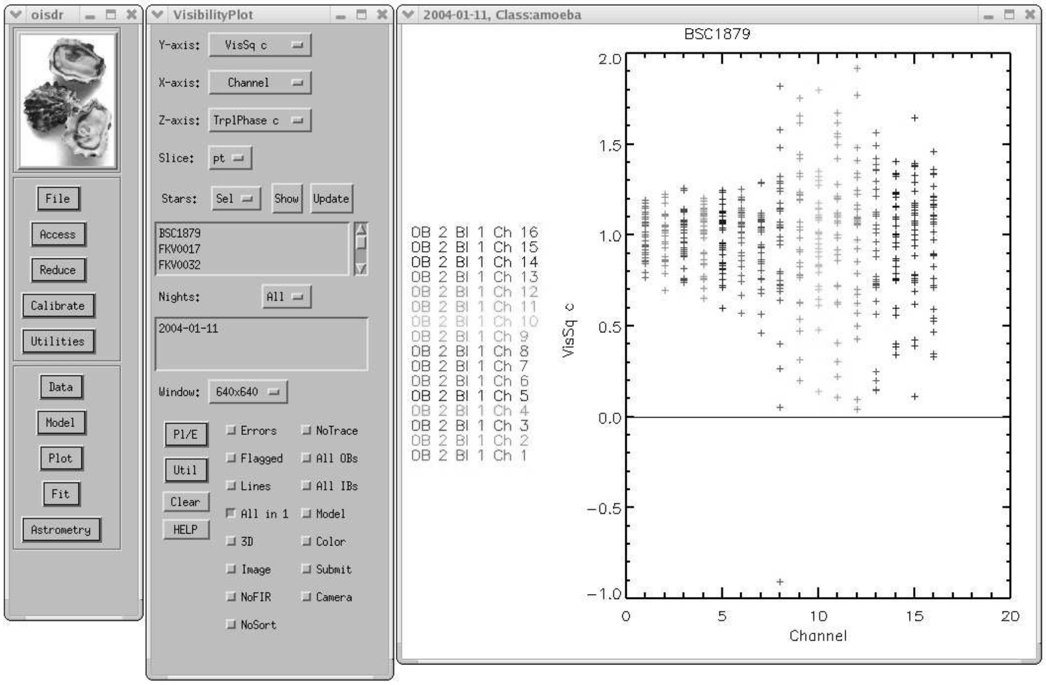

Y-axis: VisSq c

X-axis: Channel

Z-axis: TrplPhase c

Slice: pt

Stars: Sel

BSC1879
FKV0017
FKV0032

Nights: All

2004-01-11

Window: 640x640

☐ Errors
☐ Flagged
☐ Lines
☑ All in 1
☐ 3D
☐ Image
☐ NoFIR
☐ NoSort
☐ NoTrace
☐ All OBs
☐ All IBs
☐ Model
☐ Color
☐ Submit
☐ Camera

FIGURE 2.9: Screen-shot of the graphical user interface to the Optical Interferometer Script Data Reduction (OYSTER) software package. This software package handles all standard data reduction steps and produces raw or calibrated squared visibilities and closure quantities.

limited editing[10]) into 90 s scans, which are then saved as *raw scans*. The OYSTER software package can also be used to perform all of the standard[11] calibration and data visualization tasks via a graphical user interface (see Fig. 2.9).

The initial data reduction process that takes the raw 2 ms measurements and produces the uncalibrated 90 s scans, is part of the standard reduction pipe-line developed for the NPOI, and is typically conducted in relatively short time after the observations are acquired. Because the above process can reduce data file sizes from tens of Gbytes to few Mbytes per night, and if the initial 2 ms data files are not retained, these initial reduction steps can be used to reduce the disk storage requirements imposed by the observations. In fact, many of the archival observations that date back to 1997 only have the reduced 90 s scans available. Of course, the disadvantage of this approach is that the raw measurements are not available for all scans.

Although the data presented in this dissertation has not been calibrated using the OYSTER software package (i.e., a custom IDL program has been written that incorporates the

---

[10] Some 1 s data points are removed based on the recorded signals from system components such as laser metrology and narrow angle tracker that indicate bad data (Hummel et al., 1998).

[11] We define the standard calibration steps as those involving calibration of the interferometric observables with respect to an external calibrator.

calibration method presented in the next chapter), the uncalibrated 90 s scans were used as a starting point in the data analysis. The OYSTER package (in conjunction with CONSTRICTOR) not only averages V^2, $V^{(3)}$, and Φ_{cl} over the 90 s intervals, but also provides an estimate on the observational uncertainties associated with these quantities. These observational errors are set equal to the standard deviation of the 1 s data points, divided by the square root of the number of data points in a scan (see Hummel et al., 1998, for more details). Because this approach attempts to account for both the white and the non-white noise sources, it produces error bars that account for some of the atmospheric and instrumental effects. If some of these effects are removed from the data through subsequent calibration, these error bars will tend to overestimate the magnitude of the actual observational uncertainty.

2.3 Observing Be Stars

Interferometric observations of Be stars represent a unique class of observations. This is because a Be star can be modeled with a simple two component model. The stellar photosphere, which is visible at the continuum wavelengths, can be modeled with a UD model. This model is especially suitable for observations conducted at baselines of less than 40 m, since even if the stellar diameter would be 2 mas (this is larger than any angular diameter predicted for stars analyzed here), only a small part of the main lobe of the J_1 function would be actually sampled (recall Fig. 2.4), which is known to be almost completely insensitive to the limb darkening effects. The second component is the circumstellar region that is responsible for the Hα emission and although there is some contribution from this region at the continuum wavelengths, this contribution can be neglected in many cases.

We have described in § 2.1.4 how a uniform disk of angular diameter θ_{UD} has a visibility which is real and its amplitude is given by equation (2.20). To describe the Hα-emitting envelope we will use an elliptical Gaussian model. The normalized intensity on the sky for an elliptical Gaussian can be written as

$$I_{\mathrm{Gauss}}(\theta_{x'},\theta_{y'}) = \frac{4\ln 2}{\pi r\theta_{\mathrm{mj}}^2}\exp\left[-\frac{(\theta_{x'}^2/r^2+\theta_{y'}^2)}{\theta_{\mathrm{mj}}^2/(4\ln 2)}\right], \tag{2.22}$$

where r is the axial ratio, θ_{mj} is the angular size (FWHM) of the major axis (when $r < 1$), and $(\theta_{x'},\theta_{y'})$ are the sky coordinates in the direction of the minor and the major axes (see Fig. 2.10). The transformation between these coordinates and the ones in the east-west (θ_x)

and north-south (θ_y) directions on the sky is

$$\theta_{x'} = \theta_x \cos\phi - \theta_y \sin\phi, \tag{2.23}$$

$$\theta_{y'} = \theta_x \sin\phi + \theta_y \cos\phi, \tag{2.24}$$

where ϕ is the P.A. (measured east from north) of the major axis. A Fourier transform of equation (2.22) gives the visibility due to the Gaussian envelope and has the form:

$$V_{\mathrm{Gauss}}(u_{x'}, v_{y'}) = \exp\left[-\frac{\pi^2\theta_{\mathrm{mj}}^2(r^2u_{x'}^2 + v_{y'}^2)}{4\ln 2}\right], \tag{2.25}$$

where $u_{x'}$ and $v_{y'}$ are the spatial frequencies corresponding to $\theta_{x'}$ and $\theta_{y'}$, respectively. These frequencies can be easily expressed in terms of the spatial frequencies u and v using a similar coordinate transformation used for the sky coordinates:

$$u_{x'} = u\cos\phi - v\sin\phi, \tag{2.26}$$

$$v_{y'} = u\sin\phi + v\cos\phi. \tag{2.27}$$

If the two components, the UD and the elliptical Gaussian, are assumed to be concentric, then the net visibility for both components can be expressed as a normalized sum of equations (2.20) and (2.25), which can be written as

$$V_{\mathrm{UD+Gauss}} = c_{\mathrm{p}}\left[2\frac{J_1(\pi\theta_{\mathrm{UD}}s)}{\pi\theta_{\mathrm{UD}}s}\right] + (1-c_{\mathrm{p}})\exp\left[-\frac{\pi^2\theta_{\mathrm{mj}}^2(r^2u_{x'}^2 + v_{y'}^2)}{4\ln 2}\right]. \tag{2.28}$$

The c_{p} parameter in the above equation (that can have a value between 0 and 1) represents the net fractional contribution to total visibility from the UD, as well as it maintains the normalization of the net visibility. Of course if the two components are not concentric then the individual visibility amplitudes cannot be added in such as simple way, and one would have to account for the relative complex phase shifts between the models. This can also be explained as a result of a flux distribution that is not point-symmetric, and where the Fourier transform yields a complex quantity.

The model consisting of a UD and an elliptical Gaussian contains five free parameters. Because it is sometimes necessary to reduce the number of free parameters, a circular symmetry is assumed. This reduces the number of free parameters to three, and the resulting visibility for a UD and a circularly symmetric Gaussian (i.e., an elliptical Gaussian with $r = 1$) becomes:

$$V_{\mathrm{UD+Gauss}} = c_{\mathrm{p}}\left[2\frac{J_1(\pi\theta_{\mathrm{UD}}s)}{\pi\theta_{\mathrm{UD}}s}\right] + (1-c_{\mathrm{p}})\exp\left[-\frac{(\pi\theta_{\mathrm{mj}}s)^2}{4\ln 2}\right], \tag{2.29}$$

which is independent of the positional angle, ϕ, as expected.

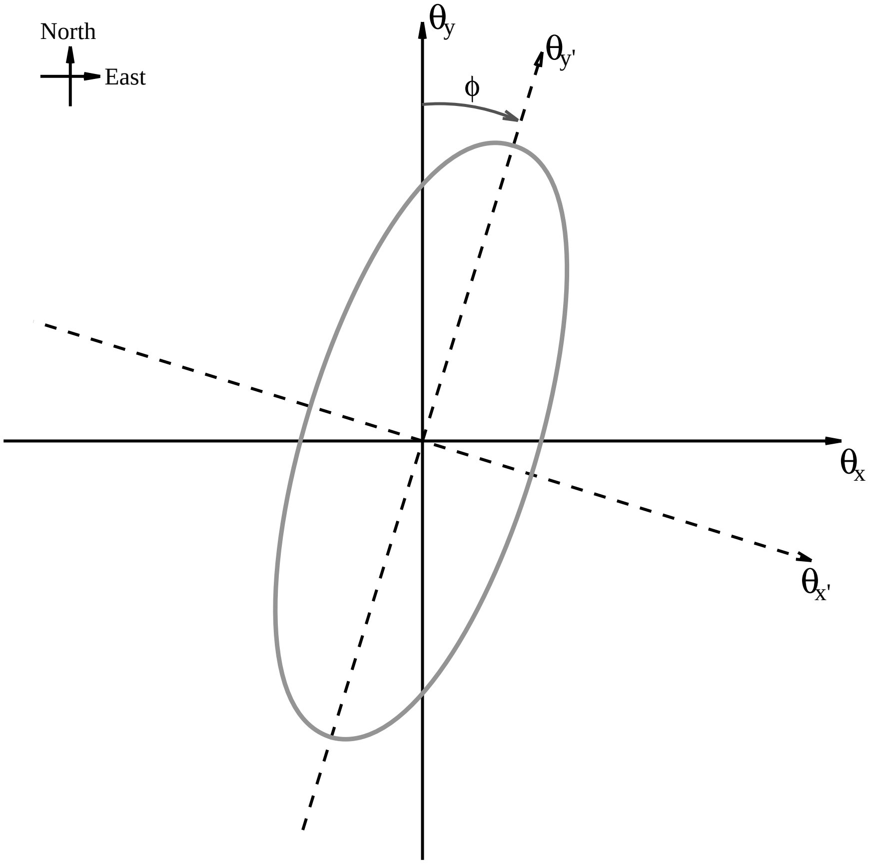

FIGURE 2.10: An ellipse representing the orientation of the elliptical Gaussian model on the sky.

Chapter 3

Internal Calibration of NPOI Data*

3.1 Introduction

The calibration of optical interferometry data is a continuing problem. A variety of instrumental and atmospheric effects combine to reduce the observed squared fringe visibility ($V^2_{\rm obs}$) from the source's intrinsic squared visibility ($V^2_{\rm src}$), and to affect both the triple-product amplitude ($V^{(3)}$) and closure phase ($\Phi_{\rm cl}$). Normally, observations of calibrator stars, for which $V^2_{\rm src}$ can be accurately estimated, are interspersed with observations of the program stars (see Benson et al., 1997, for an example). The observed squared visibility of the calibrator, $V^2_{\rm obs}({\rm C})$, is used to estimate a correction factor, $\Gamma^2 = V^2_{\rm obs}({\rm C})/V^2_{\rm src}({\rm C})$, which is then applied to the observed squared visibility of the program star, $V^2_{\rm obs}({\rm P})$, to obtain a calibrated quantity via $V^2_{\rm cal}({\rm P}) = V^2_{\rm obs}({\rm P})/\Gamma^2$.

Obviously, there are two limitations to this approach. First, a model is required that describes the calibration star with sufficient accuracy. In practice, this should not be a problem except possibly for observations on the longest baselines where there are few stars with simple, well-determined models. Second, Γ^2 can change with both time and angle on the sky. The ideal calibration observations, close to those of the program star in both time and angle, are not always possible.

It would be desirable to solve for the calibration corrections and the source characteristics from the observations of the program star alone. Of course, in general this is not possible since there are an infinite number of ways to divide a measurement $V^2_{\rm obs}$ between Γ^2 and $V^2_{\rm src}$. Nev-

---

*The material from this chapter has been published in the Astronomical Journal, vol. 125, pp. 3378–3388.

ertheless, there are classes of objects for which such a calibration technique can be successfully applied. The key idea is to generate a model for Γ^2 with as few parameters as possible, then to generate a model for at least some characteristics of the source with parameters that are orthogonal to the calibration parameters. With this orthogonality, both the calibration and the source characteristics can be obtained from the same data.

In this chapter, we implement one version of the calibration technique and apply it to archival observations from the Navy Prototype Optical Interferometer (NPOI) of the Be star γ Cassiopeiae (=HD 5394, B0 IVe). The NPOI, with multiple simultaneous baselines and numerous spectral channels, provides a rich data set for such a technique. We will concentrate mostly on the observed squared visibilities as a function of wavelength, although we will also consider the triple products and closure phases. We model the atmospheric and instrumental effects on the V^2 as quadratic functions in λ^{-1} and determine their net effect in eight continuum spectral channels. We then correct the data from the two channels that contain Hα emission and use those corrected data to determine the characteristics of the circumstellar envelope of γ Cas.

3.2 The Technique

The observed visibility, $V_{\rm obs}$, is the product of the visibility intrinsic to the source, $V_{\rm src}$, and the degradation of that visibility due to the atmosphere and the instrument, Γ. Normally, the observations at a single baseline consist of measuring simultaneously a number of squared visibility amplitudes in n spectral channels; thus,

$$V^2_{\rm obs}(\lambda_i) = \Gamma^2(\lambda_i) V^2_{\rm src}(\lambda_i), \tag{3.1}$$

where $i = 1, 2, ..., n$. Our procedure is to generate a model, Γ^2, for each set of simultaneously measured V^2-values of a single baseline, that will represent all $\Gamma^2(\lambda_i)$ with as few parameters as possible and will have a functional form that is orthogonal with respect to the source model. Because of this orthogonality, all of the time- and baseline-dependent Γ^2 functions, as well as $V^2_{\rm src}$, can be determined from the same observations.

For the Γ^2 model, we will assume a slow, monotonically increasing variation with wavelength. Because the degradation of $V^2_{\rm src}$ due to the atmosphere and the instrument can be represented by a Taylor series expansion in λ^{-1} (Porro, Traub, & Carleton, 1999), we decided to treat it as a quadratic function in λ^{-1}, and therefore

$$\Gamma^2(\lambda) = A_0 + A_1\lambda^{-1} + A_2\lambda^{-2}, \tag{3.2}$$

where A_i are time- and baseline-dependent constants. This is a good assumption for most interferometers built to date, including the NPOI (see also the discussion in § 3.4). However, for large aperture diameters, D, the quadratic description of Γ^2 might not be sufficient. This is because when the ratio D/r_0 is large (where r_0 is the Fried parameter) and the wave-front is not corrected by adaptive optics, a simple description of the wave-front distortion between the two elements as a simple residual tilt is no longer sufficient. In such a situation, higher order terms might be required to describe Γ^2 and model the atmospheric degradations effectively (see Berio et al., 1997, for more details).

Because the above technique requires both functions, Γ^2 and V^2_{src}, to have significantly different functional forms, it can be applied only in specific situations. Multiwavelength observations of a binary star system might be one of such situations. Observations obtained for a single baseline over a range of different wavelengths correspond to measurements at different spatial frequencies. These frequencies form a line through the origin in the Fourier (u, v)-plane. Along such a line, the observed V^2-values of a binary star system can be modeled using

$$V^2_{\mathrm{obs}}(\lambda_i) = \Gamma^2 V^2_{\mathrm{binary}} = \left(A_0 + A_1\lambda_i^{-1} + A_2\lambda_i^{-2}\right)\left[F_0(s_i) + F_1(s_i)\cos(2\pi\theta s_i)\right], \tag{3.3}$$

where θ is the angular separation of the pair projected along that line and s_i is the spatial frequency in the radial direction from the origin in the (u, v)-plane (i.e., $s_i \equiv |\boldsymbol{B}|/\lambda_i$, where $\boldsymbol{B}$ is the baseline vector). The F_i depend on the diameters and relative brightnesses of the components. If the observations at a single baseline cover a large enough range of wavelengths so that at least one full period of the cosine is observed, and the total number of independent data points is large, one can solve simultaneously for all six unknowns in equation (3.3).

Another situation in which the technique can be applied is the case of emission-line sources. If all of the emission of interest is restricted to one, or a few, spectral channels, then the other channels can be used to obtain the correction function Γ^2 which in turn can be used to calibrate the V^2-values in the spectral channels of interest. This type of model is a good approximation for Be stars and will be the focus of the rest of this chapter.

Because the atmospheric and instrumental signatures, as well as the signature due to the stellar photospheric disk (assumed to be unresolved or only slightly resolved), are present in all the spectral channels, they cannot be treated separately. Therefore, for the spectral channels containing only continuum radiation from the central star, the observed squared visibilities can be expressed as

$$V_{\mathrm{obs}}^2 = \Gamma^2 V_{\mathrm{UD}}^2, \tag{3.4}$$

where we have assumed that the stellar photospheric disk can be represented by a uniform disk (UD) model whose V^2-values are given by

$$V_{\mathrm{UD}}^2 = \left[2 \frac{J_1(\pi \theta_{\mathrm{UD}} s)}{(\pi \theta_{\mathrm{UD}} s)} \right]^2, \tag{3.5}$$

for a UD of angular diameter θ_{UD}, and where J_1 is the first-order Bessel function.

The quadratic function in λ^{-1} used for Γ^2 can equally well model the V^2-values for a UD component, and therefore equation (3.4) cannot be used to solve for both Γ^2 and V_{UD}^2 from the same observations (the special case where the squared visibilities from a single baseline span the zero crossing of J_1 for well-resolved sources might be an exception). At the same time, if the angular diameter for the stellar photospheric component is known (or can be estimated), equation (3.4) can be used to solve for the constants required to describe the polynomial Γ^2 from the continuum channels alone. After the correction factor Γ^2 is obtained for a specific baseline, it can then be applied to the V^2-values in the spectral channels of interest to calibrate out any atmospheric and instrumental signatures via

$$V_{\mathrm{cal}}^2 = V_{\mathrm{obs}}^2 / \Gamma^2, \tag{3.6}$$

where in this case the observed V^2-values are from the spectral channels with contributions from both the stellar photosphere (as UD) and an optically thin circumstellar envelope (see also the discussion in § 3.6) and can be written as

$$V_{\mathrm{obs}}^2 = \Gamma^2 (V_{\mathrm{UD}} + V_{\mathrm{env}})^2. \tag{3.7}$$

3.3 Observations

The NPOI has been described in detail by Armstrong et al. (1998). For the observations presented in this study three astrometric elements were used, which provided baselines of 18.9, 22.2, and 37.5 m at azimuths (measured east from north) of $-67\overset{\circ}{.}5$, $63\overset{\circ}{.}6$, and $86\overset{\circ}{.}0$, respectively (recall Fig 2.7). A detailed description of the observational approach and the initial data reduction procedure has been provided elsewhere (see, for example, Benson et al., 1997).

The observational data are collected in the form of "scans," where one scan corresponds to data obtained simultaneously from n separate spectral channels at each of the three baselines. Each scan contains the average of ~90 s of data from which fringe parameters, the V^2-values and the closure quantities, are derived. If we define an "observation" to correspond to a single point in the (u, v)-plane, then a single scan produces three different observations per spectral channel. The instrumental configuration at NPOI was such that the Hα profile at 656.3 nm, which for Be stars can have a full width of more than 2 nm (Banerjee et al., 2000), overlapped two spectral channels with central wavelengths at 648 and 665 nm, and widths of 16 and 17 nm, respectively. In the data presented in this study, 10 channels were analyzed, with the channels containing Hα positioned in the middle of the group.

Before we can work with the calibrated V^2 from the two channels that contain Hα emission, we must first combine the signals from both. We need to consider the average signal not only because the fractional contribution from the Hα emission in each channel is not known exactly, but also because the contribution in each channel can change slightly during the night as a result of changes in the projected radial velocity and, potentially, because of thermal shifts in the beam-dispersing optics.

The correct way to generate a combined spectral channel is to add the bin counts. Since the raw data are not available (recall § 2.2.3), it is necessary to estimate the visibility for the combined channel from the visibilities measured in the individual narrow channels. The visibility $V_{\mathrm{H}\alpha}$ measured in the combined Hα channel is related to the visibilities V_1 and V_2 measured in the individual channels by

$$\langle N_{\mathrm{H}\alpha} V_{\mathrm{H}\alpha} \rangle = \langle N_1 V_1 + N_2 V_2 \rangle, \tag{3.8}$$

where N_1 and N_2 are the counts in the respective channels and we are assuming that the phase in each channel is the same. Because $N_1 \sim N_2$ this is equivalent to averaging the visibility amplitudes,

$$\langle V_{\mathrm{H}\alpha} \rangle^2 = \left(\frac{1}{2} \sqrt{\langle V_1 \rangle^2} + \frac{1}{2} \sqrt{\langle V_2 \rangle^2} \right)^2 . \tag{3.9}$$

Our scientific target, γ Cas, was observed on four different nights. Table 3.1 lists the dates for those nights, the number of observations obtained on each night for the combined Hα channel, and the range of positional angles (P.A.'s) these observations cover on the sky. Figure 3.1 shows the corresponding Fourier (u, v)-plane coverage in the Hα channel for all four nights.

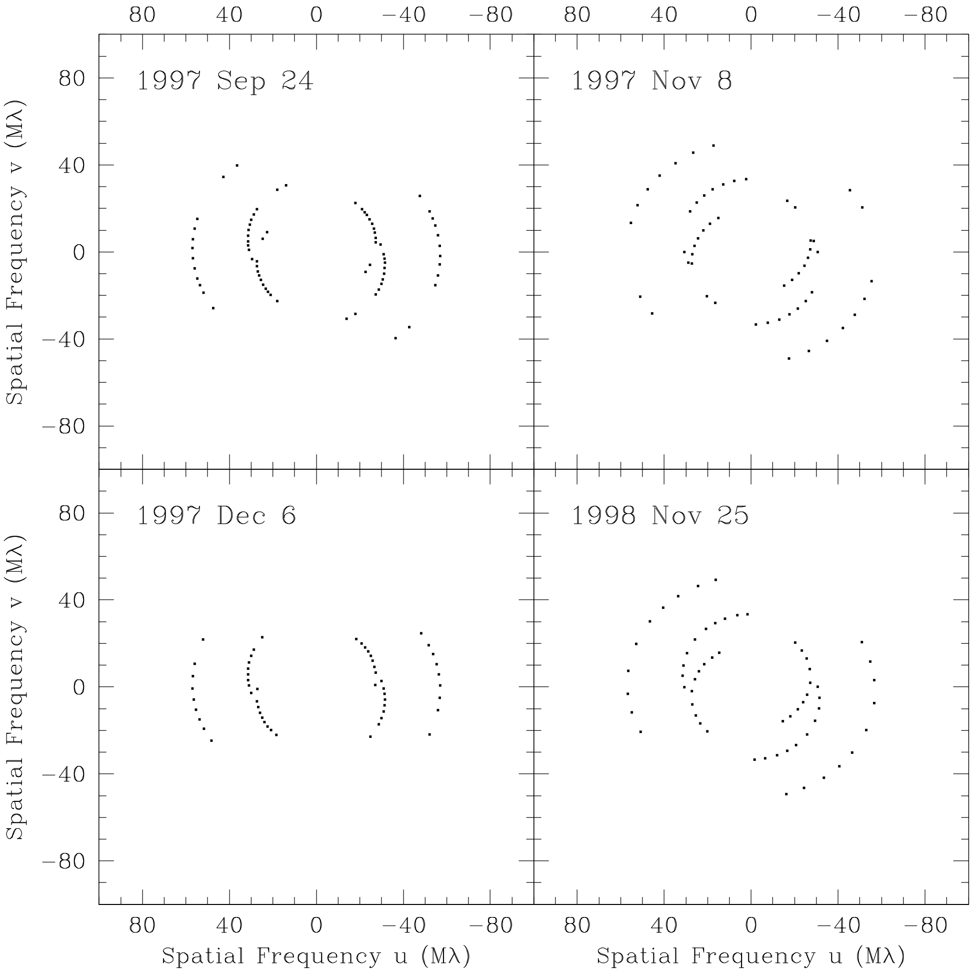

FIGURE 3.1: The Fourier (u, v)-plane coverage in the Hα channel for γ Cas on four nights of observations.

TABLE 3.1: NPOI OBSERVATIONS OF γ CASSIOPEIAE

Date	JD	N_{obs}	P.A. Coverage[†] (deg)
1997 Sep 24	2,450,716	36	24.4 – 141.5
1997 Nov 8	2,450,761	27	3.9 – 144.7
1997 Dec 6	2,450,789	27	47.6 – 140.2
1998 Nov 25	2,451,143	30	2.8 – 135.4

[†] Angles measured east from north.

3.4 Application to β Cassiopeiae

Before we apply our technique to a star with Hα emission, we analyze a star without emission as a null test of our methodology. For this purpose we use a calibrator star, β Cas (=HD 432; F2 III), whose observations were interleaved with those of γ Cas on 1997 September 24 and are shown in Figure 3.2*a*. Although β Cas is a variable star of δ Scuti type, the peak-to-peak amplitude variation is only ~0.031 mag with a period of ~2.4 hr (Riboni, Poretti, & Galli, 1994). Nordgren et al. (1999) give a UD angular diameter for β Cas of 2.05 ± 0.05 mas, and thus the star is partially resolved by our Fourier (u, v) coverage. The expected V^2-values for a UD of angular diameter of 2 mas are shown in Figure 3.2 (*dashed lines*).

Because of its spectral type, β Cas is not expected to have a significant Hα emission in the two spectral channels with central wavelengths at 648 and 665 nm (see also the low resolution spectrum shown by Torres-Dodgen & Weaver, 1993). We can expect the two channels to behave similarly to the channels containing mostly continuum radiation from the star. Therefore, we can use up to 10 spectral channels to fit for Γ^2. Instead, for consistency with the γ Cas reductions, we analyzed β Cas in exactly the same way (i.e., only the four shortest and four longest wavelength channels were used).

The squared visibilities of a partially resolved UD decline with spatial frequency s in a very similar way to the atmospheric and instrumental degradations. Because we are interested in how well the quadratic polynomial we use to describe Γ^2 can model the degradations, we can also model the signature of the UD component in the process. Applying such a polynomial to $V^2_{\rm obs}$ removes the signature of the stellar angular diameter as well as the signature of the degradations, and the resulting V^2-values should cluster around unity. Figure 3.2 shows all 10 channels for each available scan, before and after the correction by the quadratic polynomial that represents $\Gamma^2 V^2_{\rm UD}$. By looking at the individual scans in Figure 3.2*a* it is apparent that a simple linear expansion for Γ^2 is not sufficient to model the atmospheric and instrumental degradations at each baseline.

In Figure 3.3*a*, we show the residuals $(V^2_{\rm cal}/V^2_{\rm UD} - 1)$, while Figure 3.3*b* shows the residuals normalized by the uncertainties of $V^2_{\rm obs}$. The residuals are smaller than the uncertainties of the visibilities, indicating that at each baseline $V^2_{\rm obs}(\lambda)$ is well represented by quadratic polynomial. This is also seen in Table 3.2, which lists the weighted means and standard deviations of the residuals in each channel. Most of the deviations from zero are less than 1%, and can be

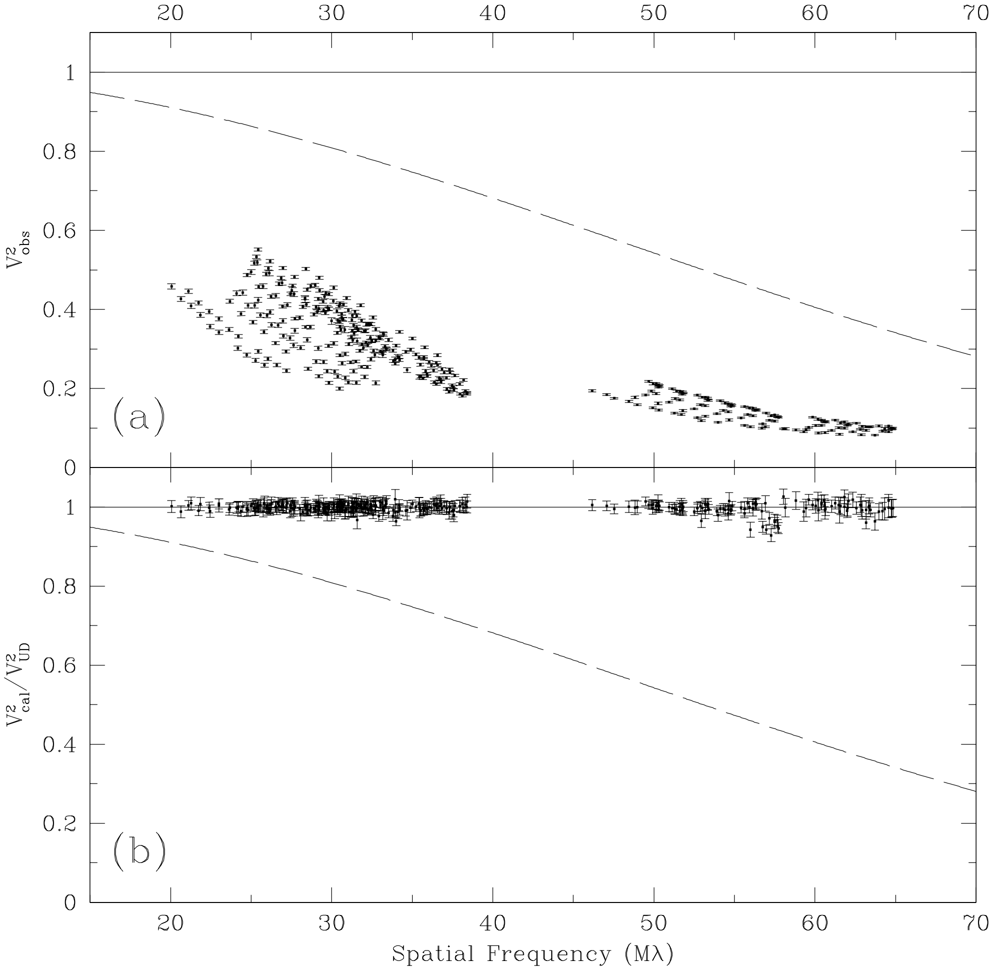

FIGURE 3.2: Null test of internal calibration using the observations of the control star β Cas obtained on 1997 September 24. (*a*) Uncalibrated squared visibilities as a function of spatial frequency $s \equiv \sqrt{u^2+v^2}$ for 10 spectral channels. The V^2-values for an unresolved source (***solid line***) and a 2 mas UD model (***dashed line***) are also shown. (*b*) Same data as in (*a*), but after division by quadratic polynomials representing the Γ^2 degradation factors and the stellar photospheric disk. The polynomials were generated from the four shortest and four longest wavelength channels. Note that the $V^2_{\rm cal}/V^2_{\rm UD}$ values lie on the solid line for all values of spatial frequency, including those that were not used to generate the polynomials.

attributed to errors in the bias corrections. The relatively large (at the 2% level) scatter present in the 648 nm channel may be due to contamination by scattered light from the HeNe delay-line metrology laser, which also makes the adjacent 633 nm channel unusable.

The spectral channel at 648 nm is one of the channels making up the wide Hα channel discussed in § 3.3, and therefore, any contamination by the laser light can potentially influence our final results. Although this could be the major source of error in our final results, we expect it to be of the same order of magnitude as the error due to the bias correction, especially after the two spectral channels used to calculate the Hα channel are averaged together.

3.5 Application to γ Cassiopeiae

Our scientific target, γ Cas, is a well-known Be star. Its relatively strong Hα emission has been detected by many observers. More importantly, the Hα emission line is the strongest emission feature in the spectral region between ~573 and ~755 nm (see for example the low resolution spectra shown by Quirrenbach et al. (1997) and Johnson, Wiśniewski, & Faÿ, 1978). Be stars can also exhibit weak emissions (relative to Hα) in the Paschen series, O I, Ca II, Fe II or He I lines, but because of our relatively wide spectral channels (12–22 nm), the contribution from these emissions is insignificant relative to the stellar photospheric signal. Thus, for the purpose of our scientific measurements, we are only concerned with the Hα emission.

The circumstellar envelope of γ Cas also emits continuum radiation that is present in all spectral channels. This extra signal is due to free-free and bound-free hydrogen emission, and it becomes more significant with increasing wavelength (Telting et al., 1993). In fact, even at 550 nm it can already represent 10% of the total flux, and it increases to 16% at 750 nm (Poeckert & Marlborough, 1978; Doazan, 1982). Because there are no ionization edges in our spectral region covering 573–755 nm, the free-free and bound-free emission, and perhaps also a component due to scattered flux, are expected to vary smoothly as a function of wavelength.

In the absence of the continuum radiation from the envelope, we expect all V^2-values to be well represented by those predicted for the UD model, which has no functional dependence on the P.A. of the projected baseline and is only slightly resolved even with our longest baseline. In the presence of the continuum radiation from the envelope, we expect the data to deviate only slightly from the UD model visibilities, since the size of the emitting region at the continuum wavelengths is known to be much smaller (since higher densities are needed) than that

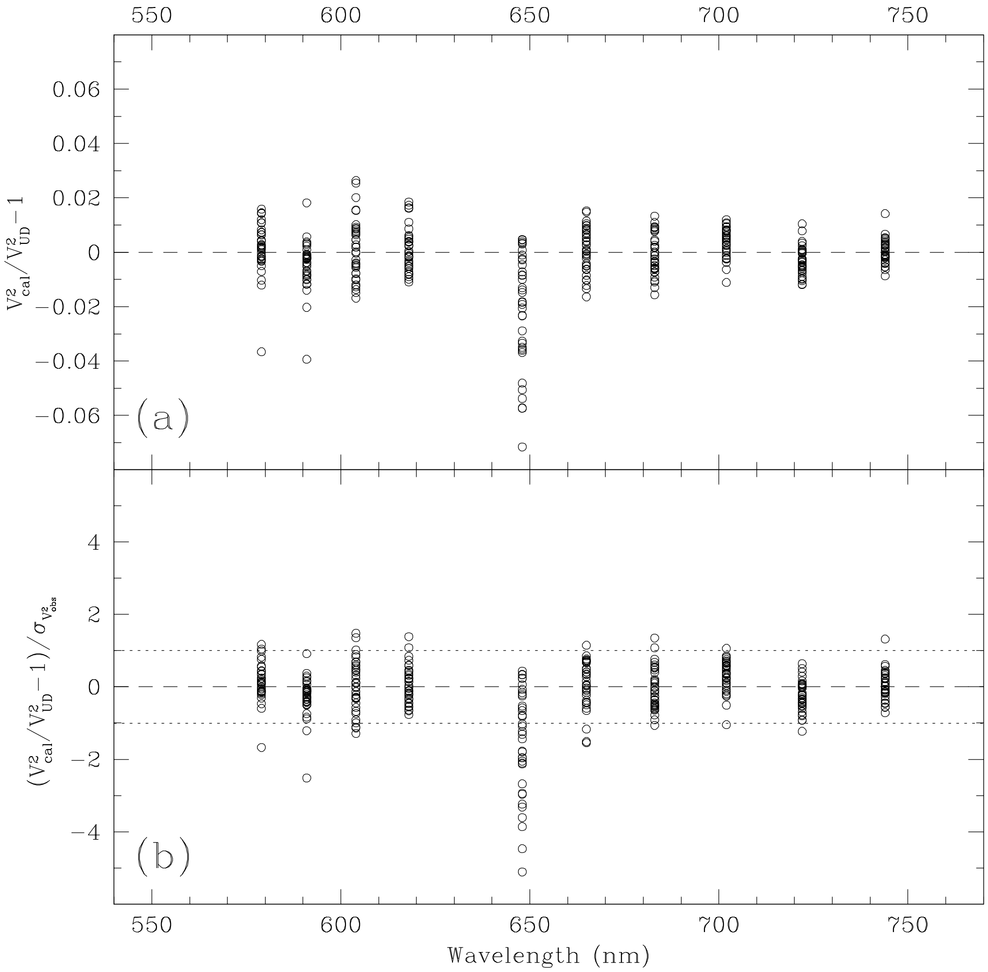

FIGURE 3.3: (*a*) Residuals of the data shown in Fig. 3.2*b* plotted as a function of the central wavelengths of the spectral channels. (*b*) Same residuals as in (*a*), but normalized by the corresponding observational uncertainties. The ±1σ deviation is indicated by the dotted lines.

TABLE 3.2: WEIGHTED MEANS AND STANDARD DEVIATIONS OF THE RESIDUALS FOR β CASSIOPEIAE

λ (nm)	$\langle V^2_{\mathrm{cal}}/V^2_{\mathrm{UD}} - 1\rangle$	$\sigma_{\mathrm{residual}}$
579	0.0032	0.0077
591	−0.0042	0.0078
604	−0.0002	0.0100
618	0.0007	0.0066
648	−0.0198	0.0182
665	0.0006	0.0076
683	−0.0007	0.0065
702	0.0038	0.0048
722	−0.0031	0.0044
744	0.0005	0.0040

corresponding to the Hα emission (see Stee et al., 1998, for an example). Therefore, we expect the variations in V^2-values across different spectral channels, due to changing continuum flux contribution from the envelope, to be very similar to the signature due to the UD, and this effect should not influence our analysis in any significant way.

Quirrenbach et al. (1997) have estimated that the angular diameter of the stellar photosphere of γ Cas is 0.56 mas using the Barnes-Evans relation (Barnes & Evans, 1976; Barnes et al., 1978). An angular diameter of a star (especially of a main sequence star) can be estimated quite accurately using its magnitude and color because tight relationship between the surface brightness and the photometric color exists (van Belle, 1999; Mozurkewich et al., 2003). For the (u, v)-plane coverage shown in Figure 3.1, the adopted stellar diameter does not significantly affect the following analysis since diameters smaller than $\sim$1 mas are too small to be significantly resolved with our current baselines (see also discussion in § 3.7.2). Therefore, for the purpose of the analysis presented in this study, we have adopted $\theta_{\rm UD} = 0.56$ mas as a *representative* angular diameter of the stellar disk of γ Cas.

Figure 3.4 shows eight continuum channels, for each available scan, before and after the correction by Γ^2. The predicted squared visibilities of the stellar photospheric component (assumed to be UD) used in our correction scheme are shown as the solid line. The calibrated V^2-values (Fig. 3.4*b*) at all spatial frequencies except those of the Hα channels are consistent with a single UD model. Applying the correction factors Γ^2, obtained from the eight continuum channels, to the V^2 of the two channels containing the Hα emission gives much different results. Figure 3.5 shows the V^2 in these two channels before and after the application of equation (3.6) to the data. The V^2 with the calibration applied (Fig. 3.5*b*) clearly fall below the UD curve, showing that the circumstellar envelope is extended. Figure 3.6 shows the average of the two channels with the Hα emission, also with the calibration applied. These squared average visibilities for the Hα channel ($V^2_{\rm H\alpha}$) can now be used for modeling the circumstellar envelope.

3.6 Modeling the Circumstellar Envelope of γ Cassiopeiae

We fit a simple model to the squared-visibility data consisting of a combination of a UD model and an elliptical Gaussian for the stellar and the envelope components, respectively. We are assuming that the two components are concentric and therefore we can use equation (2.28) to

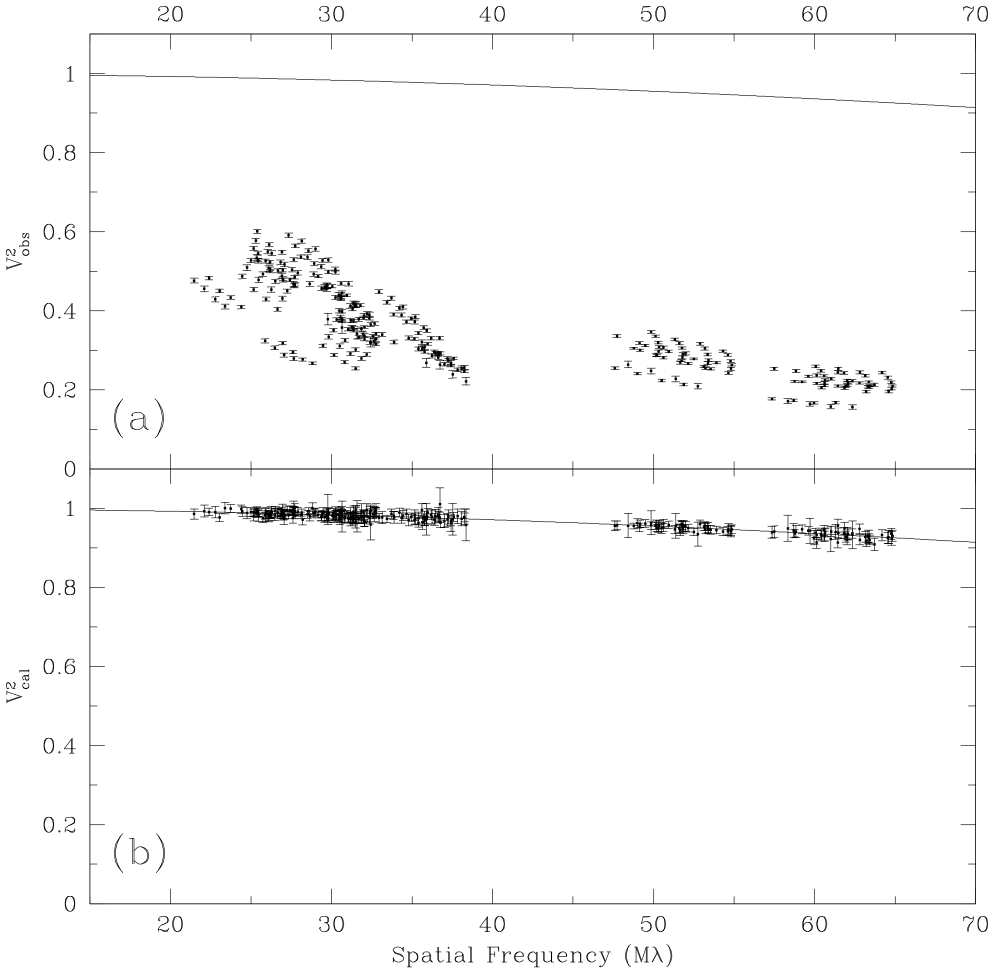

FIGURE 3.4: (*a*) Uncalibrated squared visibilities for γ Cas measured on 1997 September 24, as a function of spatial frequency s for all spectral channels, but excluding the two channels that contain Hα emission. The solid line corresponds to eq. (3.5) for $\theta_{\mathrm{UD}} = 0.56$ mas. (*b*) Same as (*a*), but after the application of eq. (3.6) to the data.

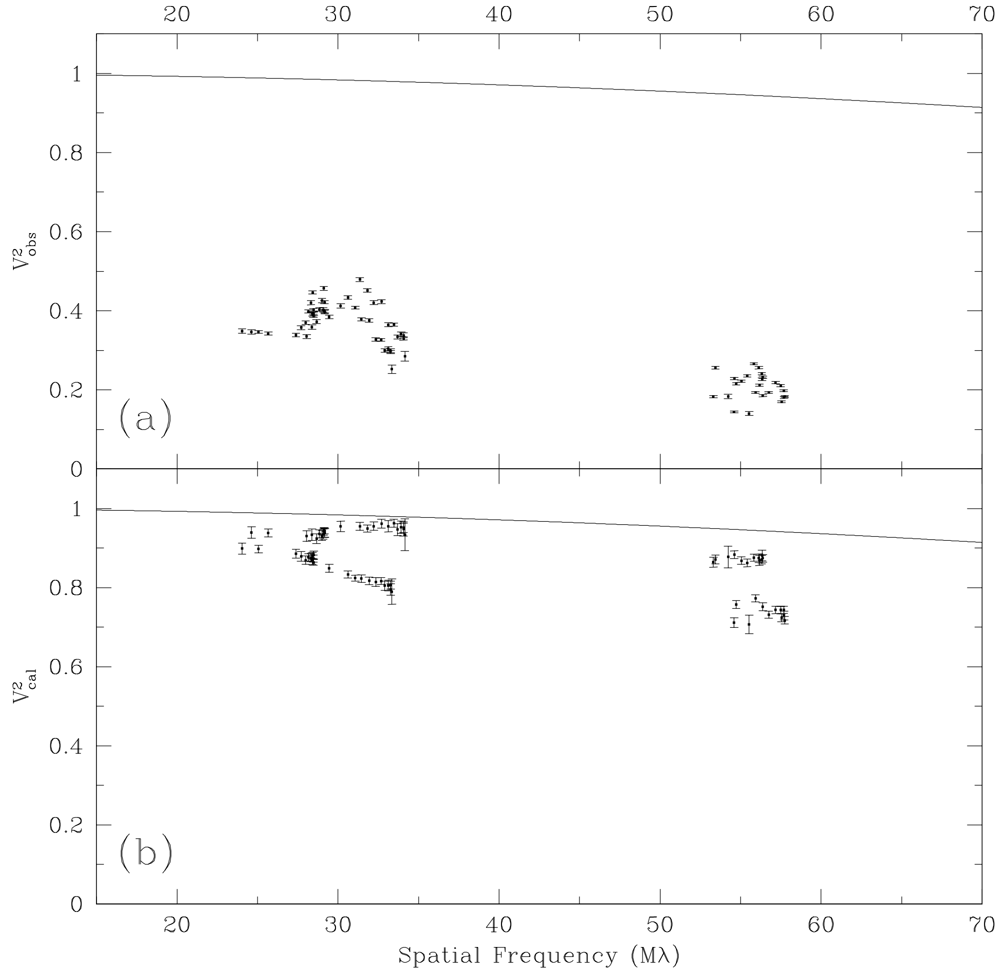

FIGURE 3.5: Same as Fig. 3.4, but for only the channels with central wavelengths at 648 and 665 nm. Note that the observed V^2-values for these two channels were not used to derive the Γ^2 degradation factors needed in eq. (3.6) to obtain the V^2_{cal}.

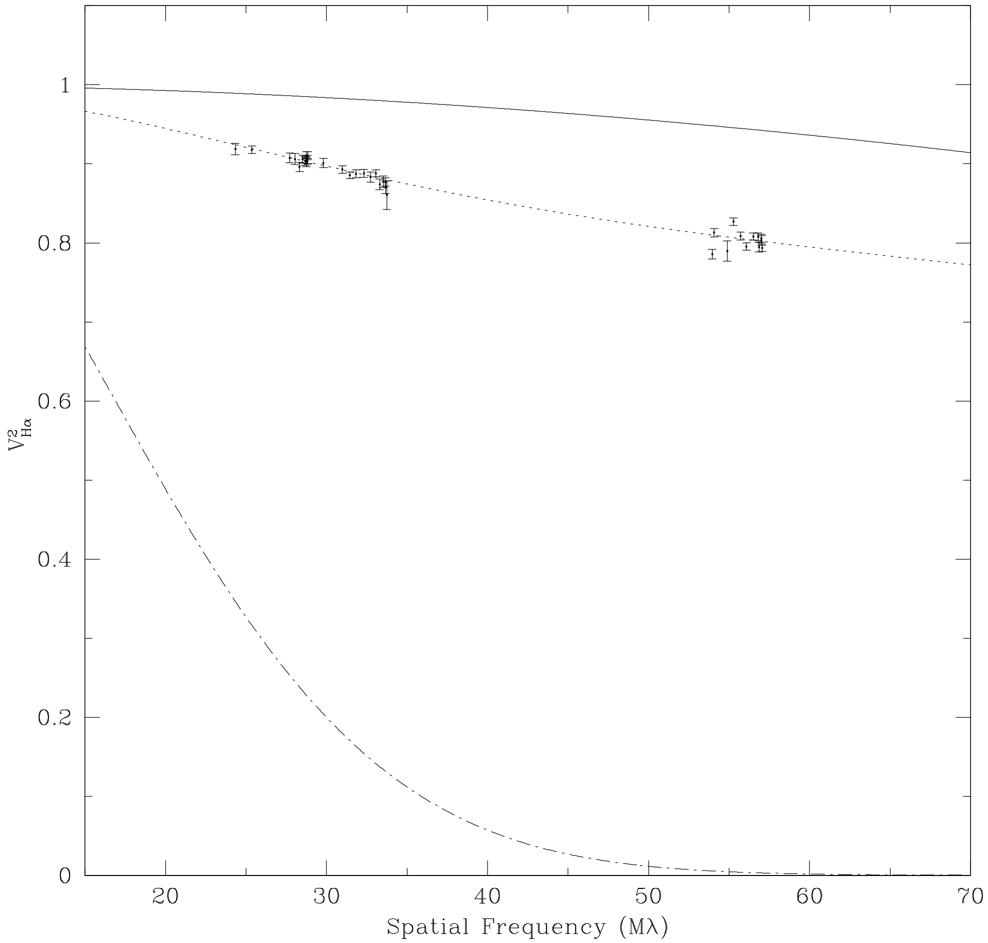

FIGURE 3.6: Squared average visibilities for the two channels shown in Fig. 3.5 for the night of 1997 September 24, calculated from the calibrated visibilities of Fig. 3.5*b*. Shown are the stellar model (*solid line*), the circularly symmetric Gaussian (*dash-dotted line*), and the best-fit (*dotted line*) of the combination of the two models to the data given by eq. (3.10).

TABLE 3.3: PARAMETERS FOR THE BEST-FIT MODELS OF γ CASSIOPEIAE

Date	$\theta_{\rm mj}$ (mas)	r	$\phi^\dagger$ (deg)	$c_{\rm p}$	χ^2_ν
1997 Sep 24	3.27 ± 0.07	1	...	0.918 ± 0.002	1.89
	3.54 ± 0.15	0.89 ± 0.04	25 ± 12	0.918 ± 0.002	1.67
1997 Nov 8	3.25 ± 0.09	1	...	0.907 ± 0.003	1.62
	3.45 ± 0.11	0.78 ± 0.06	39 ± 7	0.908 ± 0.003	0.95
1997 Dec 6	3.48 ± 0.09	1	...	0.922 ± 0.002	1.30
	3.93 ± 0.25	0.85 ± 0.06	30 ± 14	0.922 ± 0.002	0.95
1998 Nov 25	3.28 ± 0.14	1	...	0.916 ± 0.003	2.45
	3.76 ± 0.18	0.62 ± 0.06	34 ± 5	0.917 ± 0.003	0.97

[†] Measured east from north.

write our model squared visibility as

$$V^2_{\rm model} = \left\{ c_{\rm p} \left[2\frac{J_1(\pi\theta_{\rm UD}s)}{\pi\theta_{\rm UD}s} \right] + (1-c_{\rm p}) \exp\left[-\frac{\pi^2\theta^2_{\rm mj}(r^2u^2_{x'} + v^2_{y'})}{4\ln 2} \right] \right\}^2 , \qquad (3.10)$$

where $\theta_{\rm UD}$ is the uniform disk diameter of the central star, $c_{\rm p}$ is the net fractional contribution from the photosphere in the Hα channel, $\theta_{\rm mj}$ is the angular size of the major axis (FWHM) of the elliptical Gaussian representing the line emission, and r is the axial ratio. The spatial frequencies $u_{x'}$ and $v_{y'}$ can be expressed in terms of the spatial frequencies u and v, as well as the P.A. of the major axis, ϕ, via $u_{x'} = u\cos\phi - v\sin\phi$ and $v_{y'} = u\sin\phi + v\cos\phi$, respectively (see also § 2.3).

We have used a nonlinear, least-squares fit based on the Levenberg-Marquardt method, provided by the Interactive Data Language (IDL), to obtain the best-fit values for all the parameters on four different nights. The list of the best-fit parameters for all of our models is given in Table 3.3. The rows indicated by a fixed r-value of unity correspond to the circularly symmetric models with only two free parameters.

The best-fit values for the angular size of the major axis of the elliptical models substantially, and systematically, differ from the parameters of the best-fit circularly symmetric models. Also, the relatively high χ^2_ν (per degree of freedom) values that we obtained for the symmetric models suggest that the elongation is real. Figure 3.7 shows the typical deviations between the circularly symmetric and the elliptical models, along with the observations for the night of 1997 November 8. If we plot the calibrated V^2-values for any night with the contribution due to the UD removed, as a function of P.A. of the projected baseline, then there is a marked angle

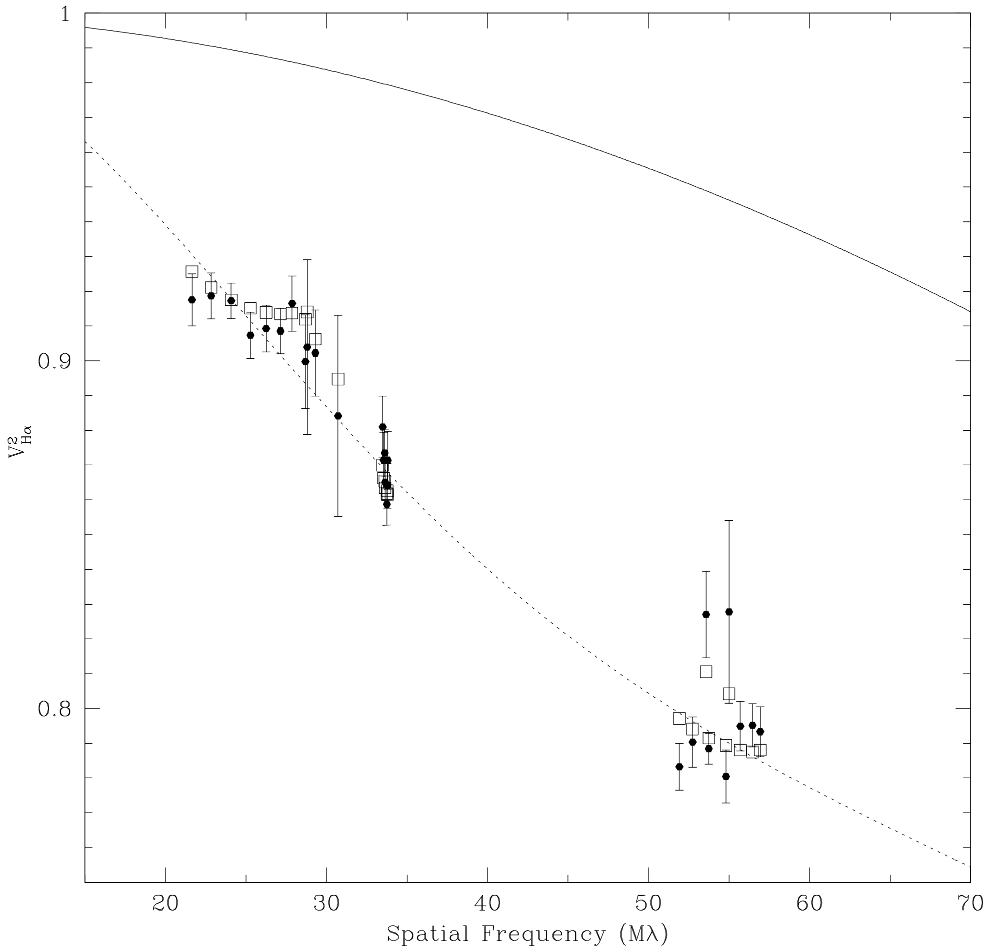

FIGURE 3.7: Same as Fig. 3.6, but for the night of 1997 November 8. The squares indicate the best-fit elliptical Gaussian model.

dependence (see Fig. 3.8, for example). The V^2-values tend to be diminished at smaller angles, which indicates that the envelope is larger and more resolved at those P.A.'s. The envelope seems to be elongated with a P.A. somewhere between 20° and 50°.

In principle we could fix the value of the fractional photospheric contribution $c_{\rm p}$ based on independent spectrophotometric information. Because the wavelength calibration and spectral response of each channel is not known with high precision, and the emission-line strength and profile may vary on timescales of hours to months (see, for example, Telting et al. (1993) and Smith, 1995), this is not a good idea. Thus, we chose to allow the $c_{\rm p}$ to vary in order to take these factors into account.

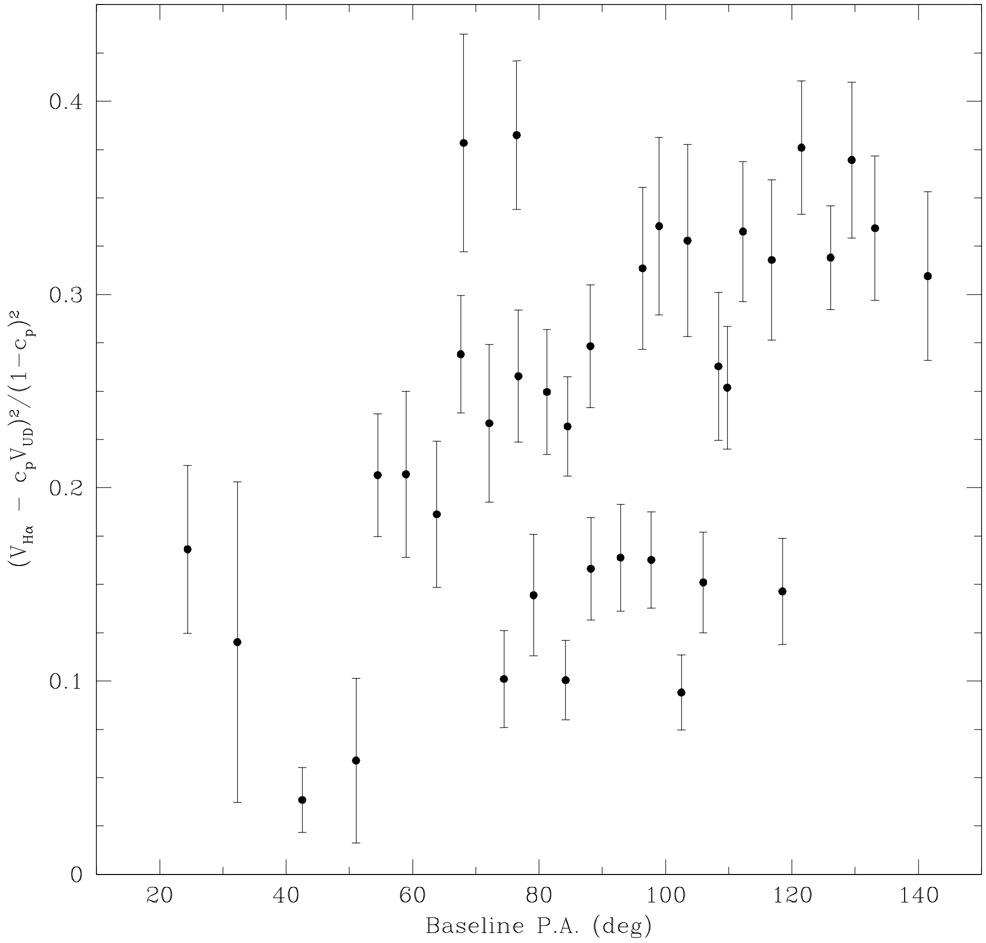

FIGURE 3.8: Squared visibilities for the Hα channel of γ Cas as a function of baseline positional angle after the stellar photospheric contribution has been removed. Data are shown for the night of 1997 September 24.

We can estimate the expected value for the c_{p} parameter using the equivalent width (EW) of Hα emission line and the total width of the spectral channel (TW), where

$$c_{\mathrm{p}} \sim \frac{\mathrm{TW} - |\mathrm{EW}|}{\mathrm{TW}}. \tag{3.11}$$

Using the EW of -2.25 nm for Hα observed by Banerjee et al. (2000) only a month after our last observation and accounting for the stellar Hα absorption profile, which has an EW of $\sim$0.25 nm (Coté & Waters, 1987) and has also been filled in, we obtain a rough estimate for the *net* emission in Hα due to the envelope of about -2.5 nm. Because the TW of the Hα channel is about 33 nm, we expect $c_{\mathrm{p}} \sim 0.92$, which is in excellent agreement with our best-fit values shown in Table 3.3.

The P.A. of the major axis of the elliptical Gaussian was the only parameter for which we could not estimate an uncertainty from the nonlinear least-squares fit alone. This is directly related to the fact that P.A. parameter is not well constrained by our observations, because we have very limited Fourier (u, v)-plane coverage as shown in Figure 3.1. We decided to apply Monte Carlo analysis (Press et al., 1992) to estimate the uncertainties by simulating 10,000 synthetic data sets for each night, based on the model parameters listed in Table 3.3. The uncertainties for the P.A.'s listed in Table 3.3 are estimated from the synthetic data sets, and it is evident that the nights with more extended and uniform (u, v)-plane coverage, also have smaller uncertainties for P.A.'s.

3.7 Discussion

3.7.1 The Circumstellar Envelope

The best-fit parameters for the elliptical Gaussian for the four different nights are listed in Table 3.3. There is no clear signature of variability of any kind, even though the observations span more than 1 year. The angular sizes of the major axis all agree with each other within 1–2 standard deviations. The P.A. of the major axis also seems to be constant from night to night. The axial ratio does seem to change slightly, especially for the fourth night, which could be due to slight asymmetries associated with the circumstellar region, but it could also be caused by our limited (u, v)-plane coverage.

The distance to γ Cas is known to be 188 ± 20 pc from the *Hipparcos* parallax of 5.32 ± 0.56 mas (ESA, 1997). If we assume that the size of the emitting region does not change in time, we can then take our average angular size of the major axis of 3.67 ± 0.09 mas and relate it to an actual size of $(1.03 \pm 0.12)\times 10^{11}$ m (or $\sim$148 $R_\odot$). Our *representative* stellar angular diameter of 0.56 mas corresponds to 1.6×10^{10} m (or $\sim$23 $R_\odot$) at the same distance.

Our average value of 3.67 ± 0.09 mas for the angular size of the major axis compares reasonably well to 3.47 ± 0.02 mas obtained by Quirrenbach et al. (1997), who observed γ Cas with 1 nm and 10 nm filters centered on Hα. Our ensemble average values of $32^\circ \pm 5^\circ$ for P.A. and 0.79 ± 0.03 for the axial ratio also compare reasonably well with those of Quirrenbach et al. (1997) who report values of $19^\circ \pm 2^\circ$ and 0.70 ± 0.02 for the same parameters. This is reasonable agreement considering that circumstellar environments of Be stars (including γ Cas) are variable at many time scales and, thus, different observations might correspond to different states of the system. Furthermore, the uncertainties of our best-fit parameters are larger than those of Quirrenbach et al. (1997), as expected, because they have twice as many observations and we solve for the extra $c_{\rm p}$ parameter.

3.7.2 Evaluation of Errors

We see in our control star that the atmospheric and instrumental degradations can be removed with a quadratic polynomial, although residuals at the $\sim$1% level can remain. These are most likely attributable to how well we can estimate the additive bias introduced in the data (recall § 2.2.2). The bias behaves like an additive error in the data, so

$$V^2_{\rm obs}(\lambda_i) = \Gamma^2(\lambda_i) V^2_{\rm src}(\lambda_i) + B(\lambda_i), \tag{3.12}$$

where $B(\lambda_i)$ can vary in magnitude from channel to channel. Although the correction for bias is applied to all observations obtained by NPOI, including those presented in this study, this cancellation is not always performed perfectly, since its magnitude is not always known with sufficient precision. For the observations presented in this study, we expect the residuals from the bias corrections, as well as the potential contamination by the metrology laser (discussed in § 3.4), to be the most significant sources of error. In the future, better statistical estimates for the detector bias, as well as isolating Hα emission line with a narrowband filter, have the potential of eliminating these sources of error.

It should be possible to assess the significance of the bias in the squared visibilities by comparing the results obtained from the triple products with those from V^2-values. This is because with our instrumental configuration, where each pair of beams falls onto a different detector, the bias term is not present in the closure quantities. For optical interferometers with three or more simultaneous baselines, the closure quantities are obtained from the real (X) and imaginary (Y) part of the complex visibility on each baseline:

$$V^{(3)}\mathrm{e}^{\mathrm{i}\Phi_{\mathrm{cl}}} = \langle (X_1 + \mathrm{i}Y_1)(X_2 + \mathrm{i}Y_2)(X_3 + \mathrm{i}Y_3) \rangle, \tag{3.13}$$

where Φ_{cl} is the closure phase and $V^{(3)}$ is the triple amplitude.

As a consistency check, we have calibrated the $V^{(3)}$-values for all observations of γ Cas using the same approach as used with V^2-values. Figure 3.9 shows the calibrated triple amplitudes already averaged over the two channels that contain the Hα emission and compares them to the predicted triple amplitudes calculated using our best-fit elliptical Gaussian models to the squared visibilities, which we have described in § 3.6. The agreement between the average triple amplitudes from the two channels (the Hα channel), and the predicted values is excellent, which indicates not only full consistency, but also that our calibration can be applied equally well to the triple amplitudes.

Another source of error is the uncertainty of the flux-weighted central wavelength of an individual spectral channel, since only average central wavelengths obtained on other targets in the past were used in our analysis. Systematic errors in the calibration of the spatial frequencies u and v, which are related to our angular scale, will affect our derived angular size of the emitting region (see also the discussion by Hajian et al. (1998) and Mozurkewich et al., 2003).

The variations in the strength of the emission line with respect to the stellar photospheric contribution from one night to another are accounted for with the c_{p} parameter. At the same time, when the best-fit value for c_{p} is obtained from a set of observations, it is assumed that the value of that constant does not change for that set. Thus, to obtain a single estimate for the value of c_{p} it is important to use observations obtained on time scales shorter than those on which there is a significant variability in the strength of the emission line.

Since all channels, including those from which scientific information is extracted, are calibrated relative to the stellar photospheric component, one might expect a slight dependence of the final results on the adopted uniform disk diameter. We have tested this dependency by calibrating the data using UD diameters ranging from an unresolved point source to a full 1 mas. In all cases we were able to reproduce our best-fit parameters for our models within 1% or better.

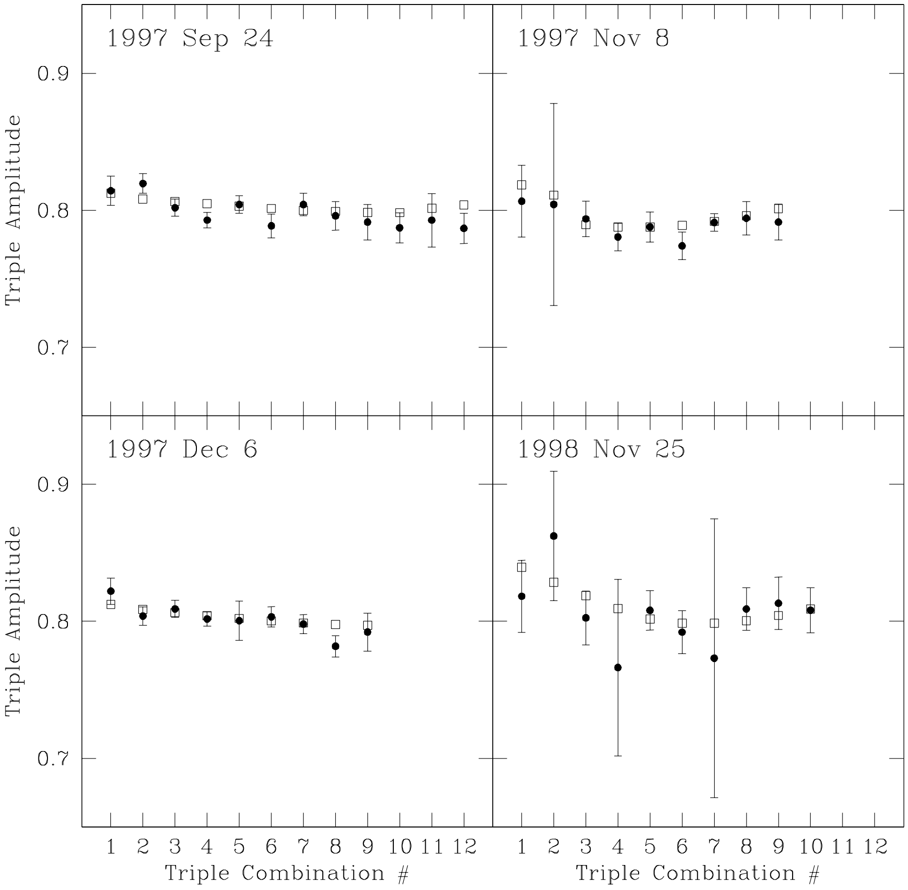

FIGURE 3.9: Triple amplitudes from the Hα channel of γ Cas for all valid triple combinations. The triple amplitudes for the elliptical Gaussian models from Table 3.3 are shown in the plot as squares.

3.7.3 Signature of Asymmetry

The closure phases we have obtained on four different nights also showed significant calibration offsets. Although a second order polynomial was not sufficient to model their variation as a function of wavelength, the variations between channels were smooth. Channels that contained the Hα emission showed a small, but unmistakable deviation from the general trend of all the other channels. Because we had only 10 spectral channels with valid closure phases, with the channels containing Hα conveniently positioned in the middle of the group, we used only eight channels (four on each side of Hα) to fit for the general trend. We have then removed the smooth trend from all 10 channels using a polynomial of third degree.

Figure 3.10 shows the weighted average of all the residual phases available for a given night, as a function of the wavelength of the spectral channels under consideration. We decided to average all closure phases for a given night at each spectral channel because the residual phases did not change significantly throughout the night. For all of our observations, the spectral channel at 665 nm shows residual closure phases systematically above the general trend, somewhere between ~2° and ~5°, depending on the night. Residual phases for the spectral channel at 648 nm show very small deviation (not detectable on one or two nights) from the general trend. This is also in agreement with the fact that this channel is the one with less Hα flux since its V^2-values lie much closer to the UD values at short baselines (recall Fig. 3.5). It is also important to note that our control star does not show any detectable residual phase deviations at any channel (see Fig. 3.11).

Since spatial flux distributions that are point-symmetric with respect to the flux-weighted center contain phases that are 0° or 180°, the closure phases (a sum of three phases) are also expected to be 0° or ±180°. This is a direct result of the fact that the Fourier components of such point-symmetric flux distributions are always real, although they can be positive or negative. Therefore, because the stellar photospheric component is not significantly resolved, it can be expected to have zero closure phases. Because the total flux in the two spectral channels with central wavelengths at 648 and 665 nm consists of a contribution from the central star as well as the circumstellar envelope, and if we assume that the envelope is point symmetric (i.e., its Fourier components are also real) then the *net* Fourier component in each channel should still be real, and we should expect to see a closure phase of 0° or ±180° in each channel. Since the observed closure phases are neither 0° nor ±180° (recall Fig. 3.10), it is thus possible that the spectral channel at 665 nm (and possibly the one at 648 nm) is detecting contributions from regions positioned asymmetrically with respect to the stellar component. We cannot say conclusively what causes these closure-phase residuals, but possible causes are: a rotational signature, or spatial asymmetry due to the circumstellar envelope being offset from the central star (see also the discussion in the next section). We should note that the observed residual closure phases are qualitatively in an agreement with the phase shifts across the Hα profile of γ Cas observed by Berio et al. (1999).

The Implications of the 5° Closure Phase

The quasi-periodic V/R variability associated with the Balmer line emission of γ Cas is well documented (Horaguchi et al., 1994) and this is the strongest evidence that the circumstellar

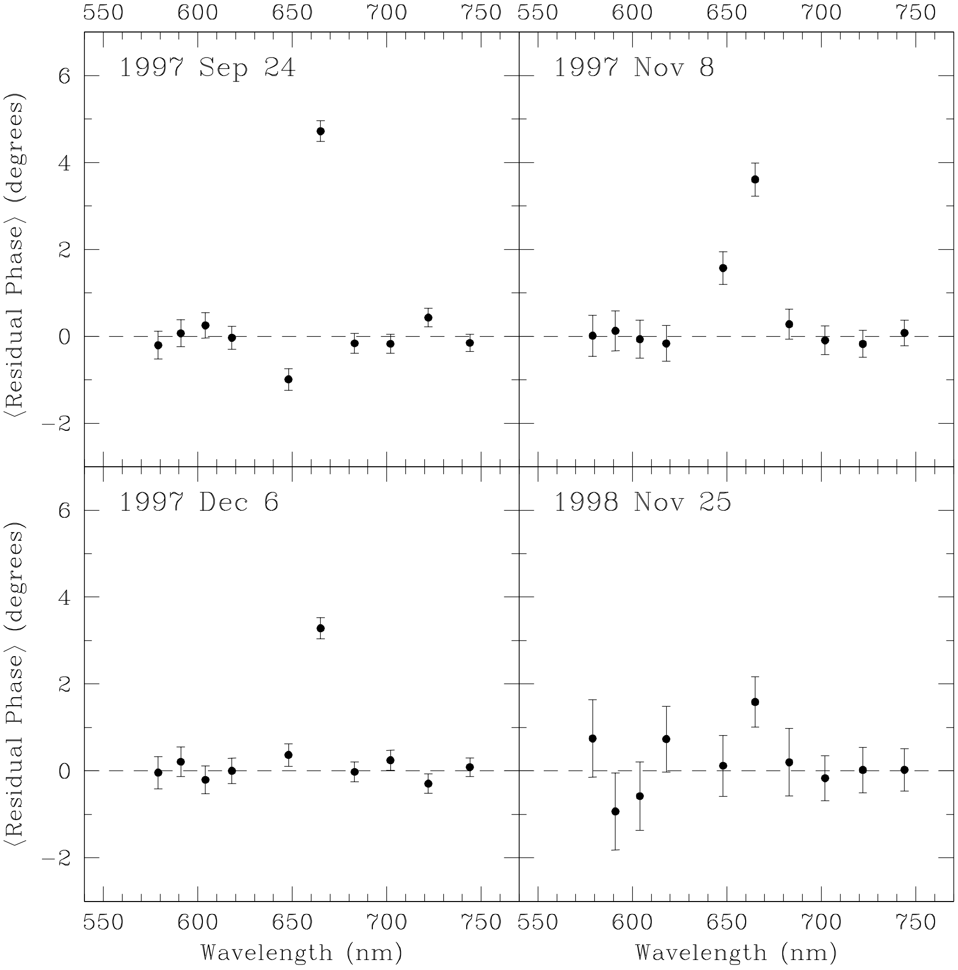

FIGURE 3.10: Weighted average of the closure phases of γ Cas for all four nights, plotted as a function of the central wavelengths of the spectral channels, after the removal of the systematic trend.

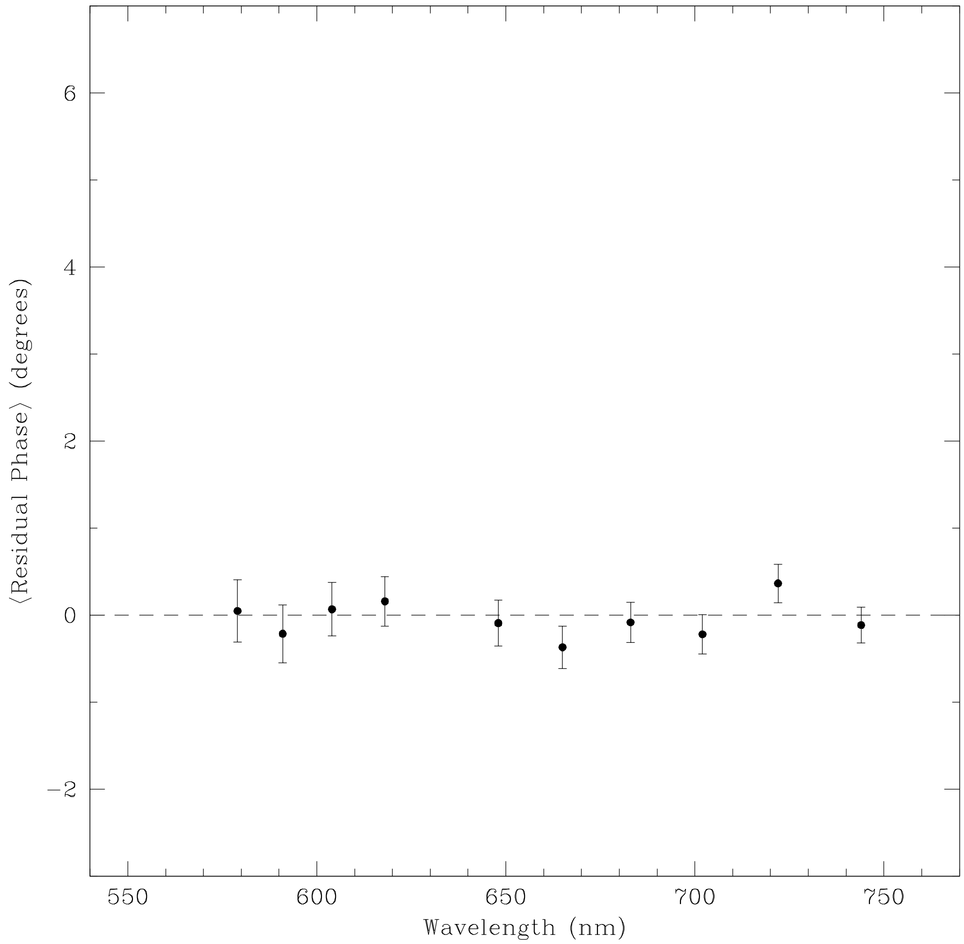

FIGURE 3.11: Same as Figure 3.10, but for the control star β Cas on 1997 September 24.

region is not symmetric with respect to the central star. Such asymmetries can be explained with models describing one-armed global oscillation (i.e., a density wave) in a geometrically thin nearly Keplerian disk (Kato, 1983; Okazaki, 1991, 1997). However, γ Cas is also a spectroscopic binary (Miroshnichenko, Bjorkman, & Krugov, 2002) as well as is an X-ray emitter (Kubo, Murakami, Ishida, & Corbet, 1998). Tidal interactions between the companion star and the circumstellar disk can also produce asymmetries (like the one proposed by Marlborough, Snow, & Slettebak, 1978). Regardless of the possible cause for asymmetry in the circumstellar envelope, we will now analyze the largest differential phase present in our data assuming it is solely due to an asymmetric structure and not, for example, due to rotational signature (recall that the Hα emission is not confined to a single spectral channel).

The most significant closure phase detected was on the night of 1997 September 24 in the 665 nm channel (recall Fig. 3.10), and therefore we will only consider the data from that night as an example of the most extreme case. Figure 3.12 shows all the closure phases from the 665 nm channel in the order in which they were obtained during that night. The variation of the differential closure phase during the night is relatively small and this is somewhat surprising considering that the position angles of the individual baselines change significantly during the night (recall Table 3.1). However, because we are dealing with closure phases, it is quite possible that as the orientations of the baseline projections on the sky change during the night the individual complex phases change, but the sum remains relatively constant. For the purpose of the discussion presented here we will assume that the closure phase, $\Phi_{\rm cl}$, is constant and has a value of approximately 5° (more accurately the weighted average is $4\overset{\circ}{.}72 \pm 0\overset{\circ}{.}24$).

The closure quantities must be defined for a closed triangle, and therefore the directions of the baseline vectors, which also affect the positions of the (u, v) points across the origin of the (u, v)-plane, are important. In our case, the closure quantities are defined for the AW0→AC0→AE0→AW0 astrometric station triangle[1] and the resulting (u, v)-plane coverage for that particular triangle is shown in Figure 3.13. Because we need only to account for three different baselines, we can express our closure phase as a sum of the form:

$$\Phi_{\rm cl} = \Phi_{\rm 18.9m} + \Phi_{\rm 22.2m} + \Phi_{\rm 37.5m}, \tag{3.14}$$

where the subscripts on the complex phases correspond to the baseline lengths.

Model fitting to both squared visibilities and closure phases is not feasible because we have

---

[1] Recall that our observations are obtained at three separate baselines, AC0–AE0 (18.9 m), AW0–AC0 (22.2 m), and AE0–AW0 (37.5 m), all shown in Figure 2.7.

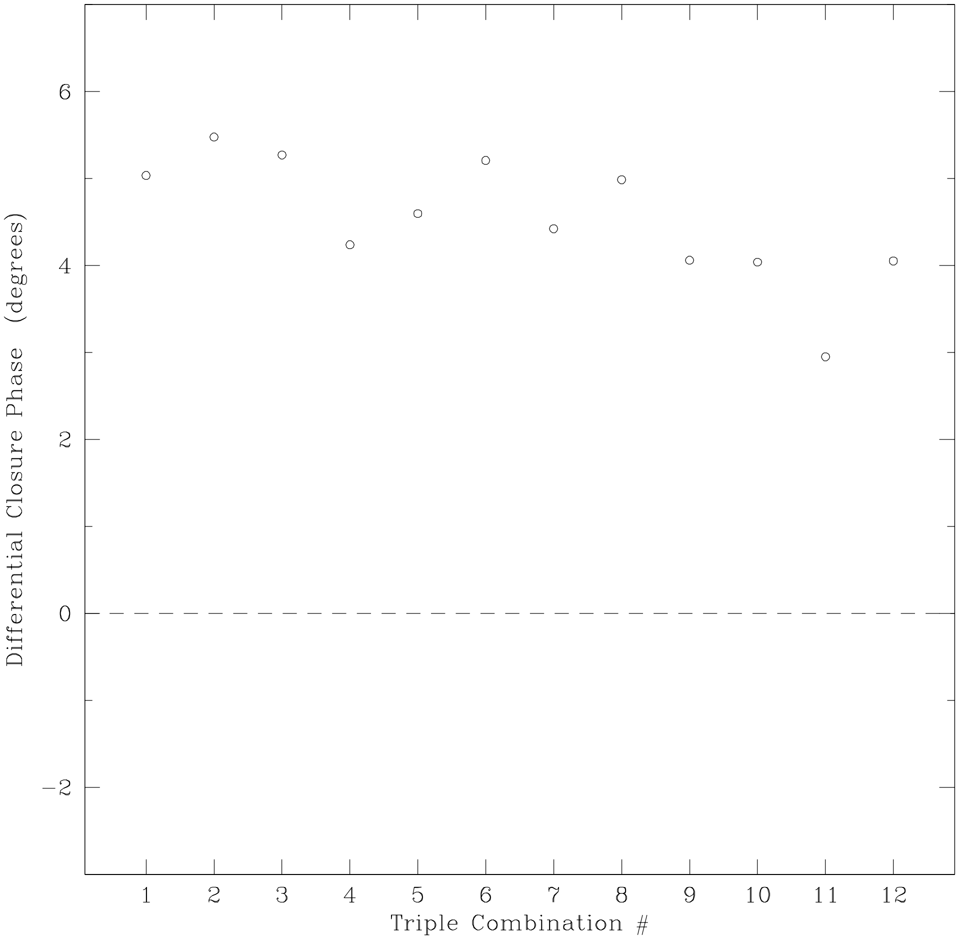

FIGURE 3.12: Differential closure phases of γ Cas from the 665 nm channel and the night of 1997 September 24 for all valid triple combinations. The numbers of triple combinations correspond to the order in which they were acquired. The uncertainties of the individual closure phases are approximately 1°.

only a small number of closure phases and the Hα emission is not confined to a single spectral channel. Nevertheless, the simplest explanation for the differential closure phase of 5° seen in the 665 nm channel is a simple offset of the circumstellar region with respect to the central star. Using the Fourier shift theorem (see, for example, Bracewell, 2000, p. 332) we can rewrite the sum of the UD and the elliptical Gaussian models we described in equation (2.28) to account for the spatial offset of the elliptical Gaussian, in which case the equation becomes

$$V_{\mathrm{UD+Gauss}} \mathrm{e}^{\mathrm{i}\Phi} = c_{\mathrm{p}} V_{\mathrm{UD}} + (1 - c_{\mathrm{p}}) V_{\mathrm{Gauss}} \mathrm{e}^{-\mathrm{i}2\pi(x_0 u + y_0 v)}. \tag{3.15}$$

The extra phase term at the end of the above equation is due to the shift of x_0 and y_0 in the east-west and north-south directions on the sky, respectively. Our goal is to deduce the value of this extra phase term, $-2\pi(x_0 u + y_0 v)$, from the complex visibility phase Φ. Before we can do this we must first estimate the complex phases from the closure phase in the 665 nm channel.

Based on the data shown in Figure 3.5 we infer that the majority of the Hα flux at the longest baseline falls onto the 648 nm spectral channel (these are the points with the highest spatial frequencies), and therefore the 37.5 m baseline does not contribute significantly to the closure phase in the 665 nm channel. Furthermore, because at spatial frequencies of $>$50 Mλ the circumstellar envelope is almost fully resolved (recall Fig. 3.6), then $V_{\mathrm{Gauss}} \approx 0$ in equation (3.15) and the complex phase Φ will not be sensitive to any spatial offsets x_0 or y_0 detected on the longest baseline. Based on the above arguments we conclude that $\Phi_{37.5\ \mathrm{m}} \approx 0$ and this implies that $\Phi_{18.9\mathrm{m}} + \Phi_{22.2\mathrm{m}} \approx 5^\circ$.

By comparing the (u, v)-plane coverage of the 18.9 and 22.2 m baselines in Figure 3.13 with the schematic representation of the best-fit elliptical Gaussian model in Figure 3.14 we see that the observations resolve the envelope along both the major- and minor-axis. Because the closure phases shown in Figure 3.12 do not appear to vary significantly as the orientations of the baselines change, this suggest that as one complex phase decreases the other increases, keeping the sum roughly constant. This could be easily explained with a small shift of the envelope along the east-west direction, since it can be seen from Figure 3.13 that the (u, v)-tracks[2] indicate that the 22.2 m baseline is in the east-west direction at the beginning of the observing run, whereas the 18.9 m baseline has the same orientation at the end of the observing sequence. Therefore, we conclude that the most likely explanation for the closure phase observed in the 665 nm is that both $\Phi_{18.9\mathrm{m}}$ and $\Phi_{22.2\mathrm{m}}$ vary between 0° and 5° (at a maximum) as the orientation of the

---

[2] Because of Earth's rotation the projection of the baseline vector on the sky changes in such a way that the (u, v)-plane coverage for a single baseline traces part of an ellipse.

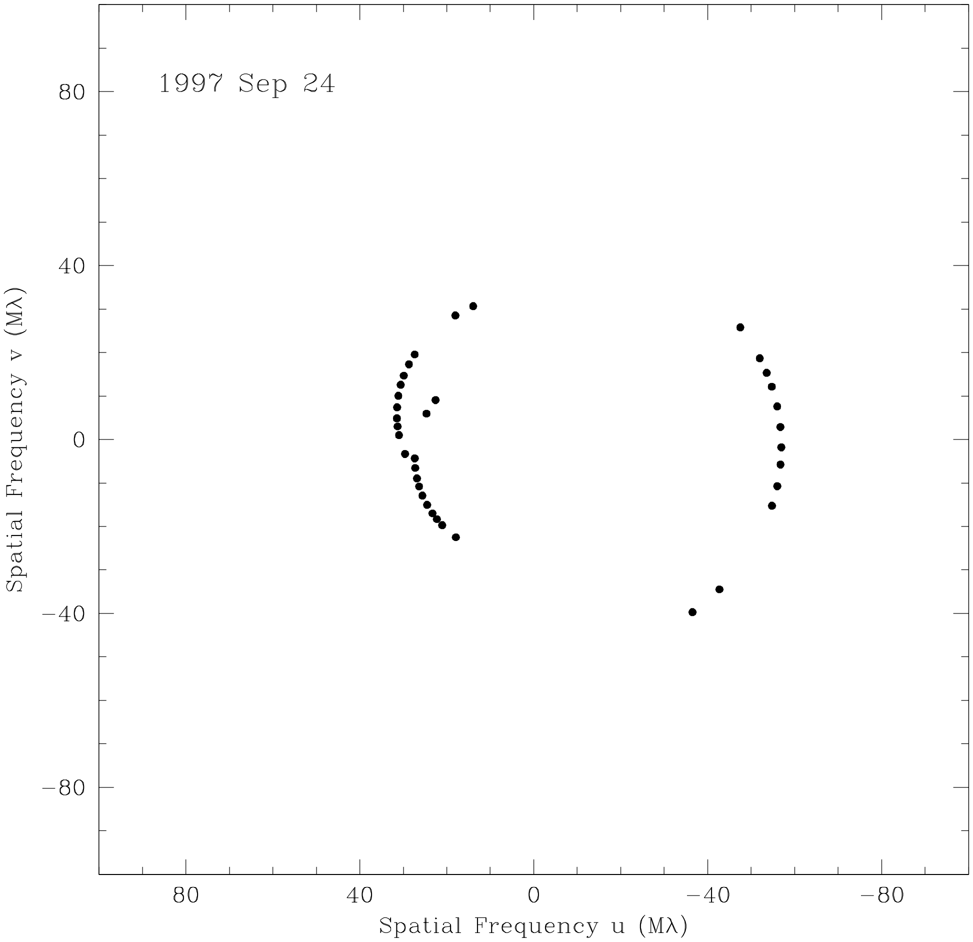

FIGURE 3.13: Same as the Fourier (u, v)-plane coverage in Fig. 3.1 for the night of 1997 September 24 except that only the u and v points are shown that correspond to the closure quantities.

baselines changes during the night. In fact, because the two baselines are not at a right angle to each other, the actual range will be even smaller (more likely between 1° and 4°).

Finally, if we assume that the spatial offset of the elliptical Gaussian is located along the east-west direction then $y_0 \sim 0$ and the extra phase term in equation (3.15) becomes $-2\pi x_0 u$. Because the imaginary components (as well as real) must be equal to each other in equation (3.15) we can use this property to obtain a relationship between the complex phase Φ and $-2\pi x_0 u$:

$$V_{\mathrm{UD+Gauss}} \sin\Phi = (1 - c_{\mathrm{p}}) V_{\mathrm{Gauss}} \sin(-2\pi x_0 u). \tag{3.16}$$

From Figure 3.6 we estimate that at the average spatial frequencies associated with the 18.9

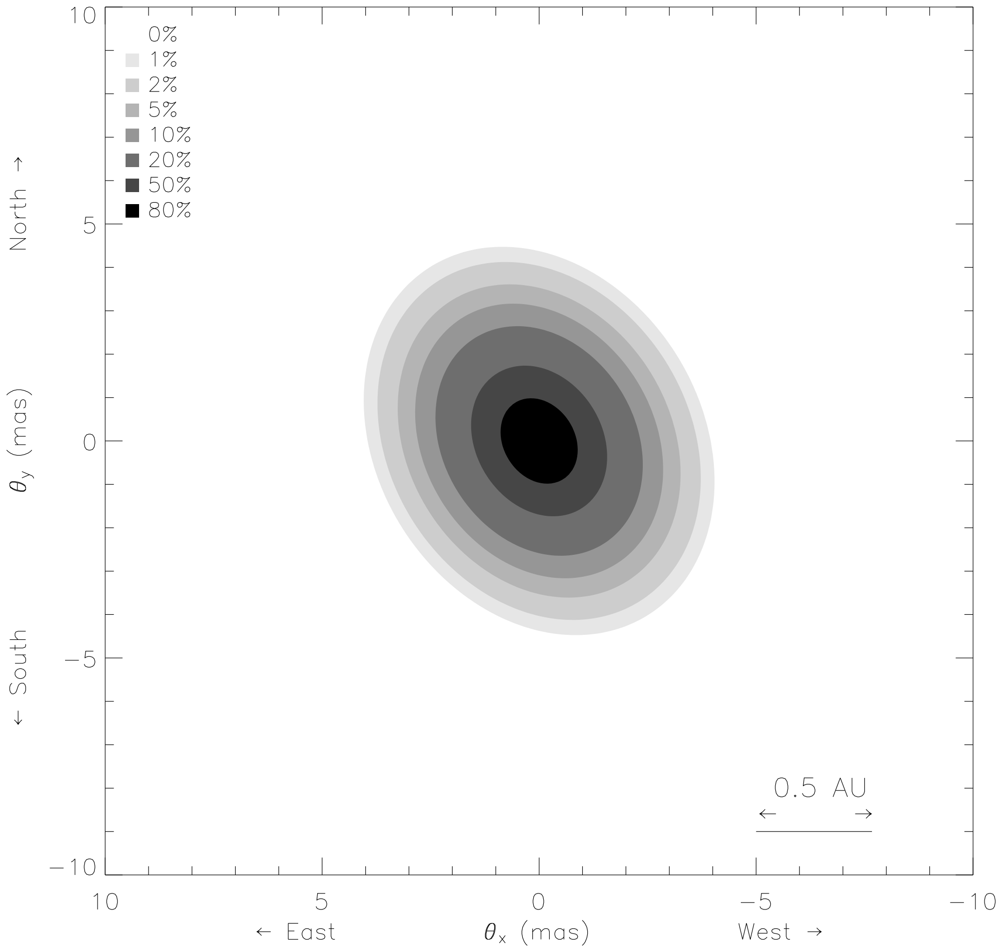

FIGURE 3.14: Schematic of the best-fit elliptical Gaussian model for γ Cas based on the ensemble average parameters of 3.67 mas for the angular size of the major axis, 0.79 for the axial ratio, and 32° for the position angle.

and 22.2 m baselines ($\sim$ 30 Mλ), the visibility amplitudes $V_{\mathrm{UD+Gauss}}$ and V_{Gauss} are $\sim$0.95 and $\sim$0.45, respectively. Furthermore, because we are assuming that most of the Hα flux falls onto the 665 nm channel $c_{\mathrm{p}} \sim 0.84$ (recall that for the averaged spectral channel $c_{\mathrm{p}} \approx 0.92$). Combining all of these values with the estimated maximum complex phase Φ of 4° we obtain a phase angle of 67° (1.17 radians) for $-2\pi x_0 u$. At $u \sim 30$ Mλ this translates to an angular offset x_0 of -6.2×10^{-9} radians or -1.28 mas. We conclude that the maximum closure phase observed in the 665 nm spectral channel can be accounted for with an elliptical Gaussian model that is offset 1.28 mas to the west of the central star. This is a significant offset considering that $\theta_{\mathrm{mj}} = 3.67 \pm 0.09$ mas, and therefore the offset is approximately one third of the width of the Gaussian. It is also interesting to note that equation (3.16) has no solutions for $\Phi > 4\overset{\circ}{.}35$, which is consistent with our estimate that the individual phases are most likely between 1° and 4°, even though $\Phi_{\mathrm{cl}} \sim 5°$.

3.8 Summary

We have demonstrated the effectiveness of a technique where both the calibration and source characteristics are obtained from the same data. The technique works especially well for modeling line-emitting regions that differ in spatial character from continuum sources that are unresolved or only slightly resolved. The method requires the emission feature to be of sufficient strength so that the signal due to the line-emitting region is not lost in the noise of the continuum radiation from the stellar photosphere. It is anticipated that the use of the custom narrowband filter, now used by NPOI in Hα observations (Pauls et al., 2001), will substantially reduce the uncertainty due to this source of error. Isolating Hα and aligning the filter such that all the light in the emission line falls at the center of one channel will also enable a much stronger treatment.

We have applied our technique to a limited set of observations of γ Cas and obtained a clear signature of a resolved Hα-emitting region. The best-fit elliptical Gaussian model fitted to our observations has an average angular size of the major axis of 3.67 ± 0.09 mas, an average axial ratio of 0.79 ± 0.03, and an average P.A. of 32° ± 5°. Simultaneous monitoring of Hα emission during the interferometric observations would also be very valuable, to ensure that there is no significant variability during a single observation and possibly to constrain the actual value of the fractional contribution from the stellar photosphere in the observed spectral band.

Since the technique presented in this study can be applied equally well not only to squared visibilities but also to triple amplitudes and closure phases, it should also be possible to obtain synthesized images from a large enough set of such narrowband observations. Since synthesis imaging requires a large amount of data and we obtain only three V^2-values and one closure phase simultaneously from a three-beam combination, it would not be feasible to obtain an image from our limited sample presented in this study. On the other hand, with the advent of six-beam combination at NPOI, optimum array configurations for a given source can be obtained. With this new capability, 10 closure phases and 15 baselines resulting in 15 V^2-values are obtainable. Concatenation of data acquired on successive nights with different array configurations can further optimize results by significantly improving the (u, v)-plane coverage, thereby enabling image synthesis (see also the discussion by Gilbreath et al., 2003).

Chapter 4

The Circumstellar Envelope of ζ Tauri*

4.1 Introduction

The Be star ζ Tauri (=HR 1910) is one of the brightest stars of its type. This makes the star a very attractive target for current optical interferometers. In fact, the circumstellar envelope of ζ Tau, with a strong Hα emission, has been observed by several such instruments, including the Mark III (Quirrenbach et al., 1994, 1997), and GI2T (Vakili et al., 1998). This chapter reports observations by the Navy Prototype Optical Interferometer (NPOI).

The Hα emission line of ζ Tau is typically observed to have an irregular shape, but because it usually shows a double-peaked structure it can be classified as having asymmetric double-peaked profile (see, for example, the Hα profile in Banerjee et al., 2000). Over the years characteristic variations in the shape and the strength of the Hα emission line have been observed. Although the detailed behavior of the line profile can be quite complex, the most common spectroscopic quantity used to characterize this type of variability is the ratio of the violet to red components (V/R). In the case of ζ Tau this V/R ratio varies cyclically on time scales of a few years (Guo et al., 1995). Most recently, this type of variation has been explained with models having one-armed oscillation in a nearly Keplerian disk, such as the ones constructed by Kato (1983) and Okazaki (1991, 1997), but other models have been also proposed (see the models listed in Guo et al., 1995, and references therein).

Although the first interferometric studies related to the variability of Be stars suggest that one-armed oscillations have been detected in the circumstellar disks of ζ Tau (Vakili et al.,

---

*The material from this chapter has been published in the *Astronomical Journal*, vol. 127, pp. 1194–1203.

1998) and γ Cas (Berio et al., 1999), these first investigations do not have enough observations to model fully the spatial extent of the circumstellar material. In fact, they rely on previously determined model parameters, such as the position angle (P.A.) or the axial ratio of the line-emitting region, taken from studies based on observations from different epochs.

In this study we model the circumstellar envelope of ζ Tau as an elliptical Gaussian and compare our results to the measurements reported by Quirrenbach et al. (1997) for observations obtained from late 1991 to late 1992. We specifically concentrate on model parameters, such as the axial ratio, P.A., and angular size of the major axis that describe the orientation and the size of the circumstellar envelope of ζ Tau. We also search for any differences that might be related to the observed changes in the shape and the overall strength of the Hα emission from different epochs. Since ζ Tau is also a single-lined spectroscopic binary, we also look at how our derived size of the circumstellar envelope compares with the published binary parameters.

4.2 Observations

The observations of ζ Tau were obtained on 1999 March 1 and consist of eight individual scans collected over a period of about 4.5 hr. Each scan corresponds to 90 s of integration during which the fringe parameters, the squared visibilities (V^2), are measured simultaneously at three baselines and 11 spectral channels covering the region between 573 and 808 nm. The instrumental configuration of NPOI is described in detail by Armstrong et al. (1998), and the initial data reduction involved in obtaining the V^2-values from the photon counts, for the case of a three-beam combination, is discussed by Benson et al. (1997) and Hummel et al. (1998). In addition to the observations of the target star, we have followed each scan of ζ Tau with an equivalent scan on a "check" star (for a total of eight reference scans). The check star was η Aur (=HR 1641), which is a B3 V standard star (Garcia, 1989) with no Hα emission.

The circumstellar envelope of a typical Be star can emit radiation not only in the Balmer series, but also in other spectral lines, as well as at the continuum wavelengths due to the hydrogen free-free and bound-free emission (Doazan, 1982). However, two weeks after our interferometric observations, the Hα emission line of ζ Tau was observed to have an equivalent width (EW) of -2.064 nm, with a peak emission more than 3 times the continuum level (Banerjee et al., 2000). Therefore, in our spectral region of interest, 573–808 nm, we concentrate on the spectral channel that contains the overwhelmingly dominant Hα emission (see also the dis-

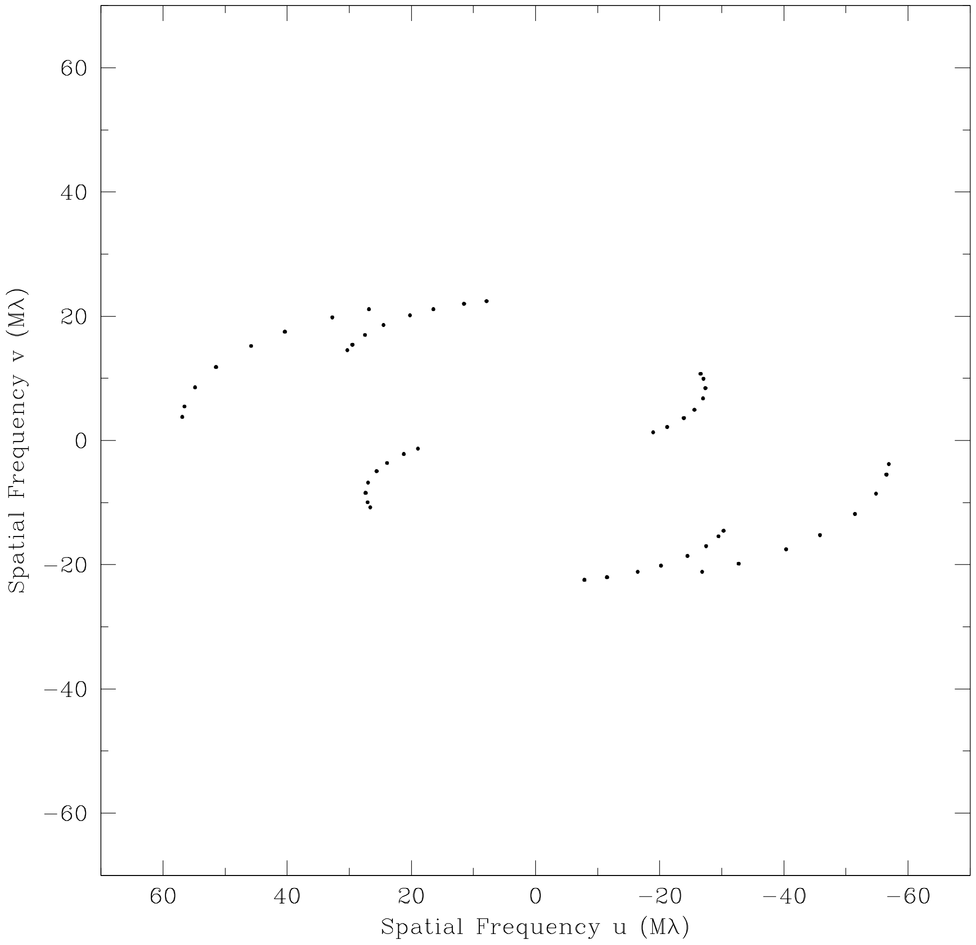

FIGURE 4.1: The Fourier (u, v)-plane coverage at Hα for observations of ζ Tau obtained from three simultaneous baselines in eight scans on 1999 March 1. The baselines have lengths of 18.9 m, 22.2 m, and 37.5 m with azimuths of $-67.^\circ5$, $63.^\circ6$, and $86.^\circ0$, respectively.

cussion in § 3.5). Figure 4.1 shows the Fourier (u, v)-plane coverage corresponding to the Hα emission for all scans used in this analysis. A distinctive pattern can be seen in the plot that is caused by the changing projection of the baseline vector on the sky (due to Earth's rotation) during the 4.5 hr the eight scans are collected.

For the observations presented in this chapter, the alignment of the spectral channels was such that the Hα emission fell primarily within a single spectral channel. However, depending on the baseline used, it was either the spectral channel with a *central* wavelength[1] at 648 or 665 nm. This happened because, for each baseline, the interference fringes produced at

---

[1] The central wavelengths are approximate and are used primarily as labels for the individual spectral channels.

the beam combiner were dispersed onto a separate lenslet array, each with slightly different spectral alignment (see also the discussion in § 4.3). The nine remaining spectral channels, both at shorter (four) and longer (five) wavelengths, contain mostly continuum radiation from the star, and thus we will refer to them as the continuum channels.

4.3 Calibration

The observed V^2-values that we obtained after the initial reductions are not calibrated with respect to an external calibrator, and therefore are degraded by many atmospheric and instrumental effects. Because the observations are obtained simultaneously over all spectral channels, we can now use the continuum channels to calibrate the V^2-values in the channels with the Hα contribution, which can then be used to model the circumstellar distribution of Hα emission.

The entire calibration procedure is discussed in detail in Chapter 3, and we highlight only the major steps here. First, for a specific baseline and scan the observed squared visibilities in the nine continuum channels are expressed as

$$V^2_{\mathrm{obs},i} = \Gamma^2(s_i) V^2_{\mathrm{p}}(s_i), \tag{4.1}$$

where Γ^2 is a quadratic polynomial representing the atmospheric and instrumental degradations, V_{p} is the visibility due to the stellar photosphere, and s_i is the spatial frequency in the radial direction from the origin of the (u, v)-plane for the ith spectral channel. We assume that the visibility due to the stellar photosphere is known or can be predicted based on the estimated angular size of the stellar component. We also assume that the contribution from the circumstellar envelope at the continuum wavelengths has a negligible effect on the observed V^2-values.

The stellar photosphere of ζ Tau is nearly unresolved with our baselines, and therefore it is sufficient to model it with a simple uniform-disk (UD) component for which the visibilities are given by

$$V_{\mathrm{p}} = V_{\mathrm{UD}} \equiv 2\frac{J_1(\pi\theta_{\mathrm{UD}}s)}{(\pi\theta_{\mathrm{UD}}s)}, \tag{4.2}$$

where J_1 is a first-order Bessel function and θ_{UD} is the angular diameter of the UD, which for ζ Tau is estimated to be 0.39 mas based on a photometric relation (see § 3.4 of Quirrenbach et al., 1997, and references therein). Therefore, when V^2_{p} is known, the coefficients of the quadratic function, Γ^2, can be obtained from the continuum channels using equation (4.1), and then the

V^2-values from the 648 and 665 nm channels can be calibrated according to $V_{\rm cal}^2 = V_{\rm obs}^2/\Gamma^2$. In order to analyze all three baselines in the same way, neither the 648 nor the 665 nm channel was used to obtain the quadratic forms of Γ^2 for all scans, even though only one of these channels contains the contribution from the Hα emission line at a given baseline.

Figure 4.2*a* demonstrates how effectively a quadratic polynomial (*dashed line*) describes the general trend seen in the continuum channels (*filled circles*) for one of the scans at the 37.5 m baseline. This apparent trend is mostly due to the atmospheric and instrumental degradations, but it also includes a slight contribution from the UD component. The predicted V^2-values for the UD component are shown as a solid line in Figure 4.2*b*, and, as expected, $V_{\rm cal}^2$ from the continuum channels resemble the UD model.

We can test how well a quadratic function fitted to the continuum channels describes the atmospheric and instrumental effects, by completely dividing the general trend (that represents $\Gamma^2 V_{\rm UD}^2$) out of the data. The normalized V^2-values should cluster around unity within their uncertainties, if in fact the quadratic description is satisfactory. Figure 4.3 shows the residuals as a function of the central wavelengths of the spectral channels used for all normalized observations at all three baselines. When normalized by the observational uncertainties, the majority of the residuals do fall, as expected, within a band of $\pm 1\sigma$, indicated in the plot with the dotted lines. The only spectral channels that show significant deviations from the general trend are the ones with the contribution from the Hα emission, the 665 nm channel for the two shortest baselines, and the 648 nm channel for the longest.

Figure 4.4 shows the normalized residuals for the check star η Aur (which is also nearly unresolved), and as expected, no large offsets are present in the 648 and 665 nm channels. At the same time, small systematic offsets (at the level of our slightly overestimated observational uncertainties) are visible in some spectral channels. These systematic offsets, which are spectral channel and baseline dependent, also appear to have the same general characteristics for both of our stars, and thus one might try to divide them out from our observations of the science target. However, we explain these systematic deviations as a limitation of how well we can correct for the additive bias present in each squared visibility determination. Based on our experience, the additive bias can depend on the amplitude of the squared visibility, and therefore, we decided not to divide these systematic offsets out of our Hα data (see also the discussion in § 4.4.3).

Because the V^2-values due to the UD component are nearly the same for the two spectral channels at 648 and 665 nm, and because the channels have nearly the same width, we can

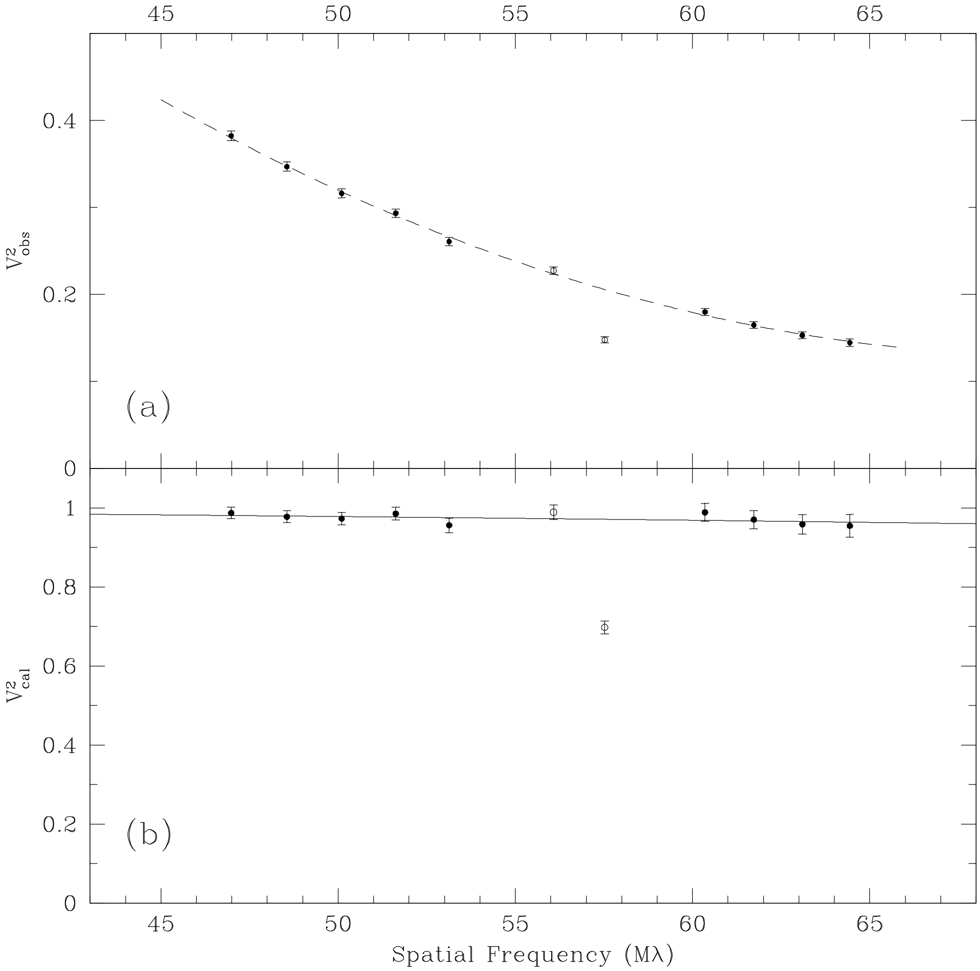

FIGURE 4.2: (*a*) Squared visibilities of ζ Tau obtained from 11 spectral channels of the 37.5 m baseline, with significant atmospheric and instrumental degradations still present. The measurements obtained from the spectral channels at 648 and 665 nm are marked with open symbols and were not used in modeling the general trend (which represents $\Gamma^2 V^2_{\rm UD}$) with a quadratic polynomial, which is shown as dashed line. (*b*) Same data as in (*a*) but after the correction by the Γ^2 factor. The predicted squared visibilities for the uniform stellar photospheric disk are shown as a solid line.

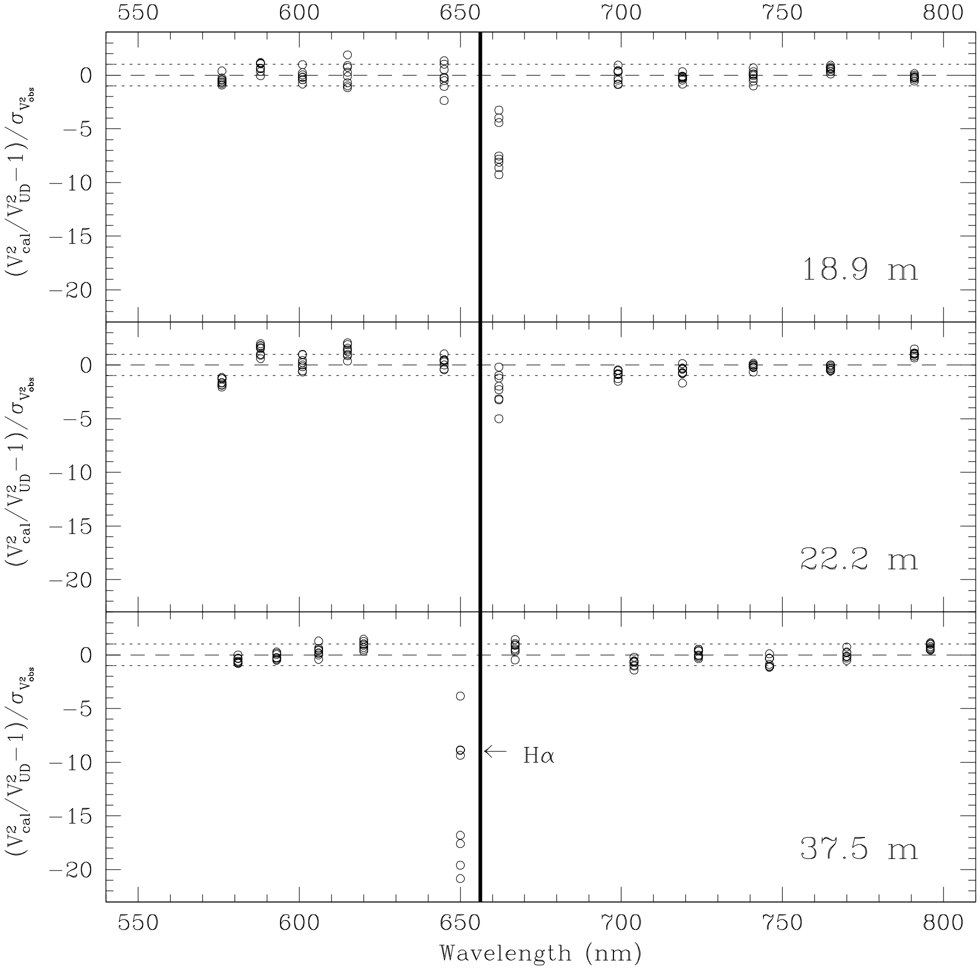

FIGURE 4.3: Normalized residuals of ζ Tau left after the general trend present at each scan and baseline has been divided out, plotted as a function of the *central* wavelengths of the spectral channels and with the $\pm 1\sigma$ deviation (*dotted lines*). Each panel represents one baseline and is labeled with the physical distance between the elements that define the baseline. The position of the Hα emission at 656.3 nm is indicated with a thick vertical line.

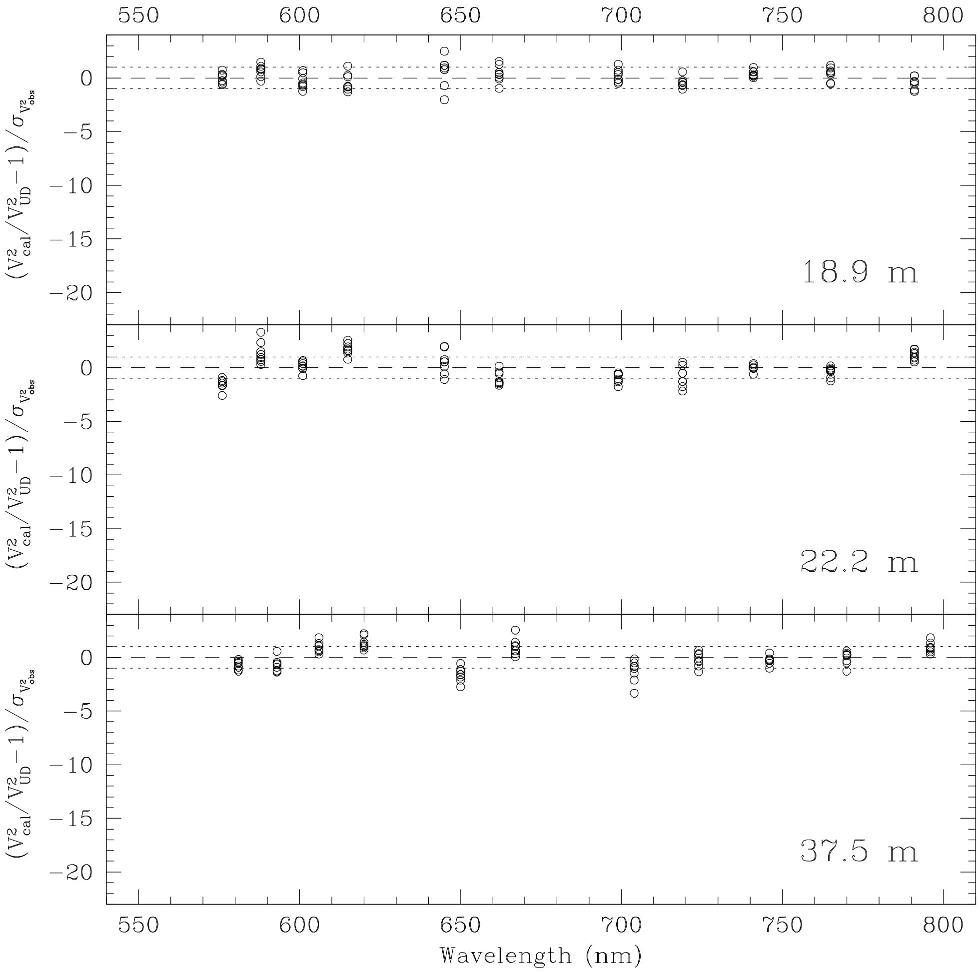

FIGURE 4.4: Same as Fig. 4.3, but for the check star η Aur.

combine the observations from both to form a single data set. More specifically, we combine the observations of ζ Tau from the 665 nm channel for the two shortest baselines with those from the 648 nm channel at the longest baseline, to produce a single dataset of V^2-values with spatial frequencies corresponding to the Hα line (i.e., we adopt a wavelength of 656.3 nm). Figure 4.5 shows the calibrated squared visibilities ($V^2_{\mathrm{H}\alpha}$) with the contribution from the Hα emission for all three baselines and eight scans (for a total of 24 independent data points), which can now be used in model fitting.

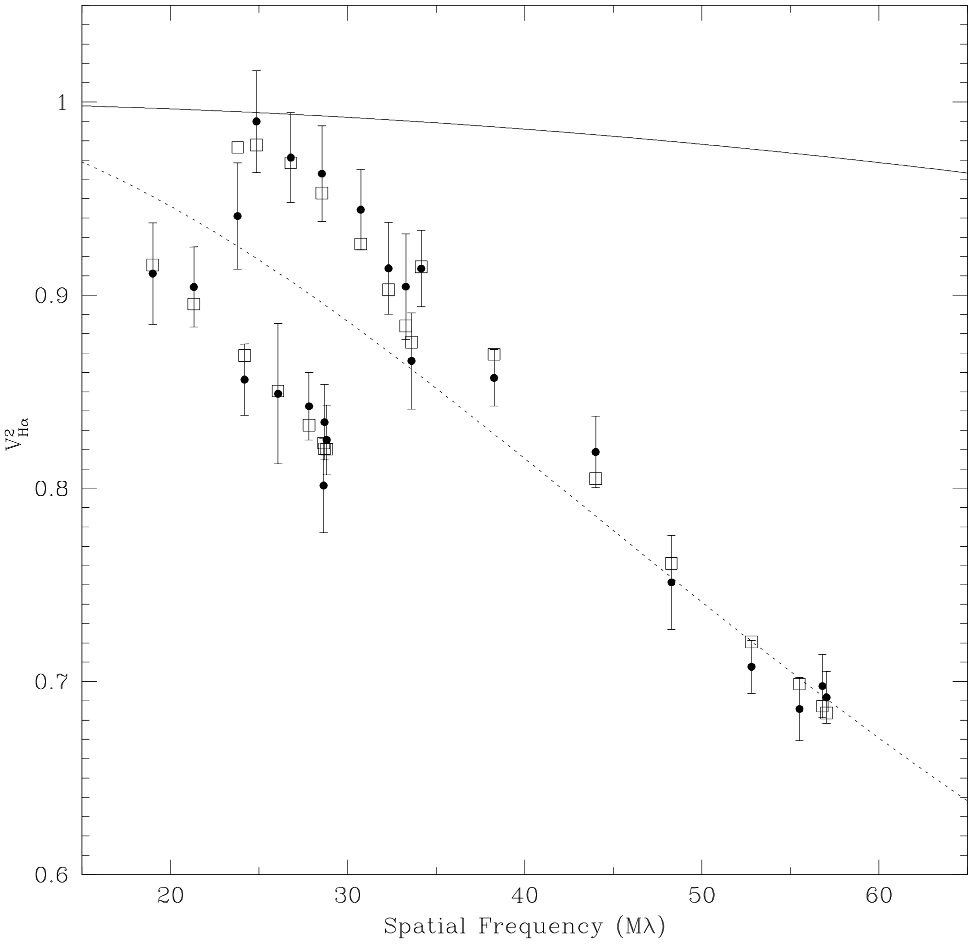

FIGURE 4.5: Calibrated squared visibilities of ζ Tau from the spectral channels with the Hα emission for all three baselines and eight scans. Shown are the uniform disk model representing the stellar photospheric disk (*solid line*), the best-fit circularly symmetric Gaussian model (*dotted line*), and the best-fit elliptical Gaussian model (*squares*).

4.4 Modeling the Hα-Emitting Envelope

4.4.1 Best-Fit Parameters

The spectral channels at 648 and 665 nm have widths of about 16 nm each, and thus are approximately 7 times wider than the Hα emission line (Banerjee et al., 2000). As a result, we must consider the contribution from the continuum-emitting stellar photosphere as well as the line-emitting circumstellar envelope. We treat this as a linear superposition of the two components, and we model the calibrated V^2 values shown in Figure 4.5 as

$$V^2_{\rm model} = \left[c_{\rm p} V_{\rm p} + (1 - c_{\rm p}) V_{\rm env}\right]^2 , \tag{4.3}$$

where $V_{\rm p}$ and $V_{\rm env}$ are the visibilities due to the stellar photosphere and the circumstellar envelope, respectively, and $c_{\rm p}$ is a free parameter that represents the fractional contribution to the total flux of the spectral channel due to the stellar photosphere.

We model the stellar photospheric component in exactly the same way as we did for the continuum channels, with a UD that has an angular diameter of 0.39 mas (recall eq. [4.2]). To model the circumstellar envelope we use an elliptical Gaussian brightness distribution centered on the star. This is the simplest model that resembles the power-law density distribution falloff usually assumed for the circumstellar disks (such as the one introduced by Waters, 1986) and is also the same model used by Quirrenbach et al. (1997). It has been shown in § 2.3 that the complex visibility for an elliptical Gaussian model is a real quantity and for a model with an axial ratio r and angular size of the major axis $\theta_{\rm mj}$ has the form:

$$V_{\rm env}(u_{x'}, v_{y'}) = \exp\left[-\pi^2 \theta^2_{\rm mj} (r^2 u^2_{x'} + v^2_{y'})/4 \ln 2\right] , \tag{4.4}$$

where $u_{x'} = u \cos\phi - v \sin\phi$ and $v_{y'} = u \sin\phi + v \cos\phi$, with ϕ representing the position angle of the major axis (which by convention is measured east from north).

Using a nonlinear least-squares fit, based on the Levenberg-Marquardt method (Press et al., 1992), we obtained the best-fit elliptical Gaussian model to the data shown in Figure 4.5 with a best-fit parameter set $\boldsymbol{P}_{\rm best} \equiv (\theta_{\rm mj}, r, \phi, c_{\rm p})_{\rm best} = (3.14 \text{ mas}, 0.310, -62^\circ\!.3, 0.814)$ and a χ^2_ν (per degree of freedom) of 0.5. The uncertainties for these parameters are given in the next section along with the discussion on how they were obtained using a Monte Carlo simulation of synthetic data sets. We also note that the best-fit model parameters are influenced only slightly by the adopted angular diameter of the UD. This is because the same model ($V_{\rm p}$) is used in the calibration of the values of $V^2_{\mathrm{H}\alpha}$ (when the Γ^2 factor is obtained via eq. [4.1]) and in the modeling of the Hα-emitting envelope (using eq. [4.3]). We have tested this numerically and found that a 100% change in the assumed UD angular diameter produces changes in the best-fit parameters of $< 1\%$.

The elliptical Gaussian model produced a much better fit to the data than a two-parameter circularly symmetric Gaussian model, which resulted with an angular size of 1.62 mas and c_{p} of 0.69, but with χ^2_ν of 5.7. Figure 4.5 shows both the symmetric and the elliptical Gaussian models, along with the observed V^2-values for the Hα emission. It is evident from the figure that the symmetric model does not match the data. It is also apparent that the observational uncertainties are slightly overestimated, which is also suggested by $\chi^2_\nu < 1$.

We conclude that the elliptical Gaussian model is a significantly better match to our data than is the circular Gaussian model. The schematic representation of our best-fit elliptical Gaussian model, as it would appear on the sky, is shown in Figure 4.6. The polarization vector at 32° (McDavid, 1999), obtained from broadband measurements at the continuum wavelengths where the circumstellar envelope is optically thin, is also shown in the figure by a dashed line. Our best-fit P.A. of the major axis is at right-angle to the polarization vector, as expected for the case of electron scattering (at the continuum wavelengths) in an axisymmetric and optically thin disk (Brown & McLean, 1977).

4.4.2 Estimating the Uncertainties

We used the Monte Carlo simulation of synthetic data sets (Press et al., 1992) to obtain the estimates for the uncertainties of the best-fit model parameters. We started with our original data set and obtained our best-fit parameters for the elliptical Gaussian model, $\boldsymbol{P}_{\mathrm{best}}$, by minimizing χ^2, as we have done in § 4.4.1. We then used these parameters to create 23,000 synthetic data sets, all with the same number of data points as our original observations. The synthetic squared visibilities were constructed by drawing numbers randomly from normal distributions, with individual widths set by the observational uncertainties of the original data points and the mean values set by the best-fit model to the original observations. We applied the same χ^2 minimization scheme to all synthetic data sets and obtained 23,000 synthetic best-fit values for each parameter. This gave us enough simulated parameters that the four-dimensional probability distribution was sampled sufficiently well, and we were able to measure the different projected widths of the distribution with high enough precision.

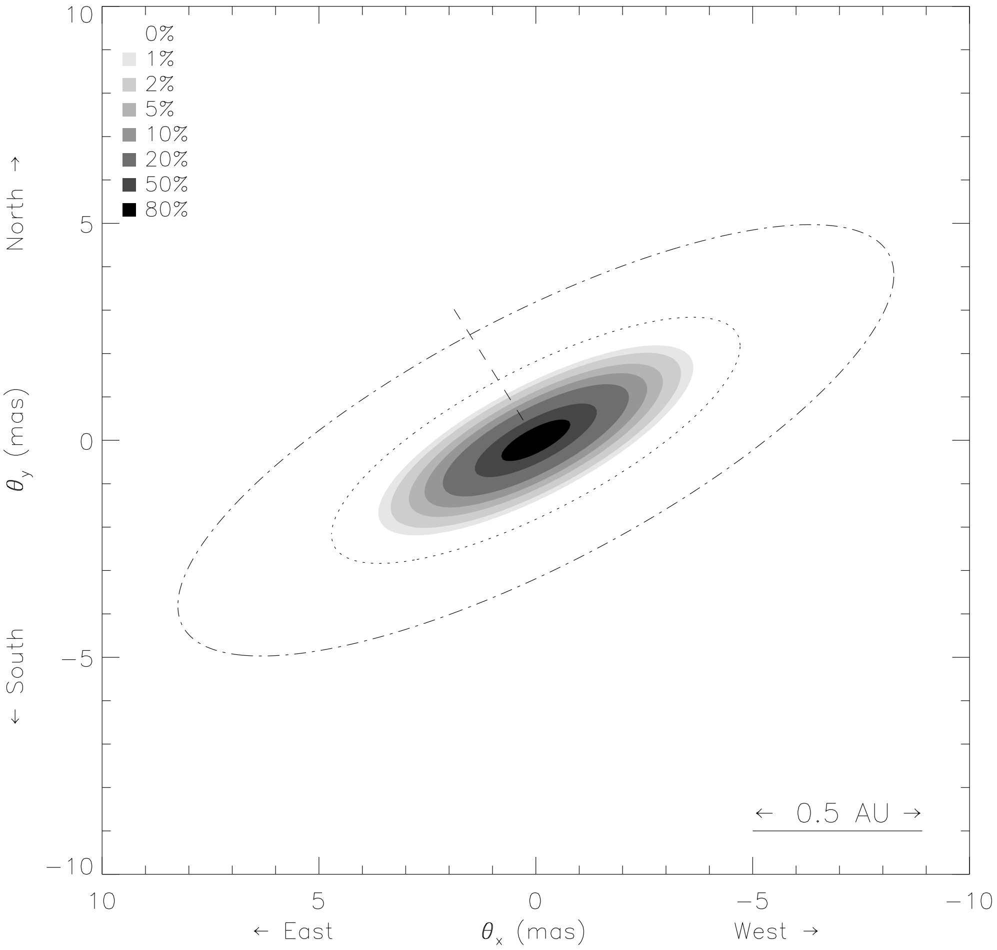

FIGURE 4.6: Schematic of the best-fit elliptical Gaussian model for ζ Tau. The *dashed line* indicates the polarization vector at 32° reported by McDavid (1999). The Roche radius of the primary star (in the plane of the disk; *dotted line*) and the projected circular orbit of the secondary component (*dash-dotted line*) are both based on the orbital parameters of Jarad (1987). The orbit neglects the small eccentricity and assumes the same orientation of the orbital plane as the circumstellar disk (see § 4.5.2 for more details).

It is not possible to plot the four-dimensional distribution of all the solutions and thus Figure 4.7 shows the marginalized distributions in six different two-dimensional planes. The majority of the solutions fall in a localized region of the parameter space, with the highest concentration of solutions near the region defined by $\boldsymbol{P}_{\mathrm{best}}$. The density contours shown in Figure 4.7 are directly proportional to the probability density functions, and therefore they provide us not only with information about the widths of the distributions, but also about the degree of correlation present between the individual pairs of parameters. We can also conclude that most of the pairs are not correlated, with exceptions in the distributions for c_{p} versus θ_{mj} (Fig. 4.7*a*) and r versus P.A. (Fig. 4.7*c*), where in both cases there is a detectable correlation.

For the case in which the parameters are statistically independent (or when the correlations between parameters are ignored), the two-dimensional density contours shown in Figure 4.7 can be collapsed further, by allowing only one parameter to vary at a time. This is shown in Figure 4.8 which displays the individual probability distributions for all four model parameters. Because all four histograms resemble normal distributions, we can fit a Gaussian curve to each distribution and obtain a corresponding standard deviation (σ) for each distribution. Based on these uncertainties our best-fit elliptical Gaussian model has $\theta_{\mathrm{mj}} = 3.14 \pm 0.21$ mas, $\phi = -62\overset{\circ}{.}3 \pm 4\overset{\circ}{.}4$, and $r = 0.310 \pm 0.072$. We also note that the best-fit fractional contribution c_{p} of 0.814 ± 0.012 compares well with our expected value of 0.84 ± 0.01, which we estimated using the EW of the *net* Hα emission (following the same procedure as in § 3.6) and by approximating the stellar photospheric contribution with the NPOI channel bandwidth (i.e., by adopting a stellar contribution of 16 ± 0.5 nm).

4.4.3 The Additive Bias

The data we have presented in this study might be limited by the presence of an additive bias that introduces systematic offsets, and not by the intrinsic scatter of the individual data points. The channel-to-channel variations in our calibrated data are at the ~1% level and appear to be baseline dependent (recall Fig. 4.3). This means that even if our data from the spectral channels with the Hα emission are affected by the additive bias, it is unlikely that all three baselines are affected in exactly the same way. Nevertheless, to assess the significance of such a potential systematic offset on our results, we have simulated its effect on our data.

We have simulated two different cases where *all* V^2-values used in the original model

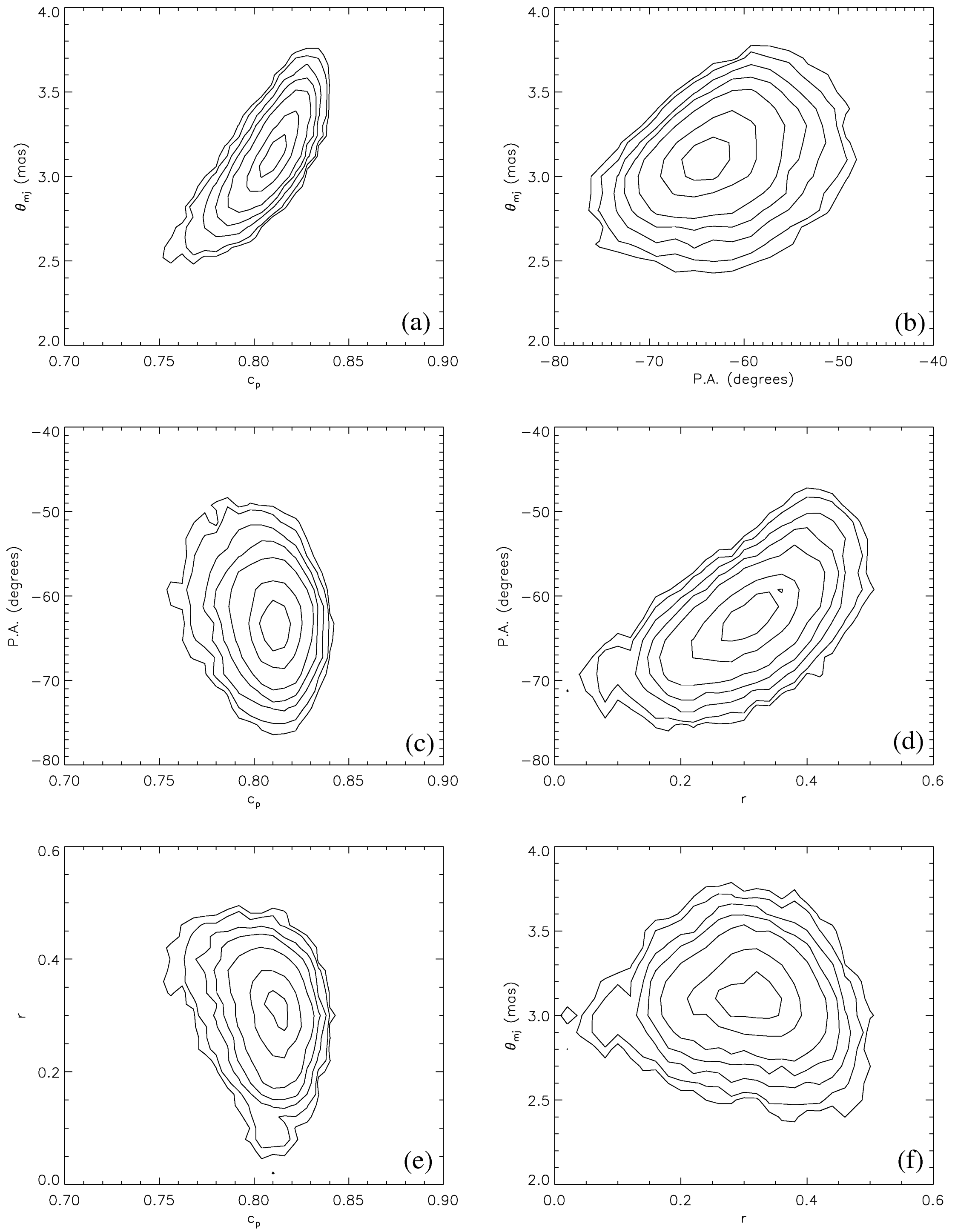

FIGURE 4.7: Density contour plots of the 23,000 synthetic best-fit values obtained for each of the four parameters describing the elliptical Gaussian model of ζ Tau. Each panel shows a two-dimensional view of the four-dimensional parameter space. The contour levels are at 1%, 2%, 5%, 10%, 20%, 50%, and 80% of the peak density.

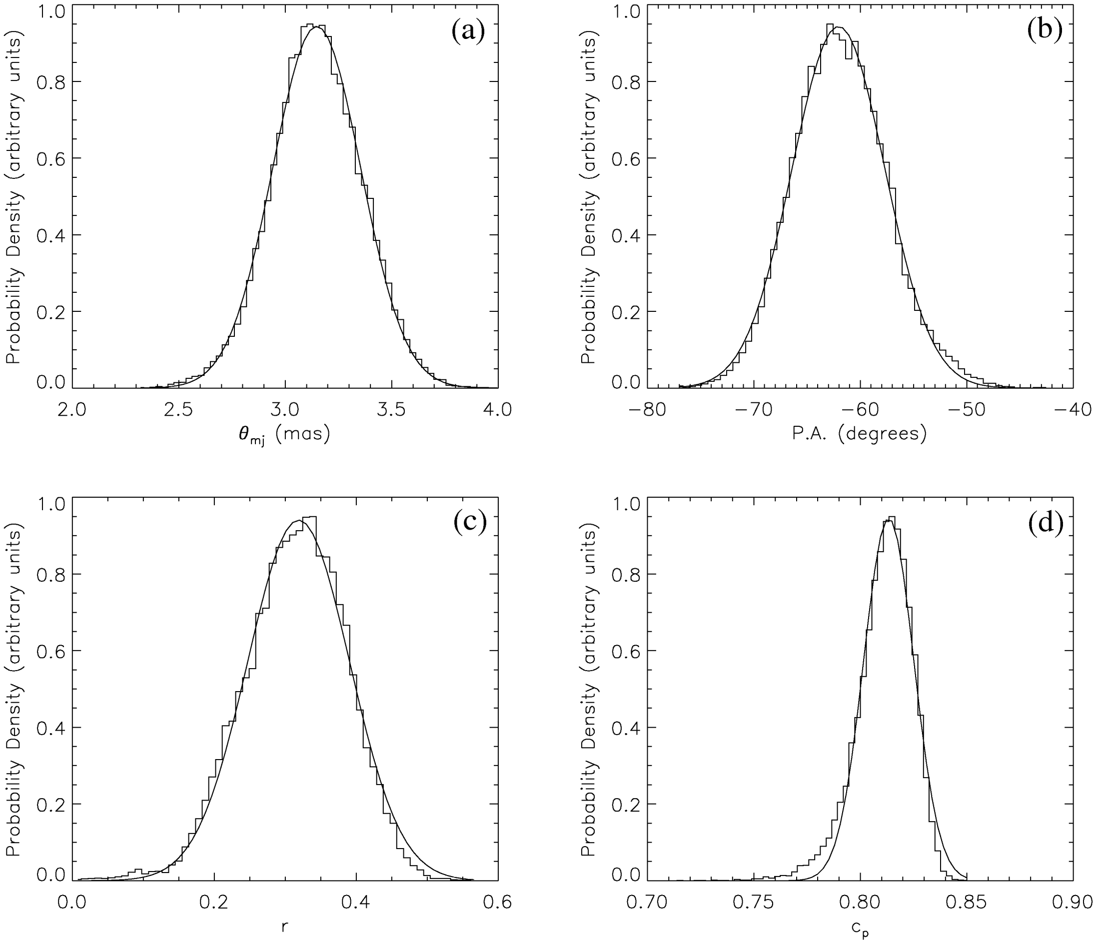

FIGURE 4.8: Histograms of all solutions for ζ Tau parameters plotted as a function of only one independent variable. Each panel corresponds to 23,000 best-fit values obtained from the simulated data sets. Solid lines represent the Gaussian fits to the individual distributions.

Table 4.1: Best-Fit Model Parameters at Different Levels of Simulated Additive Bias

Type of Data	$\theta_{\rm mj}$ (mas)	r	ϕ (deg)	$c_{\rm p}$	χ^2_ν
$V^2_{\rm H\alpha} + 0.01$	3.01 ± 0.24	0.211 ± 0.120	-64.5 ± 4.3	0.817 ± 0.015	0.5
$V^2_{\rm H\alpha}$	3.14 ± 0.21	0.310 ± 0.072	-62.3 ± 4.4	0.814 ± 0.012	0.5
$V^2_{\rm H\alpha} - 0.01$	3.26 ± 0.23	0.371 ± 0.078	-60.3 ± 5.2	0.810 ± 0.012	0.5

fitting ($V^2_{\rm H\alpha}$) were either decreased or increased by a constant offset of 0.01. The best-fit model parameters were obtained from both data sets using the same methods applied to the original observations, and the results are listed in Table 4.1. Although we would intuitively expect the photospheric fraction to increase when the data are shifted to higher values, other parameters are also affected since a linear shift in V^2-values cannot be expressed as a single adjustment of the $c_{\rm p}$ parameter (recall eq. [4.3]). In fact, a constant positive shift in V^2-values corresponds to larger changes at the lower visibility values, thus making the data look “less resolved,” and produces smaller values for the angular extent of the circumstellar region, as can be seen in Table 4.1. The axial ratio and the P.A. of the major axis are also affected by the systematic shift, although ϕ is not very sensitive to the shift since it depends not only on the V^2-values but also on the position angles of the individual baselines. Because r depends on both the lower as well as the higher visibility values (due to the major and minor axes), and because the minor axis is not significantly resolved, it is affected slightly more by a constant shift in the data.

Based on the data in Table 4.1 we conclude that although our results can be affected by the presence of an additive bias, the magnitude of this effect is within our quoted uncertainties. This also justifies our use of the overestimated observational uncertainties which yield $\chi^2_\nu < 1$ and give us final uncertainties that also account for the possible presence of such a systematic offset.

4.5 Discussion

4.5.1 The Circumstellar Envelope

The circumstellar envelopes of Be stars are typically assumed to be thin, axisymmetric, circumstellar disks viewed at different angles, and therefore the axial ratio r is mostly due to a projection effect (see for example Wood, Bjorkman, & Bjorkman, 1997). This also means that both r and ϕ are not expected to vary in any significant way even if variability, such as one-armed oscillation, is present within the circumstellar disk. Our best-fit values for r and ϕ of 0.310 ± 0.072 and $-62\overset{\circ}{.}3 \pm 4\overset{\circ}{.}4$, which we have obtained for a single night, are in excellent agreement with the parameters reported by Quirrenbach et al. (1997) for observations obtained over a two month period in 1992. Their elliptical Gaussian model has an axial ratio of 0.28 ± 0.02 and P.A. of $-58° \pm 4°$, as well as an angular size of the major axis of 4.53 ± 0.52 mas.

It is not obvious that the apparent difference between our angular size of 3.14 ± 0.21 mas for the major axis and that of Quirrenbach et al. (1997) is in fact real. We have performed a number of tests to assess the significance of this apparent difference. We have tested the null hypothesis (that the size of the disk did not change) by treating $\theta_{\rm mj}$ as a fixed parameter in our model-fitting procedure. We used two values for $\theta_{\rm mj}$ based on the Quirrenbach et al. (1997) results, 4.53 and 4.01 mas (best-fit value minus 1σ), and at the expense of slightly worse fits (χ^2_ν of 1.73 and 1.03, respectively) we obtained similar results for r and ϕ as before (i.e., within their quoted uncertainties). Although in both cases the best-fit values for $c_{\rm p}$ were slightly larger, they were in agreement with our predicted value of 0.84 ± 0.01. Based on this analysis we conclude that we cannot confidently rule out the possibility that the size of the major axis was the same at the time of our observations and that of Quirrenbach et al. (1997).

At the same time there is still a possibility that this difference is caused by an actual change in the extent of the circumstellar disk or is due to a different spatial position of an over-density region such as the one reported by Vakili et al. (1998). Although on 1999 March 16 the Hα profile observed by Banerjee et al. (2000) does not show a simple double emission structure, it does show clearly that the short wavelength side is weaker than the long wavelength side (i.e. $V/R < 1$). This is in the same direction as the V/R of ~ 0.7 reported by Guo et al. (1995) for the same epoch as the observations of Quirrenbach et al. (1997). Based on the analysis of Vakili et al. (1998), this suggests that the over-density region (if present) might be located in approximately the same region of the circumstellar disk and should affect the best-fit parameters of our simple elliptical models in a very similar way. On the other hand, it is interesting to note that the EW of Hα was larger (by about 16%) during the observations by Quirrenbach et al. (1997) than at the time of our observations (see the EW measurements by Guo et al. (1995) and Banerjee et al. (2000)). Therefore, if the apparent difference between our best-fit value for $\theta_{\rm mj}$ and that reported by Quirrenbach et al. (1997) is real, then this suggests that the physical extent of the circumstellar region is directly correlated with the strength of the Hα emission line. A logical extension of our study would involve the simultaneous NPOI and Hα

spectroscopic observations.

4.5.2 The Binary Component

ζ Tau is also a single-lined spectroscopic binary with a period of about 133 days and an eccentricity of ~ 0.15 (Harmanec, 1984; Jarad, 1987). The inclination of the axis of the orbital plane to the line of sight is estimated to be $60° < i_{\rm orb} < 90°$, based on the lack of eclipses and the presence of a hump in the radial velocity curve (see Floquet et al., 1989, and references therein). A similar lower constraint can be obtained on the angle between the rotational axis of ζ Tau and the line of sight by comparing the observed rotational velocity to the critical velocity predicted for a star of the same spectral type (Floquet et al., 1989). If we assume that the elliptical Gaussian model we obtained in § 4.4.1 represents an axisymmetric disk, then the lower limit for the inclination angle is $i_{\rm min} = \arccos(r) \sim 70°$. If we also assume that the circumstellar disk is geometrically thin, as suggested by Wood, Bjorkman, & Bjorkman (1997), we can then use this lower limit as an approximate inclination of the circumstellar disk. This inclination angle is in the same range as the inclination angles for the star and the binary orbit estimated by Floquet et al. (1989), and suggests that all three planes have roughly the same orientation.

We do not expect to detect the secondary in our data because it is likely to be much fainter than the primary. The mass of the secondary is estimated to be 1.0–1.4 $M_\odot$ (Harmanec, 1984; Jarad, 1987; Floquet et al., 1989). If it is a 1.4 $M_\odot$ main-sequence star, it would be an F star with $M_V \sim 3$ (Gray, 1992, p. 431). From the *Hipparcos* distance (ESA, 1997) of 128 ± 19 pc and the apparent V magnitude of 3.0, the M_V of the primary is -2.5 ± 0.3, or 5 mag brighter than the secondary. For this magnitude difference, the variation in V^2 as a function of spatial frequency would be $\lesssim 2\%$. Because spatial frequency is proportional to λ^{-1} on a given baseline, such variations would show up as variations in V^2 versus λ in the continuum channels. We see no variations above the 2% level in any of our scans, which is consistent with the expected magnitude difference.

Although we cannot detect the secondary component of the binary directly, we can still obtain an interesting result if we assume that the inclination angle of the orbital plane of the binary is the same as that of the circumstellar disk and use the published results from spectroscopy. Jarad (1987) estimated the basic parameters of the binary system of ζ Tau for various choices of the inclination angle (assuming that $M_{\rm primary} \approx 11.2\ M_\odot$) and for $i = 70°$

predicts a binary separation of 254 ± 20 $R_\odot$ and a Roche radius ($R_{\rm Roche}$) of the primary of 144 ± 12 $R_\odot$, which is obtained when the Roche lobe is approximated with a sphere of the same volume. At the distance of ζ Tau of 128 ± 19 pc, the binary separation is 9.2 ± 1.5 mas and $R_{\rm Roche}$ is 5.3 ± 0.9 mas. Figure 4.6 shows the schematic representation of the projected circular orbit of the secondary component (we neglect the small eccentricity) and the extent of the Roche radius in the plane of the disk, along with our best-fit elliptical Gaussian model.

The inferred binary separation is large enough to place the secondary component outside the circumstellar disk, in agreement with many models (see, e.g., Castle, 1977). Furthermore, the disk lies well within the Roche radius, since the outermost disk radius, which we take to be the 1% level of our Gaussian model, is ~ 4 mas, which suggests that the disk may be truncated by tidal interaction with the secondary. If this is the case, we would not expect to find any strong radio emission from a region much more extended than the Hα-emitting region (in fact, Taylor et al., 1990, did not detect any radio emission for the ζ Tau system). The ζ Tau system might be one of the few Be stars for which the presence of a nearby companion limits the extent of the circumstellar disk.

4.5.3 Alternative Models

In § 4.4 we fitted an elliptical Gaussian model to the data from the Hα channel. As stated in § 4.4.1 the choice of this particular model allowed us a direct comparison with the results published in the literature where the same model was used. Furthermore, because this simple model only has four free parameters, it helps us avoid over-interpreting the observational data.

Gaussian models are not the only simple models that can be used to represent the circumstellar region. For example, an elliptical uniform disk, which contains the same number of free parameters, can also be used. In fact, because the Hα emission is expected to be optically thick, and if the temperature in the circumstellar disk is roughly constant (as suggested by Millar & Marlborough, 1999a,b,c) then one could argue that an uniform disk might be a better representation of the possible uniform brightness distribution in the Hα-emitting part of the envelope. For this reason we have modified the model given by equation (4.3), which is fitted to the squared visibilities from the Hα channel, by modeling the envelope component with an elliptical uniform disk whose model visibilities are given by

$$V_{\rm env}(u_{x'}, v_{y'}) = 2\frac{J_1\left(\pi\theta'_{\rm mj}\sqrt{r^2u_{x'}^2 + v_{y'}^2}\right)}{\left(\pi\theta'_{\rm mj}\sqrt{r^2u_{x'}^2 + v_{y'}^2}\right)}, \tag{4.5}$$

where all the variables have the same definition as in equation (4.4) with the exception that $\theta'_{\rm mj}$ represents the full angular extent of the major axis of the uniform disk.

We have performed a non-linear least-squares fit of the above model (in conjunction with the UD model representing stellar photosphere via eq. [4.3]) to the data and obtained the best-fit parameters of $\theta'_{\rm mj} = 5.93 \pm 0.36$, $r = 0.32 \pm 0.12$, $\phi = -62\overset{\circ}{.}1 \pm 5\overset{\circ}{.}4$, and $c_{\rm p} = 0.855 \pm 0.008$. We have also obtained a χ^2_ν value of 0.5 and therefore the elliptical uniform disk can model the data equally well as the elliptical Gaussian model. Furthermore, our best-fit values for the axial ratio and the position angle of the elliptical uniform disk are exactly the same as the best-fit values obtained for the same parameters in the case of the elliptical Gaussian (recall Table 4.1). The fractional contribution from the stellar photosphere, $c_{\rm p}$, is slightly larger for the elliptical uniform disk model, but still fully consistent with the expected value derived in § 4.4.2. Naturally, the angular extent of the major axis of the uniform disk, $\theta'_{\rm mj}$, is larger than in the case of the Gaussian model because it describes the full extent of the region (recall that $\theta_{\rm mj}$ is the FWHM measure of the Gaussian). In Figure 4.9 we demonstrate that indeed the two models are essentially indistinguishable at spatial frequencies of ≤ 50 Mλ for baseline orientations that resolve the major axis, and at even higher spatial frequencies for orientations at which the angular extent of the circumstellar region is smaller (due to the apparent ellipticity). Because we do not have any observations at spatial frequencies much higher than ~ 55 Mλ, even at the longest baseline (which in fact does not even cover the same position angles as the orientation of the major axis), our data cannot help us preferentially choose one model over the other.

Accepting the elliptical uniform disk as an alternative description of the Hα-emitting region allows us to estimate an approximate temperature in the circumstellar disk. Although an accurate temperature determination would have to account for the detailed energetics in the disk due to all the heating and cooling mechanisms, as well as account for the optical depth effects, we can obtain a rough estimate of the temperature by assuming that the disk radiates like a black body. In this case the flux received at Earth can be expressed as

$$f_\lambda = \frac{(\pi a^2 r)\pi B_\lambda}{4\pi d^2}, \tag{4.6}$$

where a is the semi-major axis of the elliptical disk, r is the axial ratio, d is the distance to the source, and B_λ is the black body source function (i.e., Planck's radiation law). Because in our case $a/d = \theta'_{\rm mj}/2$ we can rewrite the above equation as

$$B_\lambda = \frac{16 f_\lambda}{r\pi(\theta'_{\rm mj})^2}. \tag{4.7}$$

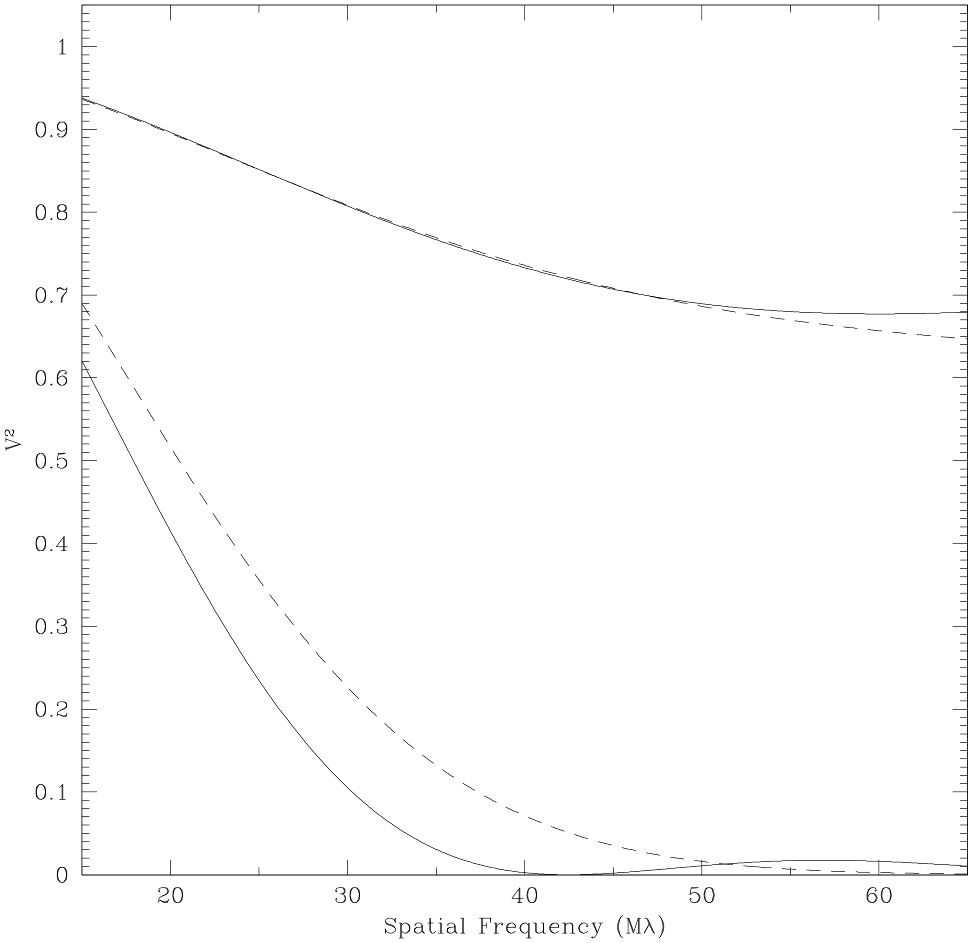

FIGURE 4.9: Squared model visibilities for a uniform disk of an angular diameter of 5.93 mas (*solid line*) and a Gaussian model with a FWHM of 3.14 mas (*dashed line*). The lower two curves correspond to the disk models alone (i.e., V_{env}^2 values). The upper two curves correspond to the normalized sum of two models, $[c_{\mathrm{p}}V_{\mathrm{p}} + (1 - c_{\mathrm{p}})V_{\mathrm{env}}]^2$, where V_{p} is the visibility of the UD model representing the stellar photosphere. For the combined squared visibilities the best-fit c_{p} values of 0.855 and 0.814 were used for the uniform and Gaussian disks, respectively.

To obtain a value for B_λ we must first estimate the received flux at the Hα line. In Figure 7.1 we show a typical Hα profile obtained for ζ Tau where the emission line peaks at 3.4 times the continuum level. In Chapter 7 we also estimate the apparent stellar flux above Earth's atmosphere based on the photometry and distance to the star (see Table 7.3), and for the continuum level in the Hα region derive $f_{\rm cont} \approx 1.45 \times 10^{-5}$ erg s^{-1}m^{-2}nm^{-1}. Therefore, assuming that $f_\lambda = 3.4 f_{\rm cont}$ and using our best-fit values for r and $\theta'_{\rm mj}$ we obtain $B_\lambda \sim 9.6 \times 10^{11}$ erg s^{-1}m^{-2}nm^{-1}, which at the wavelength of the Hα line corresponds to a black body with $T \sim 9,000$ K. It is interesting to note that the temperature we derive for the circumstellar disk using the above assumptions is quite consistent with the range of temperatures Millar & Marlborough (1999c) obtain in their disk models by accounting for all the sources of energy gain and loss.

4.6 Summary

We have fitted an elliptical Gaussian model to interferometric observations of ζ Tau obtained on 1999 March 1 with the NPOI and have shown that it effectively describes our data. We have also shown that a circularly symmetric Gaussian model is not capable of modeling the data. Our best-fit values for the axial ratio and P.A. of the elliptical Gaussian describing the circumstellar region of ζ Tau confirm the values reported by Quirrenbach et al. (1997) for observations of the same star obtained about seven years earlier. We conclude that the orientation of the disk does not appear to change on time scales much longer than the orbital period of the binary. We also conclude that the circumstellar envelope is smaller than the size derived by Jarad (1987) of the Roche lobe of the primary component of the binary.

Although our best-fit value for the major axis $\theta_{\rm mj}$ appears to be smaller than the value reported by Quirrenbach et al. (1997), obtained when the Hα emission was stronger, the difference is only slightly larger than the sum of the formal errors, and therefore it is difficult to assess the significance of this change. If this difference in $\theta_{\rm mj}$ is real, it suggests that the size of the circumstellar envelope is correlated with the strength of the Hα emission. Further interferometric observations of this system, preferably using the same instrumental setup, should be capable of investigating the relationship between the Hα emission strength and the characteristics of the circumstellar envelope.

We have shown how Gaussian and uniform disk models can have very similar squared visibilities (recall Fig 4.9), even though in the image domain they are quite distinct. In fact, to be able to distinguish any differences between the two models observations at spatial frequencies of > 55 Mλ are required. Because we reach this lower limit with our 37.5 m baseline, only slight improvement in the baseline length (something in the range of 50–70 m) will be more than sufficient to choose one model over the other. Also, because a number of other models that can be fit to the data, for example a power-law model, fall qualitatively between the Gaussian and the uniform disk models, we can conclude that our limited observational data would also be consistent with such models, and it would not be possible to choose these models over the simpler models without additional observations at higher spatial frequencies.

The variability of ζ Tau is known from spectroscopy (see for example Hanuschik et al., 1996), as well as from optical interferometry (Vakili et al., 1998), and thus it is important to acquire sufficient data to model the source characteristics on short enough time scales. We have demonstrated in this chapter that satisfactory model fits can be obtained from only 12 minutes of data using a three-beam configuration, and, therefore, the NPOI is capable of detecting intensity variations in the circumstellar environments of Be stars on short time-scales. This is an important and unique observational tool, especially if combined with simultaneous high spectral resolution Hα observations, that can probe new astrophysical phenomena.

Chapter 5

Observations of η Tauri

5.1 Introduction

The internal calibration technique has been applied successfully to Be stars with strong Hα emission, as it has been demonstrated in the previous two chapters. The strong Hα emission allows the interferometric observations to be obtained using wider spectral channels than it is possible for weak emission sources. This is directly related to the fact that if the contribution from the Hα emission to the total flux in the spectral channel gets too low, the signal from the circumstellar envelope might get lost in the noise (random or systematic) associated with the light originating in the stellar photosphere. Although the minimum level of the Hα emission required for the detection of the circumstellar envelope will depend on the noise level, we will test the internal calibration technique on a Be star with significantly weaker Hα emission than is typically observed for stars like γ Cas and ζ Tau. For this purpose we will apply the calibration method to archival observations of the Be star η Tauri (=HR 1165) obtained with the NPOI between 1997 and 1999.

5.2 Interferometric Observations

The Be star η Tau has been observed with the NPOI on many occasions, although most of the time not as a primary scientific target. In many instances it has been simply used as a reference, or a check star for observations of other targets, frequently binary systems. This resulted in a quite limited coverage of this star on any single night, but searching through the archival observations of NPOI we have found 19 nights from late 1997 to early 1999 that contained at

TABLE 5.1: OBSERVING LOG FOR η TAURI

Date	Number of scans
1997 Oct 15	5
1997 Nov 6	11
1997 Nov 7	10
1997 Nov 25	6
1997 Dec 5	3
1997 Dec 6	3
1998 Oct 7	5
1998 Oct 11	8
1998 Oct 12	3
1998 Nov 25	4
1998 Dec 11	2
1998 Dec 12	5
1998 Dec 24	18
1999 Feb 27	2
1999 Feb 28	3
1999 Mar 1	4
1999 Mar 4	2
1999 Mar 20	3
1999 Mar 25	3
Total	100

least some valid scans of η Tau. Some scans were excluded because of missing data on one of the baselines, or very low signal-to-noise ratio due to poor atmospheric conditions. Table 5.1 lists the dates and the number of scans of η Tau available for analysis from each night. We have a total of 100 uncalibrated scans that we combine into a single data set and the resulting (u, v)-plane coverage in the Hα is shown in Figure 5.1.

Fortunately, the instrumental configuration of the NPOI, for all practical purposes, was unchanged from 1997 until mid-1999. This applies not only to the baseline configuration, which involves the AW0, AE0, and AC0 astrometric stations (recall Fig. 2.7), but also to the spectral alignment of the output beams in the optics lab. We have seen in Chapter 4 how in the case of the observations of ζ Tau the spectral alignment of the output channels was such that the Hα emission ended up in the 665 nm channel at the two shortest baselines (18.9 and 22.2 m), and in the 648 nm channel at the longest baseline (37.5 m). We can verify if the alignment of the spectral channels for η Tau is the same as it was for observations of ζ Tau (which were obtained on 1999 Mar 1) by comparing the signal from the spectral channels that are expected to contain the Hα emission with those that do not.

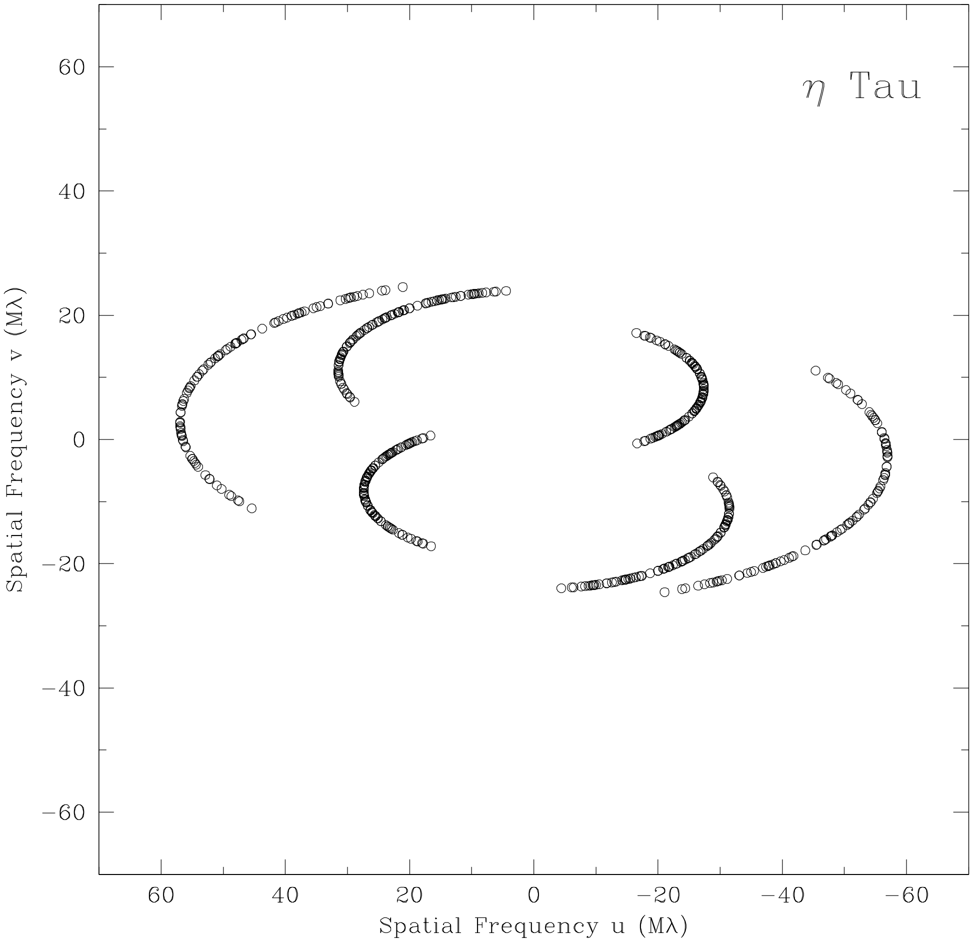

FIGURE 5.1: The Fourier (u, v)-plane coverage at Hα for observations of η Tau. The baselines have lengths of 18.9 m, 22.2 m, and 37.5 m with azimuths of $-67\overset{\circ}{.}5$, $63\overset{\circ}{.}6$, and $86\overset{\circ}{.}0$, respectively.

We begin by calibrating the V^2-values of η Tau using exactly the same method as was used in the case of ζ Tau (recall § 4.3), and assuming a UD diameter of 0.71 mas (Quirrenbach et al., 1997) for the photospheric component. The calibrated squared visibilities from the Hα containing channels are shown in Figure 5.2 along with the V^2-values for the UD model. The squared visibilities from the Hα channels systematically fall below the expected photospheric values, especially at the higher spatial frequencies. We interpret this as a direct signature of a resolved circumstellar envelope that is responsible for the Hα emission. Figure 5.3 demonstrates that when the spectral channels (648 and 665 nm) at all three baselines are reversed, we end up with a plain photospheric signature. This signature, in the 648 and 665 nm channels without the Hα emission, is very similar to the signature seen in the continuum channels at both, shorter (Fig. 5.4) and longer (Fig. 5.5) wavelengths. Based on this, we conclude that all of the Hα emission is captured in a single spectral channel at all three baselines (as was also the case for ζ Tau, but not for γ Cas).

5.3 The Hα Emission

The interferometric observations of η Tau cover a period of almost one and a half years (see Table 5.1), and because we want to model all of these observations with a single model, we need to verify that the Hα emission of η Tau is in fact stable on such long-time scales. To obtain a quantitative measure of the relative stability of the Hα emission the height of the peak intensity above the continuum, combined with the width of the emission, can be used. Similarly, the Hα equivalent widths from different epochs can be compared, but because EW is an integrated quantity it is less sensitive to the actual changes in the shape of the emission line (i.e., lines of different shapes can have the same EWs). The actual measurements of the peak intensity and the EW are dependent on the continuum level, and therefore different normalizations of the continuum level (by different observers) might result in numerical differences, which are not real. Also, the comparison of EW measurements collected from different sources is not straightforward, because different observers can, and usually do, define the EW differently. This especially becomes important for emission lines that do not completely fill in the underlying absorption lines.

Because η Tau is a well known Be star, its Hα emission has been observed on many occasions. For example, the Hα profiles from 1980 (Andrillat & Fehrenbach, 1982), 1982 (Hanuschik

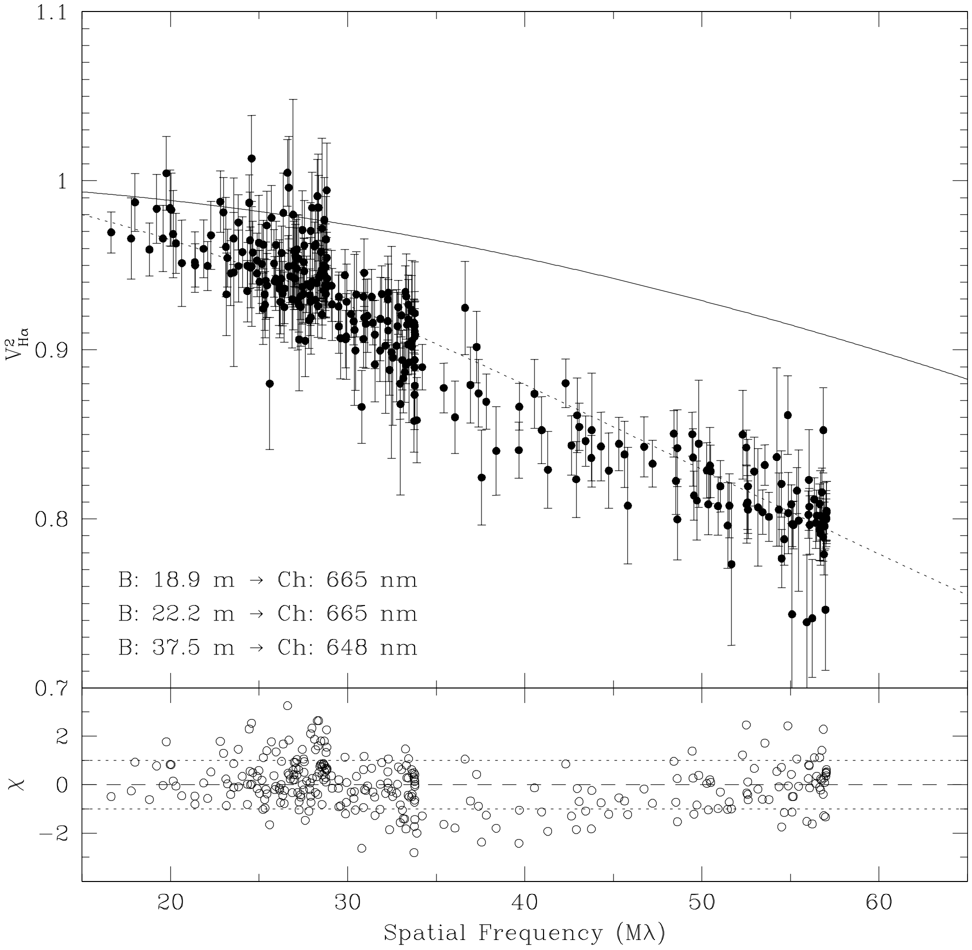

FIGURE 5.2: Calibrated squared visibilities of η Tau for the spectral channels that contain the Hα emission (i.e., 665 nm channel for the 18.9 and 22.2 m baselines, and 648 nm channel for the 37.5 m baseline). The uniform disk model representing the stellar photospheric disk (*solid-line*) and the best-fit circularly symmetric Gaussian model (*dotted-line*) are also shown. The normalized residuals for the circularly symmetric Gaussian are shown in the lower panel.

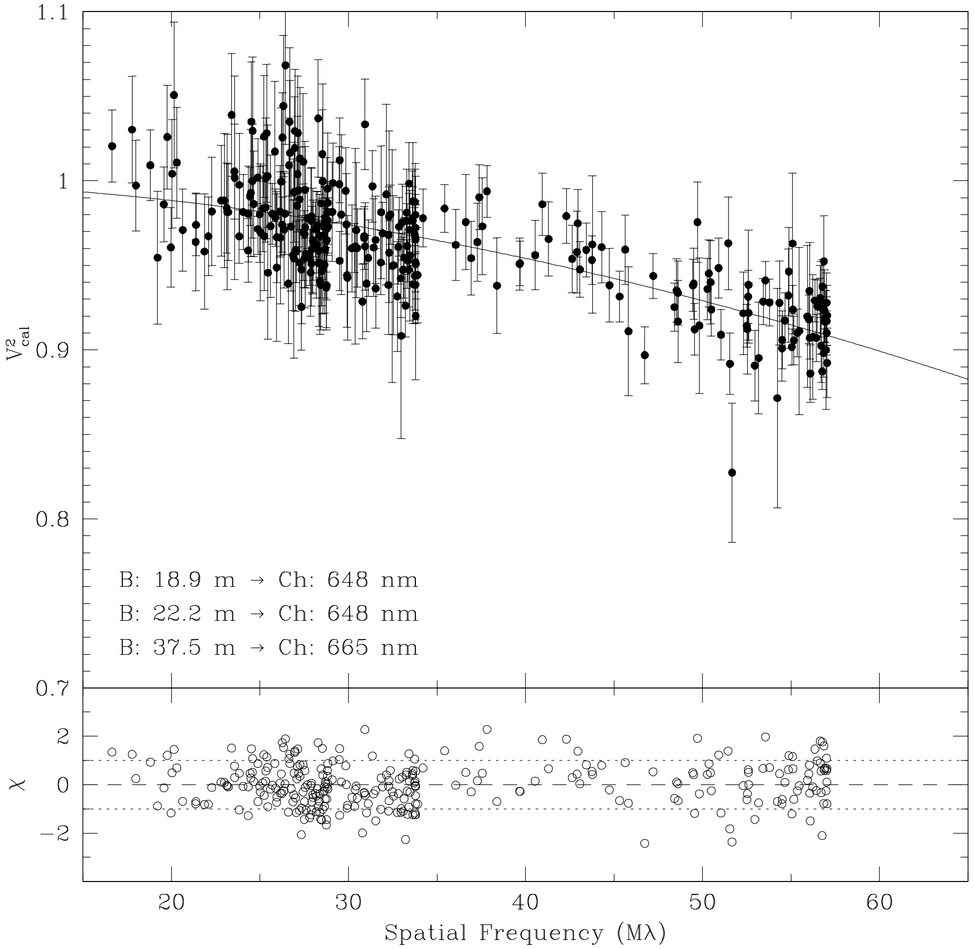

FIGURE 5.3: Same as Fig. 5.2 but with the choice of the spectral channels reversed (i.e., the 648 nm channel was used for the two shortest baselines and the 665 nm channel for the longest baseline). The residuals in the lower panel are calculated with respect to the uniform disk model representing the stellar photosphere.

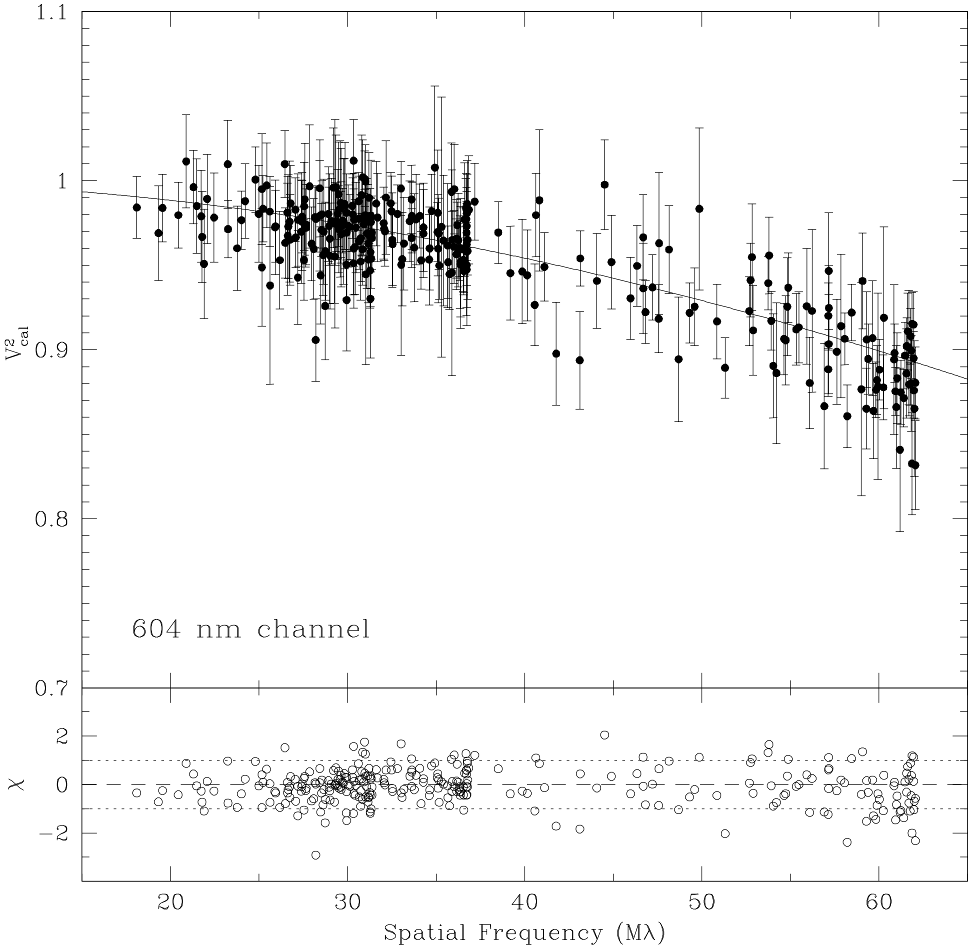

FIGURE 5.4: Same as Fig. 5.3 but for the continuum channel at 604 nm.

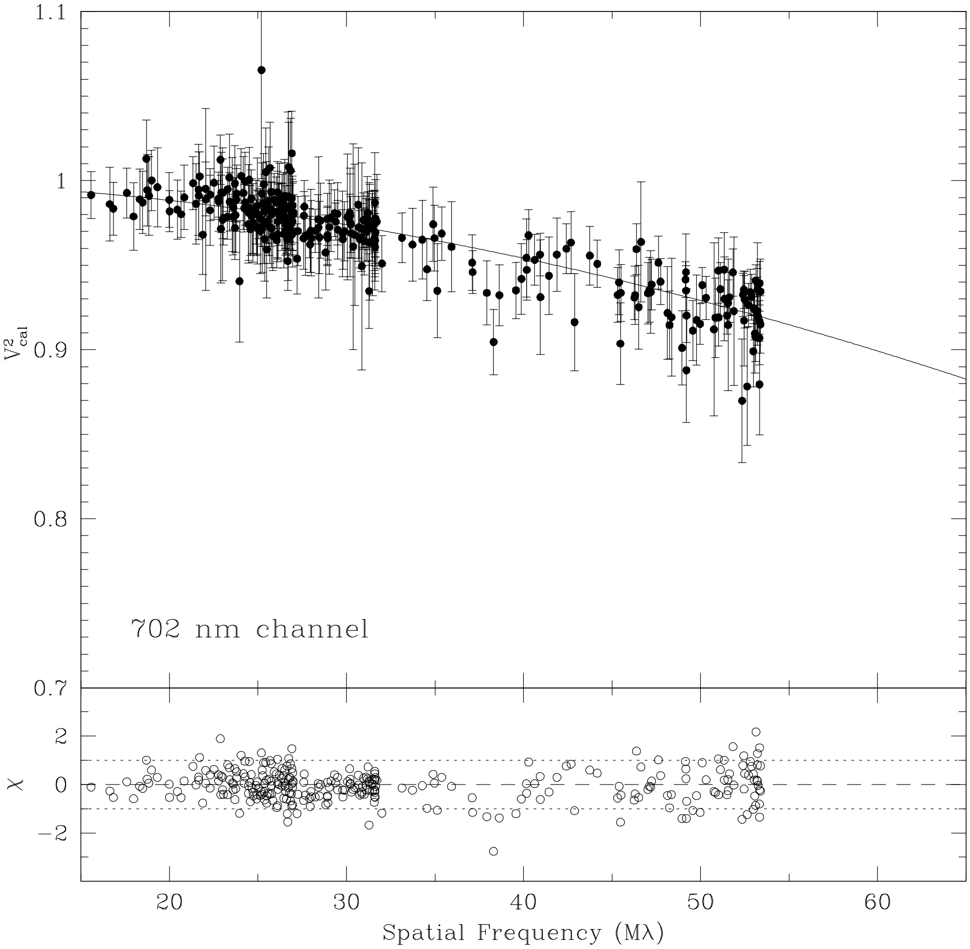

FIGURE 5.5: Same as Fig. 5.3 but for the continuum channel at 702 nm.

et al., 1996), 1989 (Hanuschik et al., 1996; Slettebak, Collins, & Truax, 1992), 1999 (Banerjee et al., 2000), and 2004 (see Fig. 5.6), all appear to have the same shape. Furthermore, all of the Hα profiles in the above references have widths (FWHM) that are in complete agreement with the width of 0.50±0.01 nm (or 229±5 km s^{-1}) that we obtain for the profile we observed in 2004 (Fig. 5.6). The peak intensity of the emission (at ~2.1 times the continuum level) is also the same for all profiles with the exception of the profile shown by Banerjee et al. (2000), where the emission is higher above the continuum (at approximately 2.7 times the continuum level) than in all other cases. This is most likely related to the fact that the observations of Banerjee et al. (2000) have spectral coverage of $\Delta\lambda \approx 2.5$ nm, which is narrower than the full extent of the underlying absorption line (that is not completely filled in), and therefore their Hα profiles are the most susceptible to incorrect normalization of the continuum level. Treating the extended wings of the absorption component as the continuum level will then result in an overestimation of the peak intensity of the emission component.

Considering the possible differences in the relative normalization of the continuum level by different observers, we conclude that the overall strength of the Hα emission of η Tau remained roughly constant (at approximately 2.1 times the continuum level) over the last two decades. Furthermore, the FWHM measurements, which are mostly immune to the normalization of the continuum level, are clearly unchanged over the same period, and this suggests that the Hα emission is in fact stable on long-time scales. We can therefore model our ensemble of interferometric observations, collected over a period of one and a half years, with a single model.

5.4 Results and Discussion

To be consistent with the modeling of the Hα emitting envelopes of γ Cas and ζ Tau, that we have conducted in Chapters 3 and 4, we need to model the envelope of η Tau with an elliptical Gaussian model (recall § 2.3). We first fit a circularly symmetric Gaussian to the data by keeping the r value fixed at unity. For the two-parameter fit we obtain best-fit values for the model parameters of $\theta_{\mathrm{mj}} = 1.94 \pm 0.12$ and $c_{\mathrm{p}} = 0.895 \pm 0.010$. As expected, based on the weak Hα emission, the contribution from the stellar photosphere to the net signal in the Hα channel is large (roughly 90%).

The V^2-values of the best-fit circularly symmetric Gaussian model are shown in Figure 5.2

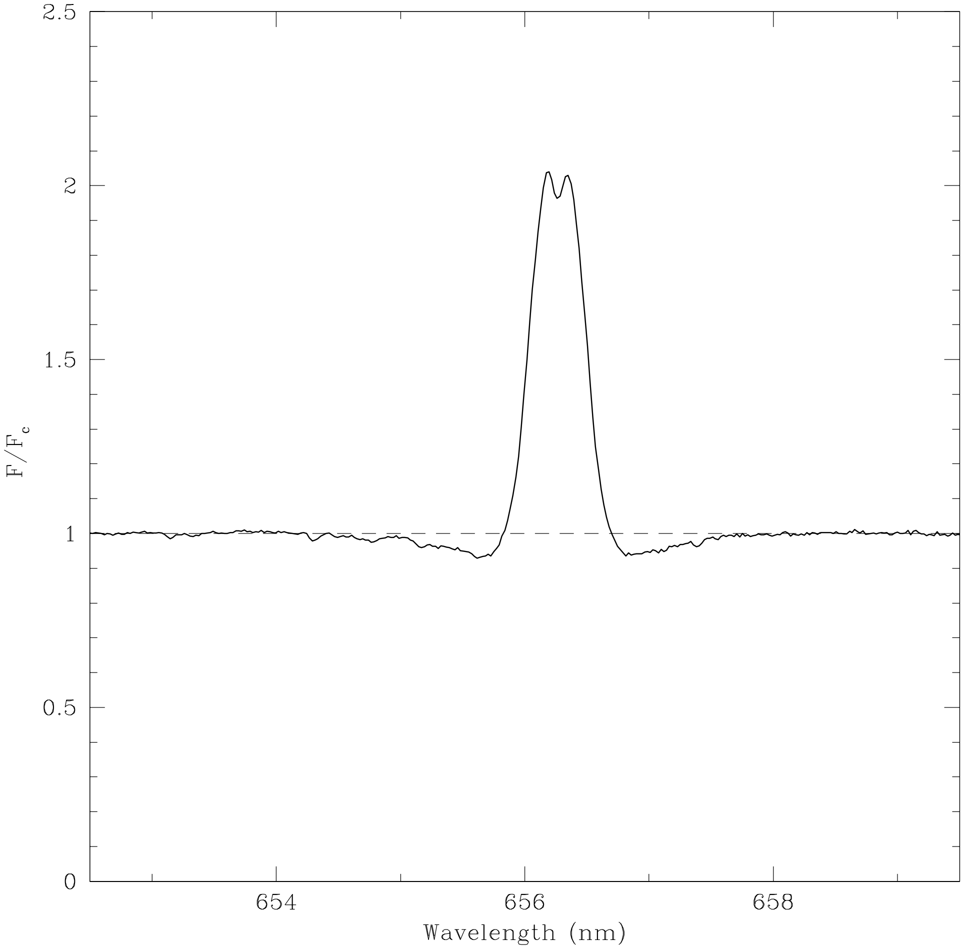

FIGURE 5.6: The Hα profile of η Tau obtained on 2004 March 8 with the Solar-Stellar Spectrograph (see also the description of the observations in § 7.2.2). The spectrum has been normalized with respect to the continuum level (*dashed line*).

Table 5.2: Best-Fit Model Parameters for η Tauri

$\theta_{\rm mj}$ (mas)	r	ϕ (deg)	$c_{\rm p}$	χ^2_ν
1.94 ± 0.12	1	...	0.895 ± 0.010	1.03
2.08 ± 0.18	0.753 ± 0.053	44.6 ± 9.4	0.893 ± 0.015	0.88

along with the resulting normalized residuals. The majority of the data points do not deviate from the model by more than one standard deviation, although the residuals in Figure 5.2 (that have a χ^2_ν of 1.03) show more variation than the residuals seen in the spectral channels without the Hα contribution (see the residuals in Figs. 5.3, 5.4, and 5.5 that have χ^2_ν values of 0.83, 0.57, and 0.43, respectively). In fact, when the residuals from the circularly symmetric Gaussian are plotted as a function of the position angle on the sky, a weak dependence is revealed (see Fig. 5.7). At the same time, the magnitude of this variation is at the same level as the possible systematic offset due to the limitation of the bias correction, and thus it is possible that this variation is caused entirely by the systematic errors. It is interesting to note that the residuals for the spectral channels without the Hα emission, particularly the continuum channels, do not show such variations as a function of PA (see Figs. 5.8 through 5.10).

If the variations in the residuals as a function of the PA shown in Figure 5.7 are real, then this suggests that the circularly symmetric model slightly overestimates the data at small position angles and underestimates at larger angles. This is consistent with a circumstellar envelope that deviates from circular symmetry and has its major axis positioned at an angle of $< 90°$. Indeed, fitting an elliptical Gaussian to the data yields a PA of the major axis of $44\overset{\circ}{.}6 \pm 9\overset{\circ}{.}4$ and an axial ratio of 0.753 ± 0.053. The remaining best-fit model parameters are listed in Table 5.2 along with the model parameters for the circularly symmetric model. By comparing the χ^2 values for the two models we can conclude that the elliptical Gaussian model produces a slightly better fit, but we cannot rule out that the apparent ellipticity is caused by the systematic offsets. It is interesting to note that Quirrenbach et al. (1997), who observed η Tau with the Mark III interferometer (and thus were influence by different systematic errors), reported similar model parameters for this star (r of 0.95 ± 0.22, PA between 19° and 48°, and $\theta_{\rm mj}$ of 2.65 ± 0.14).

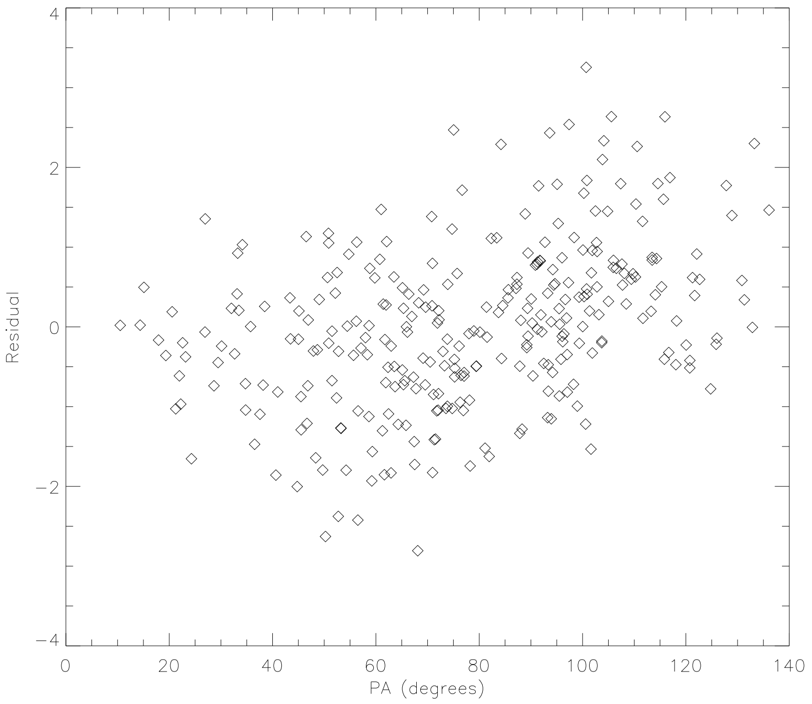

FIGURE 5.7: Same as the residuals shown in the lower panel of Fig. 5.2, but plotted as a function of the position angle on the sky.

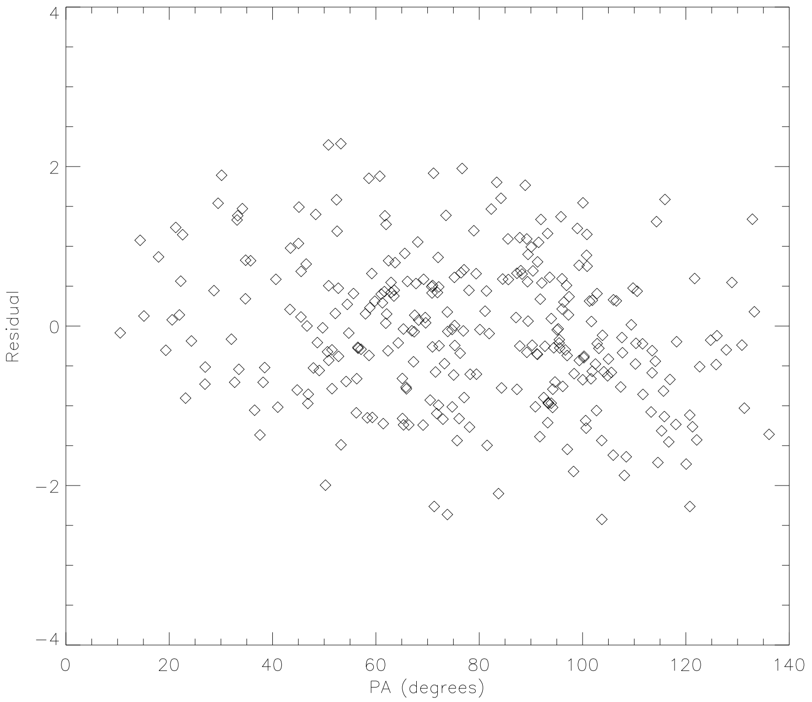

FIGURE 5.8: Same as Fig. 5.7, but for the residuals calculated with respect to the UD model in the 648 and 665 nm channels without the Hα emission.

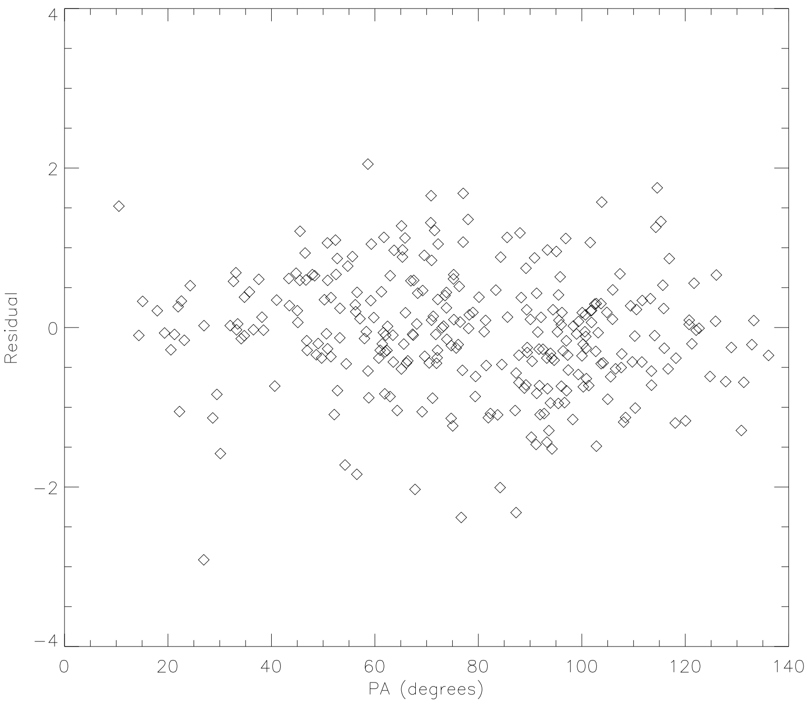

FIGURE 5.9: Same as Fig. 5.7, but for the residuals calculated with respect to the UD model in the 604 nm channel.

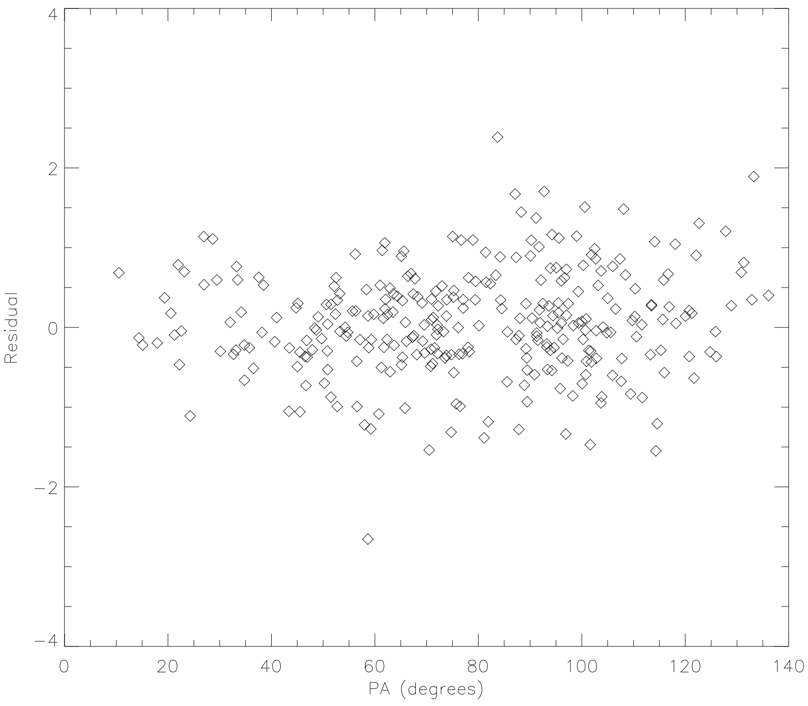

FIGURE 5.10: Same as Fig. 5.7, but for the residuals calculated with respect to the UD model in the 702 nm channel.

Chapter 6

Observations of β Canis Minoris

6.1 Introduction

The Hα-emitting circumstellar regions of classical Be stars are quite challenging objects to resolve spatially. This is a direct result of the fact that even in the case of the brightest objects, which are also typically the closest, baselines of tens of meters are necessary to resolve these envelopes sufficiently well so that an estimate of the angular extent of the region can be obtained. A good example of such star is β Canis Minoris (=HR 58715), which at a distance of about 52.2 ± 2.4 pc (ESA, 1997), still required baselines of up to 30 m to be resolved by the Mark III interferometer (Quirrenbach et al., 1997). What is even more interesting is that Quirrenbach et al. (1997) failed to detect any signature of asymmetry of the Hα emitting envelope. This is in contrast with the relatively high $v \sin i$ value obtained for this system, which suggests that we are not looking at the system pole-on. Therefore, the deviation from circular symmetry of the Hα-emitting region of β CMi has yet to be detected by long-baseline interferometry.

In this chapter we analyze the observations of β CMi obtained with the NPOI, and show that it is the weak Hα emission that makes the detection of the asymmetry of the Hα-emitting region so challenging. We also demonstrate that the expected degree of asymmetry, as deduced from the observed $v \sin i$ value, is consistent with our data, but to confidently measure the actual degree of ellipticity, narrow-band interferometric observations are required.

6.2 Estimating the Inclination Angle

We can estimate the inclination angle (i) between the rotational axis of β CMi and the line-of-sight using the observed $v \sin i$ value of 245 ± 25 km/s reported by Slettebak (1982) and an estimated critical velocity for a star of the same spectral type. Using the spectral type of B8 Ve for β CMi (Hoffleit & Jaschek, 1982) and the critical velocities tabulated by Porter (1996), we estimate a $v_{\rm crit}$ of 397 km/s. Because stars cannot rotate at velocities greater than $v_{\rm crit}$, we expect

$$(v \sin i)_{\rm obs} \leq v_{\rm crit} \sin i, \tag{6.1}$$

which can be rewritten in terms of a lower limit on the inclination angle

$$i \geq \sin^{-1}\left[\frac{(v \sin i)_{\rm obs}}{v_{\rm crit}}\right], \tag{6.2}$$

which for β CMi results in a minimum value of $i_{\rm min} = 38° \pm 4°$. Porter (1996) analyzed a large sample of $v \sin i$ values derived for many Be stars and concluded that the distribution of rotational velocities as a function of critical velocity is sharply peaked near $\sim 0.7 v_{\rm crit}$. Therefore, if we assume that $v = 0.7 v_{\rm crit}$ we obtain a most likely value for i of $\sim 60°$.

To deduce an upper limit on the value of i, we compare the shape of the Hα profile of β CMi with those of other Be stars for which observational constraints on the inclination angle already exist. For example, comparing the shapes of the Hα profiles for β CMi and ζ Tau (compare, for example, the profiles in Figs. 17 and 35 of Hanuschik et al., 1996), reveals that β CMi has a narrower two-peak structure with a much less pronounced central depression (see also Fig. 6.1). Indeed, based on the profile classification scheme developed by Hanuschik et al. (1996), β CMi is viewed at an inclination angle which is less than that of ζ Tau. Because we have already obtained an inclination angle of $\sim 70°$ for ζ Tau (Ch. 4), we conclude that in the case of β CMi the upper limit for i is $\lesssim 70°$. Combining our estimates for the lower and upper limits of i leads to our best estimate for the inclination angle for β CMi of $i = 60^{+10}_{-26}$ degrees. If we assume that the circumstellar envelope is a thin axisymmetric disk that is aligned with the stellar equator then the above range in the inclination angle implies an axial ratio of $r = 0.5^{+0.33}_{-0.16}$.

6.3 The Data

The observational data for β CMi is sparser than the data we analyzed in Chapter 5 for η Tau, although both data sets cover roughly the same period of one and a half years. We

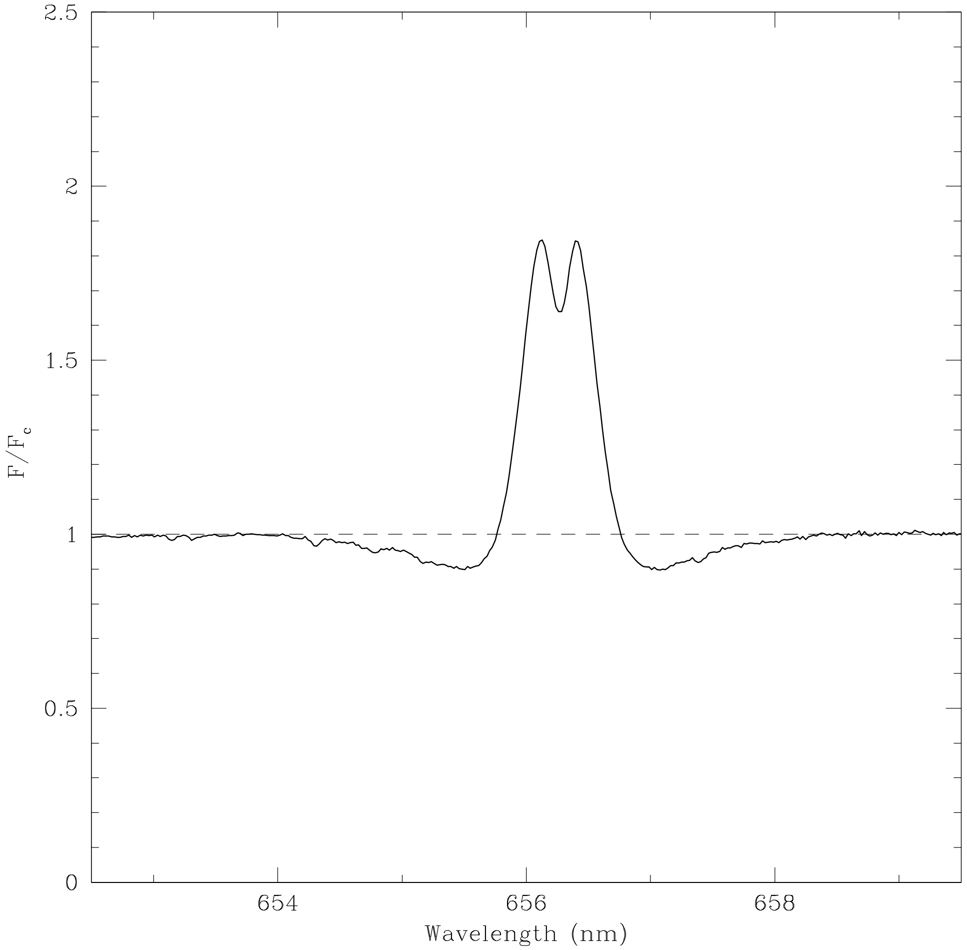

FIGURE 6.1: The Hα profile of β CMi obtained on 2004 March 8 with the Solar-Stellar Spectrograph (see § 7.2.2 for the description of the observations). The spectrum has been normalized with respect to the continuum level (*dashed line*).

TABLE 6.1: OBSERVING LOG FOR β CANIS MINORIS

Date	Number of scans
1997 Nov 6	4
1997 Nov 7	2
1997 Nov 8	3
1998 Mar 22	4
1998 Nov 25	3
1999 Feb 27	2
1999 Apr 10	2
Total	20

have a total of 20 uncalibrated scans available for analysis (see Table 6.1), which result in a (u, v)-plane coverage (at the Hα channel) shown in Figure 6.2. We calibrate these scans using the same method as was used in the case of ζ Tau (recall § 4.3), except that the angular diameter of the UD model representing the photospheric component of β CMi was assumed to be 0.74 mas (Quirrenbach et al., 1997).

To verify that the spectral alignment for β CMi is the same as it was for η Tau (recall § 5.2), we compare the calibrated squared visibilities from the spectral channels that are expected to contain the Hα emission (see Fig. 6.3) with those that do not (see Figs. 6.4 through 6.6). Because the V^2-values systematically fall below the UD model values at the 665 nm channel of the shortest two baselines (18.9 and 22.2 m) and at the 648 nm channel of the longest (37.5 m), we conclude that similarly to our previous data sets only those channels contain the signal from the Hα-emitting envelope.

6.4 Resolving the Hα-emitting Envelope

Because the observations of β CMi span almost a year and a half, and we have only a small number of scans that we would like to treat as a single data set, we need to verify that the Hα emission is stable on such long-time scales. The line profiles from 1980 (Andrillat & Fehrenbach, 1982), 1989 (Hanuschik et al., 1996; Slettebak, Collins, & Truax, 1992), 1992 (Hanuschik et al., 1996), 1999 (Banerjee et al., 2000), as well as our own spectroscopic observations from 2004 (see Fig. 6.1), all show that the line shape, peak intensity (at ~1.8 times the continuum level), and the line width (FWHM of ~0.61 nm) remained essentially unchanged over the period covered by the observations. The small differences between the profiles, especially those of Banerjee et

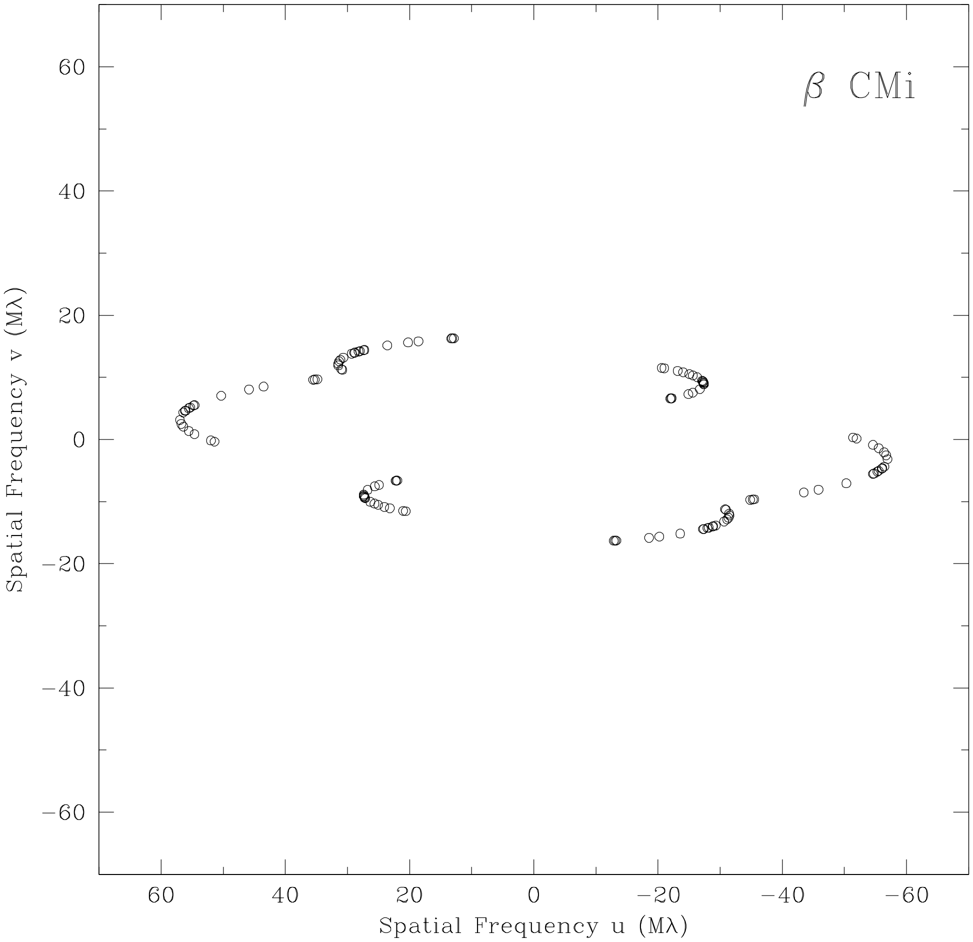

FIGURE 6.2: The Fourier (u, v)-plane coverage at Hα for observations of β CMi. The baselines have lengths of 18.9 m, 22.2 m, and 37.5 m with azimuths of $-67\overset{\circ}{.}5$, $63\overset{\circ}{.}6$, and $86\overset{\circ}{.}0$, respectively.

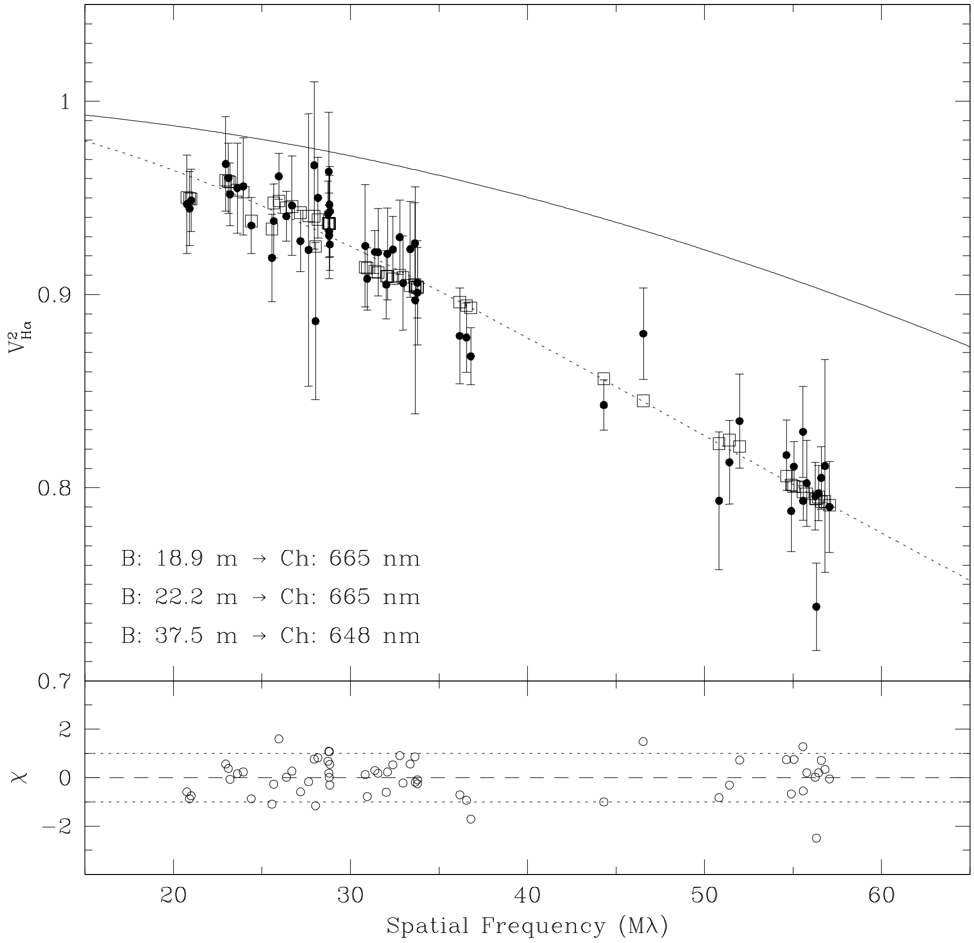

FIGURE 6.3: Calibrated squared visibilities of β CMi for the spectral channels that contain the Hα emission (i.e., 665 nm channel for the 18.9 and 22.2 m baselines, and 648 nm channel for the 37.5 m baseline). The uniform disk model representing the stellar photospheric disk (*solid line*) and the best-fit circularly symmetric (*dotted line*) and elliptical (*squares*) Gaussian models are also shown. The normalized residuals for the circularly symmetric Gaussian model are shown in the lower panel.

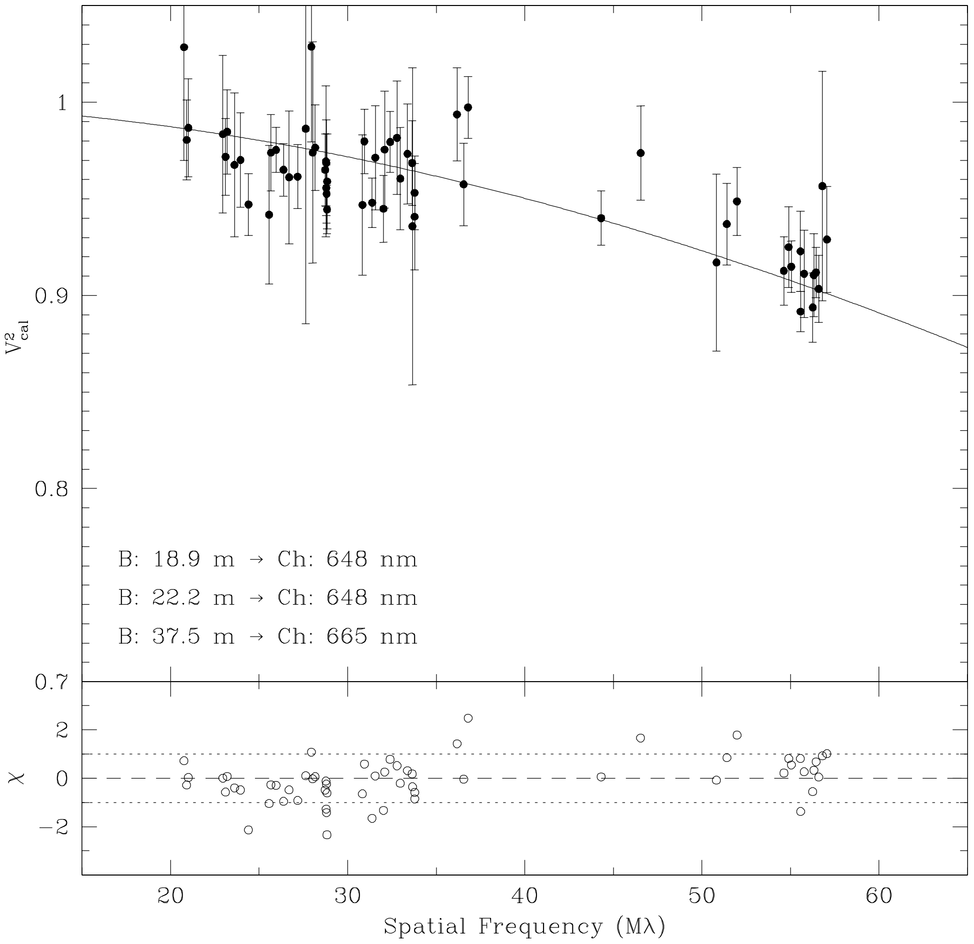

FIGURE 6.4: Same as Fig. 6.3, but with the choice of the spectral channels reversed (i.e., the 648 nm channel was used for the two shortest baselines and the 665 nm channel for the longest baseline). The residuals in the lower panel are calculated with respect to the uniform disk model representing the stellar photosphere.

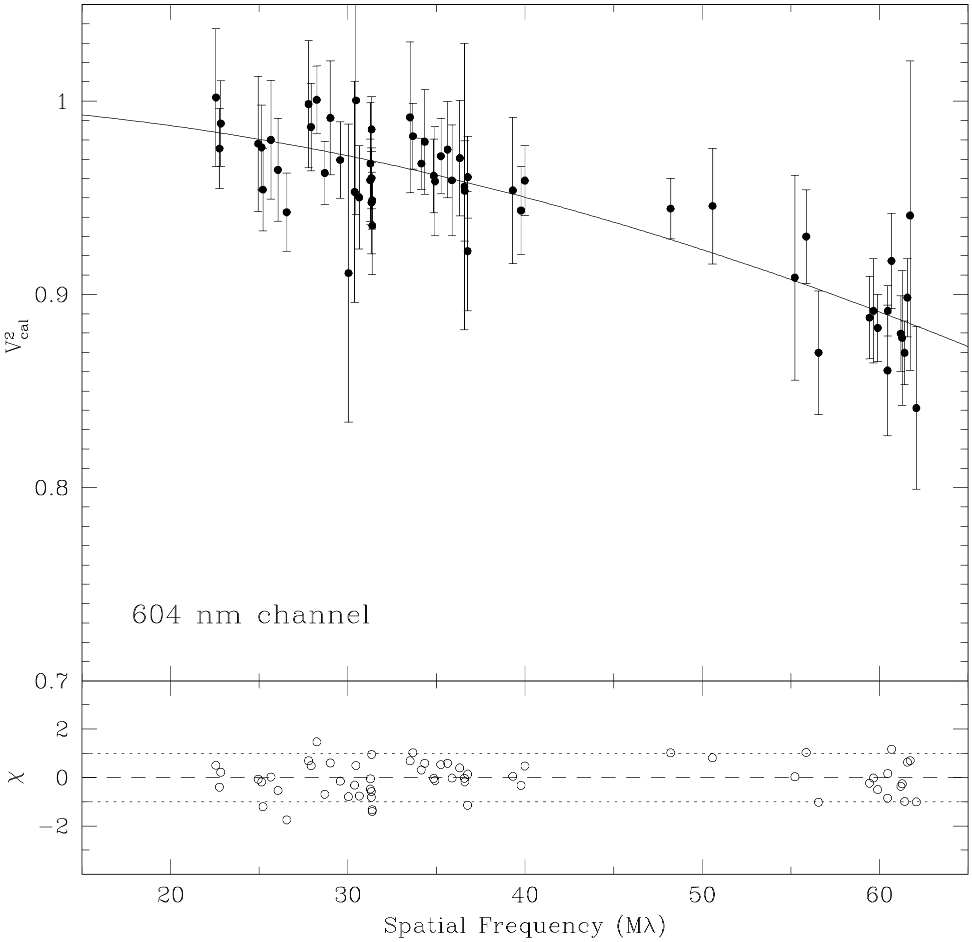

FIGURE 6.5: Same as Fig. 6.4, but for the continuum channel at 604 nm.

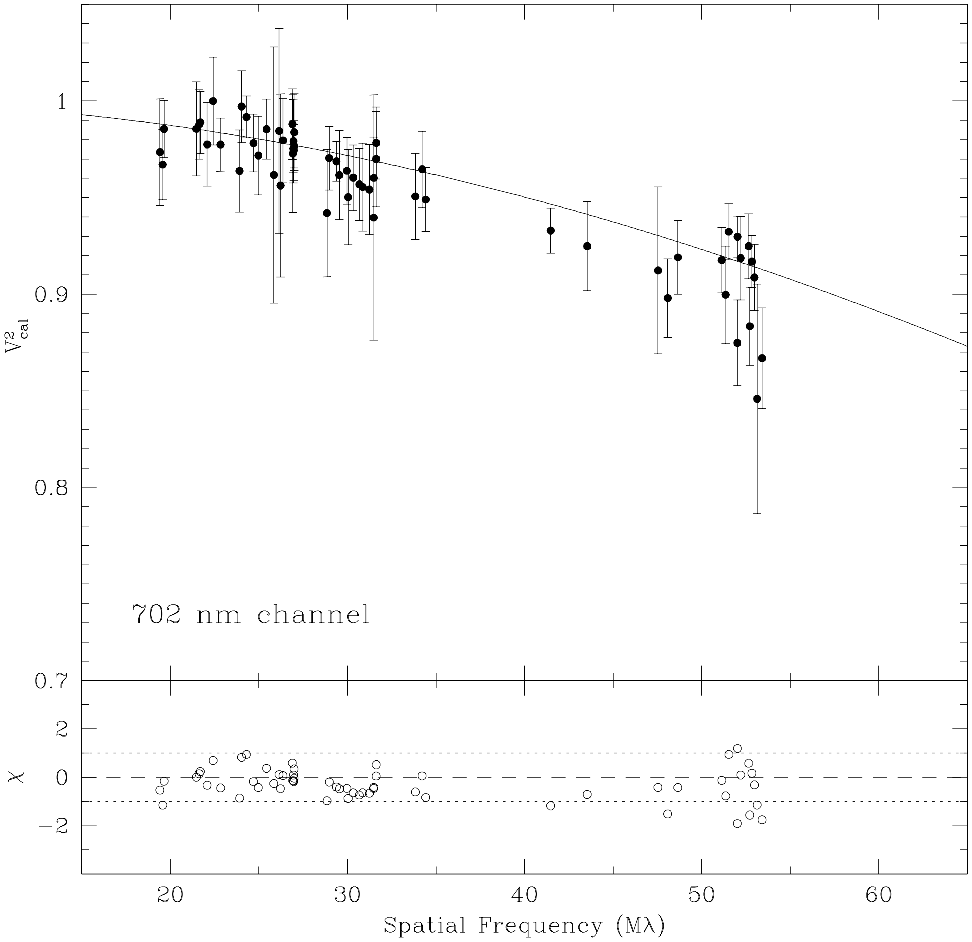

FIGURE 6.6: Same as Fig. 6.4, but for the continuum channel at 702 nm.

Table 6.2: Best-Fit Model Parameters for β Canis Minoris

$\theta_{\rm mj}$ (mas)	r	ϕ (deg)	$c_{\rm p}$	χ^2_ν
2.02 ± 0.28	1	...	0.904 ± 0.019	0.62
2.13 ± 0.50	0.69 ± 0.15	40 ± 30	0.874 ± 0.069	0.54

al. (2000) can be fully attributed to incorrect normalization of the continuum level that does not properly account for the photospheric absorption line that is not fully filled in by the emission component (see also the discussion in § 5.3). We conclude that the Hα emission of β CMi does not vary on time scales of years, and that we can model the twenty scans listed in Table 6.1 with a single model.

We have fitted both circularly symmetric and elliptical Gaussian models to the data. The best fit parameters are listed in Table 6.2. In the case of the elliptical Gaussian model the best-fit value of ϕ appeared to have a slight dependence on the initial guess (a starting value in the non-linear least-squares fit), but generally converged in the range of 10°–70°. At the same time, the difference between the model V^2-values for elliptical and circularly symmetric Gaussians is at most ~1% (see Fig. 6.3) and therefore the detected signature of asymmetry is at the same level as the possible systematic offsets we have discussed in the previous chapters.

The reason why the signature of asymmetry is so small is directly related to the weak Hα emission. Because of this weak emission the net signal from the circumstellar envelope (even if fully resolved) can only amount to a maximum ~10% drop in the squared visibilities. The deviation from circular symmetry, which appears as slight differences in apparent angular size as the positional angle of the baseline is varied, produces even smaller changes in the V^2-values. Interferometric observations conducted using much narrower spectral channels would definitely eliminate this problem by decreasing the photospheric "contamination" in the spectral channel containing the Hα emission. Although the best-fit value for r should be treated with caution for the reasons discussed above, it is interesting to note that the best-fit value we have obtained from the non-linear least-squares fit is consistent with the expected range of $0.5^{+0.33}_{-0.16}$ we have estimated for r in § 6.2.

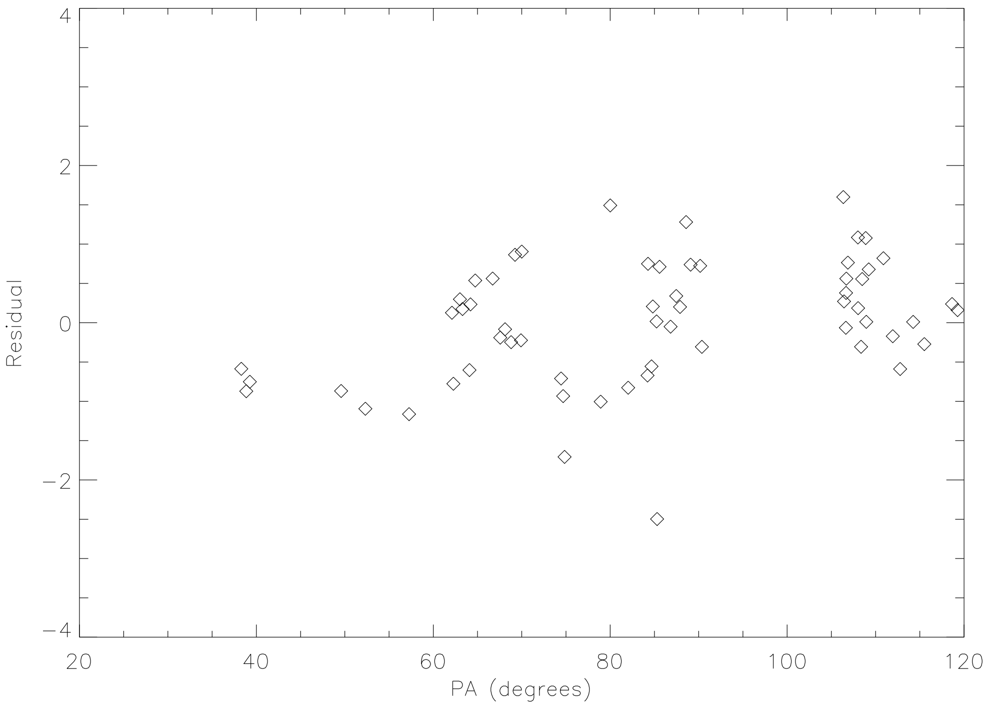

FIGURE 6.7: Same as the residuals shown in the lower panel of Fig. 6.3, but plotted as a function of the position angle of the corresponding baseline. Note: the approximate PA coverage by each baseline is 35°–72° (22.2 m), 73°–93° (37.5 m), and 111°–120° (18.9 m).

Chapter 7

Properties of the Hα-emitting Regions

7.1 Introduction

One of the expected, but not fully investigated, properties of Be stars is the correlation between the strength of the Hα emission line and the spatial extent of the circumstellar region. Although Quirrenbach et al. (1997) have shown that there is a tendency for stars with larger disks to have stronger Hα emission, there was also a considerable scatter present in their results. We will extend their analysis to account for the different flux levels in the Hα emission lines, and we will show that there is a clear relationship between the net emission and the physical extent of the Hα-emitting disk.

Another important property associated the circumstellar regions is the dependency of their physical sizes on stellar parameters, such as the effective temperature or the rotational velocity. Establishing a clear connection between such parameters might provide crucial tests of models for the disk formation around Be stars.

7.2 The Data

We have analyzed the observations of a total of four Be stars so far, and the properties of their Hα-emitting circumstellar envelopes have been presented in previous chapters. Because we model each Hα-emitting envelope in nearly the same way as Quirrenbach et al. (1997), we can also include their results for three extra Be stars that were not observed by the NPOI. This allows us to expand the data set, thereby making the correlations more apparent. Table 7.1 summarizes the names and the spectral types (from the Bright Star Catalogue, BSC, Hoffleit

TABLE 7.1: THE CIRCUMSTELLAR REGIONS OF BE STARS

HD (1)	Star (2)	Spectral Type (3)	π (mas) (4)	d (pc) (5)	$\theta_{\rm mj}$ (mas) (6)	r (7)	$D_{\rm mj}$ (10^9 m) (8)
5394	γ Cas	B0 IVe	5.32 ± 0.56	188^{+22}_{-18}	3.67±0.09	0.79±0.03	103^{+13}_{-10}
23630	η Tau	B7 IIIe	8.87 ± 0.99	113^{+14}_{-11}	2.08±0.18	0.75±0.05	$35.1^{+5.4}_{-4.7}$
37202	ζ Tau	B4 IIIpe	7.82 ± 1.02	128^{+19}_{-15}	3.14±0.21	0.31±0.07	$60.1^{+9.9}_{-8.0}$
58715	β CMi	B8 Ve	19.2 ± 0.85	$52.2^{+2.4}_{-2.2}$	2.13±0.50	0.69±0.15	$16.6^{+4.0}_{-4.0}$
10516	ϕ Per	B2 Vpe	4.55 ± 0.75	220^{+43}_{-31}	2.67±0.20	0.46±0.04	87.8^{+19}_{-14}
22192	ψ Per	B5 Ve	4.66 ± 0.73	215^{+40}_{-29}	3.26±0.23	0.47±0.11	105^{+21}_{-16}
25940	48 Per	B3 Ve	5.89 ± 0.72	170^{+24}_{-19}	2.77±0.56	0.89±0.13	70.4^{+17}_{-16}

NOTE.— Column 3: spectral type from the BSC. Column 4: parallax from the *Hipparcos* catalogue (ESA, 1997). Column 5: distance to the source. Column 6: the angular diameter of the major axis of the elliptical Gaussian model representing the Hα-emitting envelope. Column 7: axial ratio of the elliptical Gaussian model. Column 8: $\theta_{\rm mj}$ in physical units.

& Jaschek, 1982) of the Be stars analyzed in this work, along with those having previously published model parameters given at the bottom of the list. We see from the table that we have a range of different spectral types, and thus it should be possible to investigate not only the relationship between the Hα emission and the physical extent of the circumstellar region, but also to test for any obvious dependencies on spectral type.

Before we can properly investigate the above relationships, we need to account for the effects of different distances, as well as different continuum flux levels with respect to which the Hα equivalent widths are measured. We begin by discussing the sources of the observational parameters derived from both interferometric and spectroscopic observations of each star.

7.2.1 Model Parameters Describing the Circumstellar Regions

For the Be stars γ Cas, η Tau, ζ Tau, and β CMi, best-fit model parameters describing an elliptical Gaussian model have been obtained and presented in Chapters 3 through 6. These model parameters provide us with the angular size of the major axis ($\theta_{\rm mj}$) of each Hα-emitting region, as well as with the ratio of the minor to major axis (r). Quirrenbach et al. (1997) also provides the same model parameters from their best-fit models of ϕ Per, ψ Per, and 48 Per. All the model parameters we use in this analysis are compiled in Table 7.1.

Although we are using the best-fit model parameters derived from elliptical Gaussians model fits to the data for all of stars, we should also note that in some cases the detection of the deviation from circular symmetry has not been fully conclusive. For example, in Chapter 6 we have discussed how in the case of β CMi the expected signature due to the ellipticity of the region is at the same level as the possible systematic offsets. Nevertheless, for consistency as well as because the angular extent of the region derived from circularly symmetric and elliptical Gaussians can be quite similar, we use the model parameters for the elliptical Gaussians as the representative parameters describing the Hα-emitting regions.

7.2.2 Hα Equivalent Widths

The radiation from the circumstellar disk is characterized by the EW of the Hα emission line. As we have discussed in § 2.2.2, our interferometric observations do not contain this type of detailed spectroscopic information, and thus we need to rely on independently obtained spectroscopic observations. For Be stars that are known to possess Hα emission that is stable on long-time scales, it is not necessary to obtain spectra that cover the same time-frame as the interferometric observations. On the other hand, for stars whose variability is well documented, spectroscopic observations taken as close in time as possible to the interferometric observations are required. We have searched the literature for spectroscopic information on the Hα emission that would cover the same period as the interferometric observations we have analyzed in Chapters 3 through 6, which were acquired between 1997 and 1999, and those of Quirrenbach et al. (1997) that were obtained throughout 1992.

To check for consistency and long-term stability, we have also obtained echelle spectra of the four Be stars that were observed with the NPOI. The echelle spectra were obtained using the Lowell Observatory's Solar-Stellar Spectrograph (SSS) located at the same site as the NPOI. The description of the instrument and the IDL-based reduction package that was used to extract the spectra from the raw echelle orders have been described elsewhere (Hall et al., 1994). We have observed γ Cas and ζ Tau on 2003 December 9, and η Tau and β CMi on 2004 March 8. The resulting spectra of the Hα region, shown in Figure 7.1, have a resolving power of about 30,000 and a signal-to-noise ratio in the range of 150–200 at the continuum wavelengths, and higher at the emission line.

η Tau and β CMi

We have already discussed in §§ 5.3 and 6.4 how the emission profiles of η Tau and β CMi appear to be stable on time scales of tens of years. These are also the only stars in our sample that

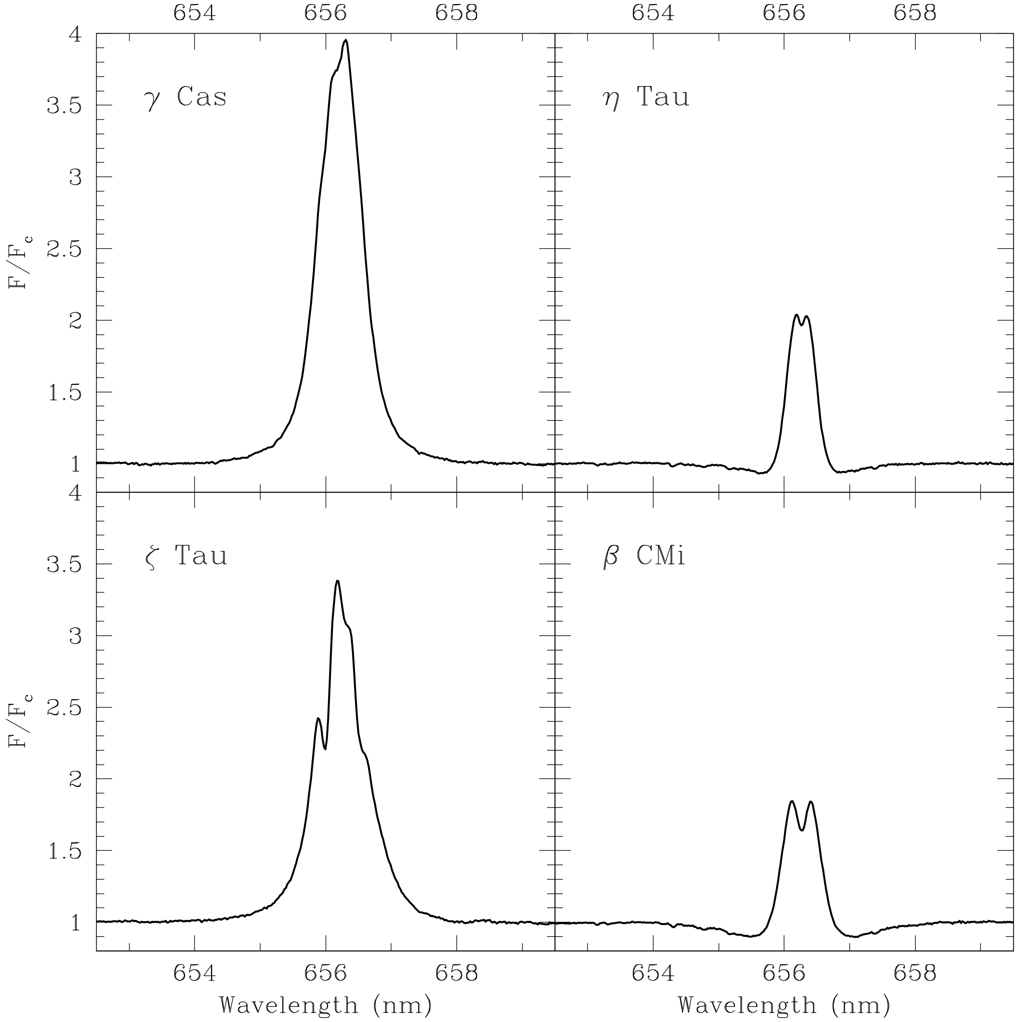

FIGURE 7.1: The Hα profiles of the four Be stars obtained with the Solar-Stellar Spectrograph. Each panel shows only a fraction of the 648–660 nm spectral region covered by the echelle order that contained the Hα line.

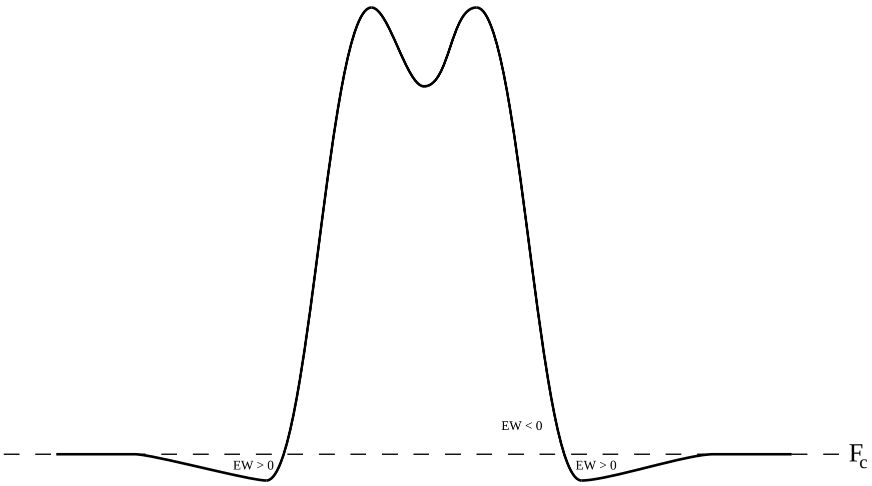

FIGURE 7.2: Schematic Hα profile that does not completely fill in the underlying absorption line. The continuum level (F_c) is indicated with a *dashed line.* The total EW of the line consists of a negative component, defined as the total flux above F_c, and the positive component(s), defined as the total absorbed flux below F_c.

have Hα emission lines that do not completely fill in the underlying absorption lines. Because we are interested in an EW that accounts for both the emission and the absorption components, we use our own spectroscopic observations of η Tau and β CMi and calculate the EW using

$$\mathrm{W}_{\mathrm{H}_\alpha} = \int \frac{F_\mathrm{c} - F(\lambda)}{F_\mathrm{c}}\,\mathrm{d}\lambda, \tag{7.1}$$

where F_c is the mean continuum flux level. The integral in the above equation extends over the entire spectral region where the absorption and the emission components are present, and therefore results in an EW that represents the absorption component (through a positive contribution to EW) and the emission component (through a negative contribution to EW). Both components are schematically illustrated in Figure 7.2. For the Hα profiles of η Tau and β CMi shown in Figure 7.1 we obtain an EW of -0.426 and -0.334 nm, respectively.

γ Cas and ζ Tau

Both γ Cas and ζ Tau are known to show complex variations in their Hα emission profiles on time scales from months to years, but in both cases the variations at the longer time-scales are always more significant. Furthermore, because the EW measure is an integrated quantity it has the tendency to be insensitive to the small scale variations in the line profile, typically seen at the shortest time-scales. Therefore we are only interested in the changes in the EW of Hα on the time scales of years.

In the case of γ Cas the spectroscopic observations conducted by Banerjee et al. (2000) are the closest in time to our interferometric observations that were collected between 1997 and 1998 (recall Table 3.1). Banerjee et al. (2000) reports Hα EW of -2.25 nm at the end of 1998, and -2.67 nm for observations obtained a year later. These values are consistent with EW of -2.57 nm we derive for the Hα profile from 2003 (recall Fig. 7.1). We conclude that the Hα emission of γ Cas is variable at the level of $\sim$20% on time scale of a year, but because the observations of Banerjee et al. (2000) from 1998 were acquired only one month after our 1998 interferometric observations, we use their reported EW of Hα as the corresponding emission measure for our observations.

The interferometric observations of ζ Tau that we have analyzed in Chapter 4 were obtained on 1999 March 1. Once again, the Hα observations by Banerjee et al. (2000) conducted on 1999 March 16 are the closest in time to our observations. Because the Hα profile variations on times-scales of days are very small in ζ Tau (Hanuschik et al., 1996), the EW of -2.06 nm reported by Banerjee et al. (2000) is very suitable for our analysis. It is also interesting to note that this value is effectively the same as the EW of -2.09 nm we obtain for the profile shown in Figure 7.1.

ϕ Per, ψ Per, and 48 Per

By comparing the Hα profiles of ϕ Per, ψ Per, and 48 Per from 1980 (Andrillat & Fehrenbach, 1982), 1989 (Slettebak, Collins, & Truax, 1992), 1993 (Hummel & Vrancken, 1995), and 1998–2000 (Banerjee et al., 2000), we conclude that only ϕ Per has significantly varying Hα emission, but even in that case the main variation is a gradual weakening of the emission over many years. Since the Mark III observations of the above stars date back to 1992, we use the EW of Hα reported by Hummel & Vrancken (1995), who observed these stars in 1993. The three stars, ϕ Per, ψ Per, and 48 Per, have reported equivalent widths of -3.50, -3.37, and -2.23 nm, respectively.

7.3 The Analysis

7.3.1 Physical Extent of a Circumstellar Region

Distance has a direct effect on the angular size, and, therefore, the angular measurements of the major axes of the circumstellar regions need to be either transformed into physical sizes (if the distances are known) or normalized with respect to the angular diameters of the central stars (which must be estimated since they have not been measured directly). The latter method was used by Quirrenbach et al. (1997), and, although it does eliminate the dependence on distance, it does introduce a dependence on the size of the central star. Because we have a range of spectral types, this approach is definitely not optimal.

A much better approach is to use the known distances to obtain directly the physical extent of each region. We use the observed Hipparcos parallax (π) to derive the corresponding distance (d) to each star. This in turn allows us to convert the best-fit value for the angular size of the major axis of the elliptical Gaussian model into a corresponding size in meters. Table 7.1 lists the angular size of the major axis ($\theta_{\rm mj}$) of each Hα-emitting region, the corresponding physical size in meters ($D_{\rm mj}$), along with the Hipparcos data used to calculate the distance to each star.

7.3.2 The Net Hα Emission

The equivalent widths of the Hα emission lines typically reported in the literature, only measure the amount of emission above the continuum level. Because we are dealing with B-type stars, whose underlying photospheric spectra are known to possess significant Hα absorption profiles, we need to correct for the "filling-in" effect of the absorption line. In our approach we assume that the entire absorption line is filled in by the superimposed emission. This is a good approximation for the sources considered here, where the Hα emission lines are stronger and wider than the underlying absorption lines. Even in the case of η Tau and β CMi, where the absorption lines are not completely filled in (recall Fig. 7.1), the above assumption can still be applied, because our EW measure of the emission, as defined through equation (7.1), is already reduced by the amount the absorption line is not filled in.

To obtain an estimate on the EW of the absorption line, we follow the procedure developed by Coté & Waters (1987), who modeled the relationship between the EW of the Hα absorption line and the intrinsic $(B-V)_0$ color index for normal main sequence B-type stars. This can be done because in the case of B-type stars the strength of the Hα absorption line is known to increase with later spectral type and it is at a maximum for early A-type stars. We should also note that for stars in our sample that are not on the main sequence, the equivalent widths of the absorption lines derived using the above method will be slightly overestimated (by not more than 0.1 nm). Because this is at the same level as the intrinsic scatter observed in the

TABLE 7.2: PHOTOMETRIC DATA FOR BE STARS

Star (1)	V (2)	$B-V$ (3)	$(B-V)_0$ (4)	$E(B-V)$ (5)	$V-R$ (6)	$E(V-R)$ (7)	R_0 (8)
γ Cas	2.47	−0.15	−0.30	0.07	0.07	0.06	2.24
η Tau	2.87	−0.09	−0.12	0.03*	0.03	0.02	2.77
ζ Tau	3.00	−0.19	−0.18	0.05	−0.03	0.04	2.91
β CMi	2.90	−0.09	−0.11	0.02*	−0.01	0.02	2.86
ϕ Per	4.07	−0.04	−0.24	0.11	0.16	0.09	3.65
ψ Per	4.23	−0.06	−0.16	0.10	0.10	0.08	3.89
48 Per	4.04	−0.03	−0.20	0.17	0.12	0.13	3.52

NOTE.— Columns 2 and 3: The apparent V magnitude and $B-V$ color from the BSC. Column 4: Intrinsic $(B-V)_0$ color based on the spectral type (FitzGerald, 1970). Column 5: $E(B-V)$ based on the absorption bump at 2200 Å (Beeckmans & Hubert-Delplace, 1980), except where denoted by * for values obtained from the estimated $(B-V)_0$ color. Column 6: $V-R$ colors from Johnson et al. (1966). Column 7: $E(V-R)$ derived from $E(V-R)/E(B-V) = 0.78 \pm 0.02$ (Schultz & Wiemer, 1975). Column 8: Absolute R magnitude corrected for interstellar extinction.

Hα equivalent widths for stars of the same spectral type (see, for example, Fig. 1 in Coté & Waters, 1987), we neglect this overestimation in our analysis.

In Table 7.2 we list the observed $B-V$ colors from the BSC for each of the stars. Deriving the intrinsic $(B-V)_0$ color of the central star from the observed $B-V$ value is not trivial, even if the corrections for the interstellar extinction are known, because Be stars can still appear intrinsically redder than normal B-type stars of the same spectral type. This is typically attributed to free-bound and free-free emission, as well as a possible circumstellar reddening (Schild, 1978). For this reason we estimate the $(B-V)_0$ index based on the spectral type and not on the observed $B-V$ color. Table 7.2 lists the $(B-V)_0$ values based on the tabulation of FitzGerald (1970) which in turn is used to calculate the equivalent widths of the Hα absorption lines (via eq. 6 of Coté & Waters, 1987). These values are then combined with the equivalent widths of the observed Hα emission lines ($W_{\mathrm{H}\alpha}$) to give a measure of the net Hα emission ($E_{\mathrm{H}\alpha}$) from each circumstellar region (both quantities are listed in Table 7.4).

7.3.3 The Hα Luminosity

The net Hα emission derived in previous section, although corrected for the "filling-in" effect of the absorption line, is still measured with respect to the underlying stellar photosphere. Because we are dealing with spectral classes ranging from B0 to B8, we need to account for the different continuum flux levels. We use two independent methods to estimate the stellar continuum level. One method is based on the photometry and thus requires us to account for the different distances to the sources. The other method, which is distance independent, uses model energy distributions to represent the underlying stellar continuum. Because the second method does not account for the continuum emission from the circumstellar region, as well as requires the stellar radius to be known, it is only used to verify the photometrically derived results.

Determining Hα Luminosity based on the Photometry

Obtaining the flux levels of the individual stars from photometry is complicated by the interstellar extinction. Using the observed $B-V$ color and the estimated intrinsic $(B-V)_0$ color based on the spectral type, we can derive the color excess $E(B-V)$. This approach should work for the later type Be stars, but will tend to overestimate the color excess (by possibly as much as 0.15 mag) for spectral types B3e and earlier, because of the intrinsic reddening due to the free-bound and free-free emission from the circumstellar envelope (Schild, 1978, 1983). Fortunately, there are other methods that can be used to estimate the color excess due to the interstellar extinction. For example, Beeckmans & Hubert-Delplace (1980) used the depth of the interstellar absorption bump at 2200 Å to derive the values of $E(B-V)$ for Be stars. In Table 7.2 we list the values of $E(B-V)$ reported by Beeckmans & Hubert-Delplace (1980) for all but two of our stars. The two missing Be stars are η Tau and β CMi, and because these stars have the latest spectral type, as well as are the closest, we simply derive an estimate of $E(B-V)$ based on their observed $B-V$ colors and the intrinsic $(B-V)_0$ colors derived from the spectral type.

With a known color excess $E(B-V)$ we can correct the apparent V magnitude of each star for interstellar extinction using:

$$V_0 = V - A_V = V - R_V \cdot E(B-V), \tag{7.2}$$

where $R_V \equiv A_V/E(B-V)$ and is known as the reddening constant. The typical value of R_V representative of interstellar extinction in our Galaxy was shown by Schultz & Wiemer (1975) to be 3.14±0.10. Similarly, the observed $V-R$ colors (see Table 7.2) can be corrected for interstellar reddening using the ratio of $E(V-R)/E(B-V) = 0.78 \pm 0.02$ derived by Schultz & Wiemer (1975), and in turn the R_0 magnitudes can be obtained. The R-band has an effective central wavelength of ~658 nm and a FWHM of ~138 nm, and thus to within a

TABLE 7.3: ESTIMATED STELLAR PROPERTIES

Star	$f_\star$ (erg/s/m^2/nm)	$4\pi d^2 f_\star$ (10^{32} erg/s/nm)	$T_{\rm eff}$ (K) ±5%	$R_\star$ ($R_\odot$)	$4\pi R_\star^2 \mathcal{F}_\star^{\rm S}$ (10^{32} erg/s/nm)
γ Cas	2.71×10^{-5}	114^{+27}_{-22}	31,000	8 ± 2	97 ± 50
η Tau	1.65×10^{-5}	$25.2^{+6.3}_{-5.1}$	12,400	5 ± 1	8.60 ± 3.5
ζ Tau	1.45×10^{-5}	$28.4^{+8.5}_{-6.5}$	16,400	6 ± 1	18.8 ± 6.6
β CMi	1.52×10^{-5}	$4.95^{+0.46}_{-0.42}$	12,000	3.6 ± 0.3	4.14 ± 0.81
ϕ Per	7.35×10^{-6}	42.5^{+17}_{-12}	21,500	6.0 ± 0.2	28.5 ± 3.4
ψ Per	5.87×10^{-6}	$32.4^{+12}_{-8.8}$	15,400	4.7 ± 0.3	10.5 ± 1.7
48 Per	8.30×10^{-6}	$28.6^{+8.0}_{-6.2}$	19,000	5.1 ± 0.1	16.9 ± 1.8

NOTE.— $f_\star$ is the physical flux (surface brightness) and $4\pi d^2 f_\star$ (where d is the distance to the source from Table 7.1) is the corresponding total radiation in the Hα region based on photometric data from Table 7.2. The effective temperature ($T_{\rm eff}$) and the stellar radius ($R_\star$) are based on the spectral type and tabulations of Böhm-Vitense (1981) and Underhill et al. (1979), respectively.

good approximation the R_0 magnitude can be used to measure the continuum flux level in the Hα region. Also, the relatively large spectral width of the R-band allows us to neglect the contribution of the Hα emission to R_0.

To convert a R_0 magnitude into a corresponding flux above Earth's atmosphere ($f_\star$) we use

$$f_\star = f_{\rm s} 10^{-0.4(R_\star - R_{\rm s})}, \tag{7.3}$$

where $f_{\rm s}$ and $R_{\rm s}$ are the mean flux density (in the R-band) and the R magnitude of a standard star, respectively. Because we are interested in the functional dependence of the net Hα emission on the disk size, the actual value of $f_{\rm s}$ is not important. Nevertheless, in order to work with values that have physically meaningful units we use a *representative* value for the absolute flux density of $f_{\rm s} = 1.76 \times 10^{-4}$ erg s^{-1}m^{-2}nm^{-1} defined for a standard star with $R_{\rm s} = 0$ (Johnson, 1966). The values for $f_\star$ based on the R_0 magnitudes are listed in Table 7.3, along with the corresponding *total* radiation at Hα ($4\pi d^2 f_\star$).

Finally to work with a Hα emission measure that is independent of distance we multiply the net Hα emission, $E_{\rm H\alpha}$, derived in previous section, by the total radiation in the Hα region, to obtain

$$L_{\rm H\alpha} = 4\pi d^2 f_\star E_{\rm H\alpha}, \tag{7.4}$$

which we refer to as the Hα luminosity. The values for the Hα luminosities are given in Table 7.4 along with their corresponding uncertainties, which account for the errors in the distance determination (largest source of uncertainty), photometry, and the Hα equivalent

TABLE 7.4: THE Hα EMISSION OF BE STARS

Star	$W_{\mathrm{H}\alpha}$ (nm)	$E_{\mathrm{H}\alpha}$ (nm)	$L_{\mathrm{H}\alpha}$ (10^{32} erg/s)	$L^{\mathrm{S}}_{\mathrm{H}\alpha}$ (10^{32} erg/s)
γ Cas	-2.25 ± 0.11	-2.51 ± 0.12	287^{+69}_{-56}	250 ± 130
η Tau	-0.426 ± 0.021	-1.02 ± 0.03	$25.6^{+6.5}_{-5.2}$	8.7 ± 3.6
ζ Tau	-2.06 ± 0.10	-2.55 ± 0.11	72.2^{+22}_{-17}	48 ± 17
β CMi	-0.334 ± 0.017	-0.942 ± 0.026	$4.66^{+0.45}_{-0.42}$	3.90 ± 0.77
ϕ Per	-3.50 ± 0.18	-3.87 ± 0.18	165^{+65}_{-47}	110 ± 14
ψ Per	-3.37 ± 0.17	-3.89 ± 0.17	126^{+47}_{-35}	40.8 ± 6.9
48 Per	-2.23 ± 0.11	-2.68 ± 0.12	77^{+22}_{-17}	45.3 ± 5.2

NOTE.— The Hα equivalent widths ($W_{\mathrm{H}\alpha}$) are taken from a number of different sources (see § 7.2.2) and their uncertainties are assumed to be at 5% level to account for observational errors as well as possible intrinsic variability.

widths, but do not include the uncertainty associated with the determination of the absolute flux density of a standard star.

Determining Hα Luminosity based on the Synthetic Spectra

Instead of using photometry to derive the stellar continuum flux level in the Hα region, we can use synthetic spectra calculated for atmospheric models of varying effective temperatures. For this purpose we have used the well known grid of stellar atmosphere model spectra computed using the ATLAS9 program (Kurucz, 1993). The models were chosen to have effective temperatures that were the same as, or as close to those estimated based on the spectral type (see Table 7.3). Because the grid covered the range of the effective temperatures in approximately 500 and 1,000 K steps, for some stars it was necessary to interpolate the fluxes in effective temperature. All models correspond to solar abundances, $\log g$ of 4 (for luminosity class V or IV) and 3.5 (for luminosity class of III), although little variation between the two gravities is present, and the standard microturbulence of 2 km s^{-1} was used. Figure 7.3 illustrates a sample of the physical flux ($\mathcal{F}_\star$) as a function of wavelength obtained for a 12,000 K model.

We also need to account for the surface area of each star to estimate the total stellar radiation from the physical flux in the Hα region. The radius of each star was estimated based on its spectral type (Underhill et al., 1979), and the resulting synthetic total radiation in the Hα region ($4\pi R_\star^2 \mathcal{F}_\star^{\mathrm{S}}$) is given in Table 7.3. It is evident from the table that the synthetic values are systematically smaller than the photometrically derived ones, and this should be expected

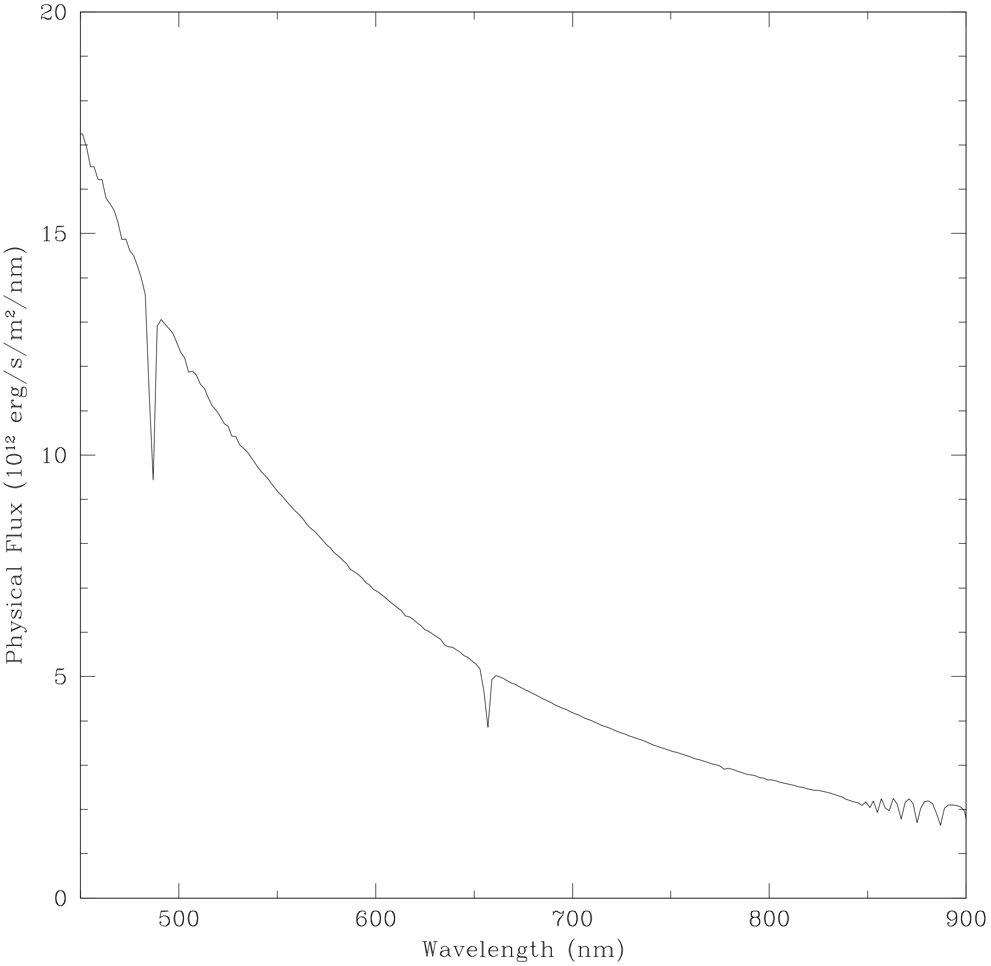

FIGURE 7.3: Synthetic energy distribution for $T_{\text{eff}} = 12000$ K and $\log g = 4.0$.

because the synthetic spectra do not account for the bound-free and free-free emission from the circumstellar material. Although there does exist a general correlation between the net Hα emission and IR excess, a large intrinsic scatter is also observed between different sources, and therefore it is not trivial to account for this extra emission (Coté & Waters, 1987; van Kerkwijk, Waters, & Marlborough, 1995). For the purpose of the analysis presented here we are only interested in the synthetic continuum level as a check for the photometrically derived values and thus we neglect the continuum emission in the synthetic spectra. Taking the same approach as in equation (7.4) we can calculate a synthetic Hα luminosity using

$$L^{\mathrm{S}}_{\mathrm{H}\alpha} = 4\pi R_{\star}^{2} \mathcal{F}_{\star}^{\mathrm{S}} E_{\mathrm{H}\alpha}, \tag{7.5}$$

where $E_{\mathrm{H}\alpha}$ is the net Hα emission discussed in § 7.3.2. The $L^{\mathrm{S}}_{\mathrm{H}\alpha}$ values for all seven stars are listed in table 7.4.

7.4 Discussion

7.4.1 The Hα Emission as a Tracer of the Circumstellar Disk

We begin by looking at the relationship between the Hα emission and the physical extent of the circumstellar region. Using the values for the Hα luminosity from Table 7.4 and the physical size of the major axis from Table 7.1, we construct a corresponding log-log plot of $L_{\mathrm{H}\alpha}$ versus D_{mj} in Figure 7.4. We obtain a Pearson correlation coefficient of 0.98 and thus a definite correlation between the parameters exists. Fitting a line to the data in the log-log plot yields a slope of 2.12±0.24 and a χ^2_ν of 0.75.

The above result suggests that the emission is proportional to the area of the Hα emitting region independently of the different inclination angles these systems are viewed at (although the range of possible inclination angles represented by our small sample of stars is not that large). If the circumstellar region is optically thin to Hα emission then this might simply mean that the *emission measure*[1] of the disk, which is proportional to the emitting volume, scales as the surface area of the emitting region. However, the study of energetics of Be star envelopes by Millar, Sigut, & Marlborough (2000) shows that the Hα emission originating in the equatorial plane of the circumstellar disk, especially close to the central star (for $r < 15R_{\star}$),

---

[1] Because the Hα emission is created by recombinations, the total emission in the optically thin case is proportional to the volume integrated squared electron number density, i.e. $\int N_{\mathrm{e}}^{2} \mathrm{d}V$, which is also known as the emission measure (see, for example, Millar, Sigut, & Marlborough, 2000).

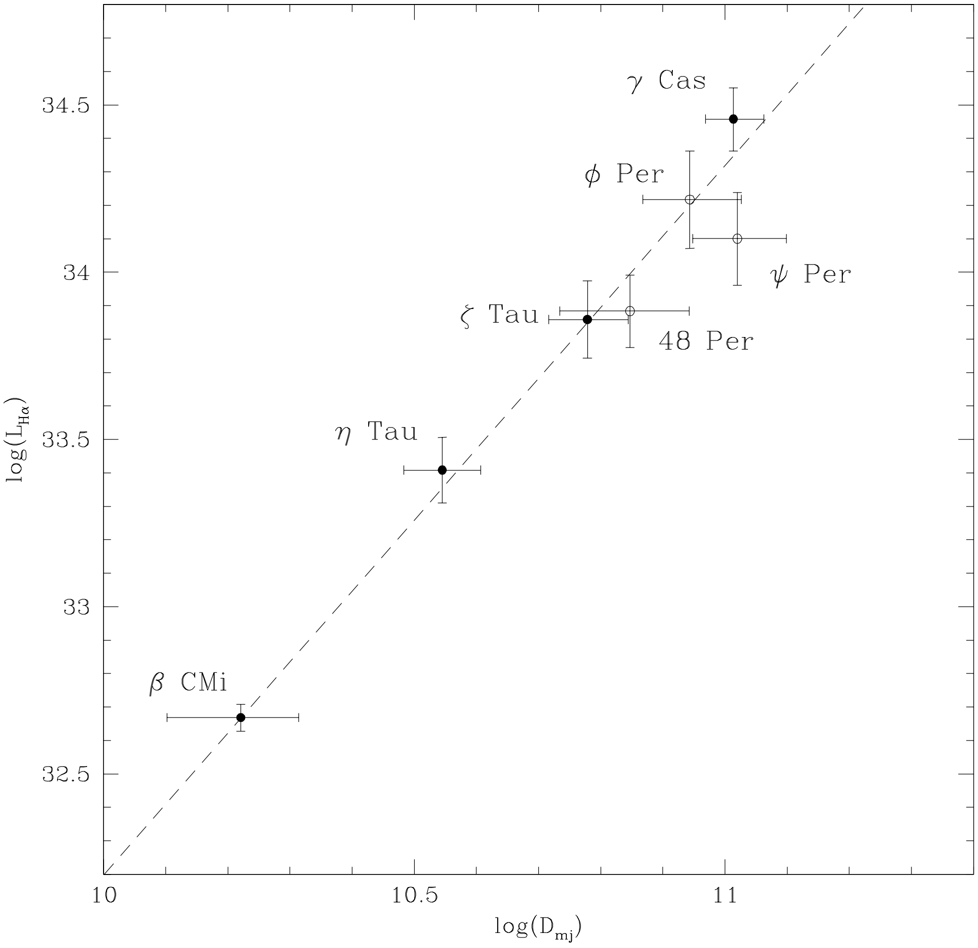

FIGURE 7.4: The Hα luminosity (in erg s^{-1}) as a function of the size (in meters) of the major axis of the disk. The circumstellar envelopes that have been resolved by the Mark III interferometer (Quirrenbach et al., 1997) are marked with *open circles*. A linear fit in the log-log plot produces a best-fit slope of 2.12±0.24 (*dashed line*).

is optically thick. Because this is the same region that is responsible for the majority of the line emission, and if the disk has a constant surface brightness, then the Hα luminosity will be proportional to the effective surface area of the circumstellar disk.

If we assume that the circumstellar region is a geometrically thin axisymmetric disk, then the axial ratio, r, we have obtained from the elliptical Gaussian model can be used to estimate the inclination angle i between the direction perpendicular to the plane of the disk and the line of sight (i.e., $r \sim \cos i$). Because the effective area of a disk viewed at an angle i can be expressed as $A \cos i$ where A is the surface area, and if the Hα luminosity is proportional to the effective area, dividing $L_{\mathrm{H}\alpha}$ by r should remove any dependence on the inclination angle. Figure 7.5 shows the relationship between $L_{\mathrm{H}\alpha}/r$ and D_{mj} where again a clear trend is visible. The correlation coefficient remains high at 0.96 and the best-fit line has a slope of 2.24 ± 0.26 and χ^2_ν of 1.19. Based on this result we conclude that the Hα luminosity (corrected for the projection effect) is consistent with an optically thick emission from a geometrically thin disk of a relatively constant surface brightness.

Optically thick disks with no temperature gradients will have a constant surface brightness as a function of radius. Although actual disks will have a range of temperatures, assigning a constant temperature to the Hα-emitting region might be appropriate. This is because Millar & Marlborough (1999c), who, by considering the rates of energy gain and loss in the disks of four Be stars (including γ Cas, ψ Per, and β CMi), have shown that the disk temperature in the equatorial plane is fairly constant as a function of radial distance, especially in the regions close to the central star (i.e., where the majority of the Hα flux is expected to originate). Furthermore, our results suggest that the surface brightness in the Hα-emitting region is not only constant as a function of radial distance, but that it does not vary significantly for stars of different effective temperatures. This is somewhat surprising considering that the disk models of Millar & Marlborough (1999c) for stars of different effective temperatures do not have the same temperature profiles as function of radial distance, although in the inner part of the disks ($< 10R_\star$) the temperatures differences are not that great and are in the 3,000–5,000 K range (depending on the distance from the equatorial plane). It is also possible that because the Hα emission is optically thick in these inner regions (Millar, Sigut, & Marlborough, 2000), the similar surface brightnesses for disks with slightly different temperatures is a result of similar conditions in the envelopes where the optical depth is roughly unity (i.e., where most of the radiation comes from).

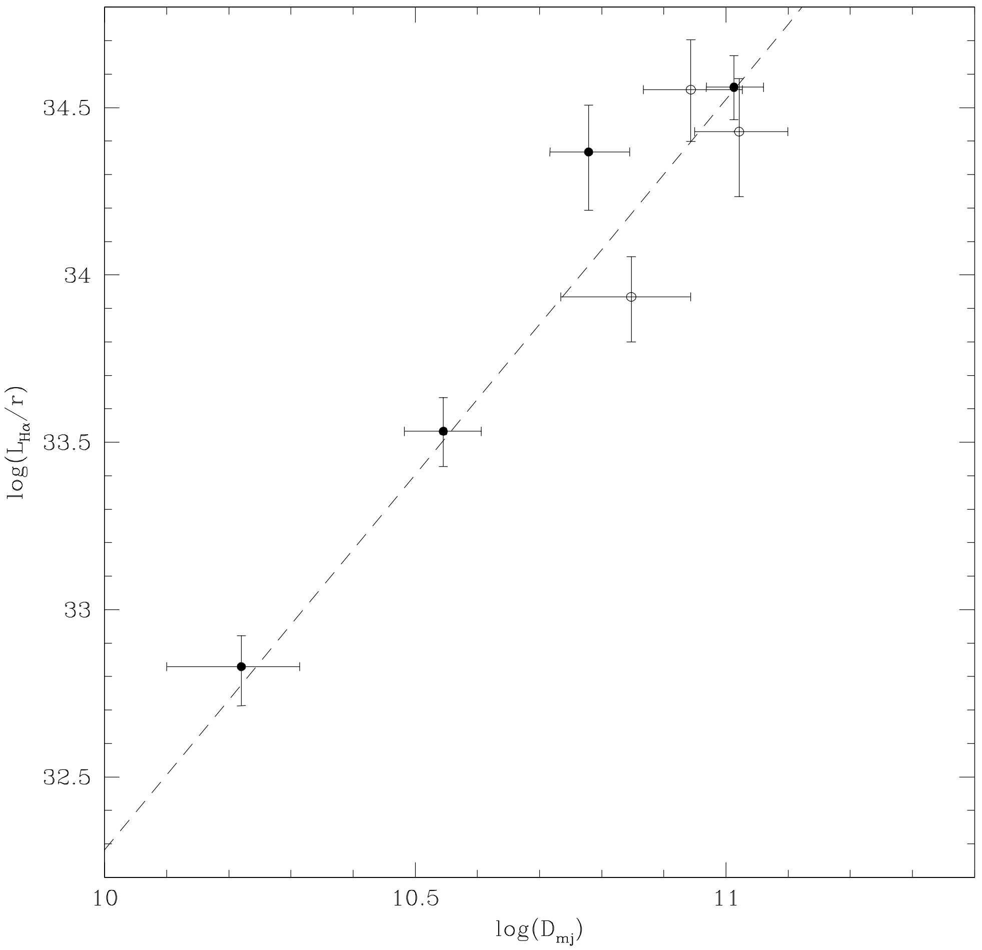

FIGURE 7.5: Same as Fig. 7.4, except that the Hα luminosity has been divided by the axial ratio r. A linear fit in the log-log plot produces a best-fit slope of 2.24±0.27 (*dashed line*).

Lastly, we need to verify that the visible trend in Figures 7.4 and 7.5 is not caused by the uncertainties in the distance alone. Both the physical size of the major axis, $D_{\rm mj}$, and the photometrically determined Hα luminosity, $L_{\rm H\alpha}$, depend on the distance, and any systematic errors in the distance will distribute the data along a diagonal line with a positive slope. To verify that the trend is not caused by such systematic errors, we plot the synthetic Hα luminosities, $L^{\rm S}_{\rm H\alpha}$ and $L^{\rm S}_{\rm H\alpha}/r$ versus $D_{\rm mj}$ in Figures 7.6 and 7.7, respectively. Because only the abscissa depends on the distance in this case, a trend can no longer be caused by uncertainties associated with the distance determination. Both relations yield best-fit slopes of 1.98±0.33 and 2.28±0.38, in complete agreement with our previously determined values. The χ^2_ν values for the relations based on the synthetic continuum levels are slightly larger (approximately twice as large) than before, but this might be solely related to the larger systematic uncertainties associated with the radii estimates, as well as with the fact that the synthetic spectra do not account for the continuum emission from the circumstellar regions. In any case, we conclude that the relationship between the Hα luminosity and the physical extent of the circumstellar region seen in Figures 7.4 and 7.5 is not caused by the errors in the distance.

7.4.2 Disk Size and Stellar Properties

Size versus Spectral Type

The origin of the circumstellar regions around Be stars is still debated. One of the simpler tests is to search for a possible correlations between the size of the circumstellar region and the spectral type of the central star. Figure 7.8 illustrates the relationship between the physical extent of the major axis and the spectral type for the seven stars listed in Table 7.1. Within our small sample of stars, it appears that the size of the Hα emitting region decreases toward later spectral type. This is also shown in Figure 7.9, which plots $D_{\rm mj}$ versus the effective temperatures from Table 7.3. The visible correlation is not nearly as strong as the one found for the Hα emission and the size of the emitting region, but it still yields a correlation coefficient of 0.75 and a slope of 1.29±0.19. Unfortunately, the small number statistics make these results tentative, but with future observations of a larger set of stars, it will be possible to explore this relationship further.

If the apparent dependence of $D_{\rm mj}$ on the spectral type is real, it is possible that this is due to the tendency of hotter stars to have physically larger circumstellar regions, but equivalently

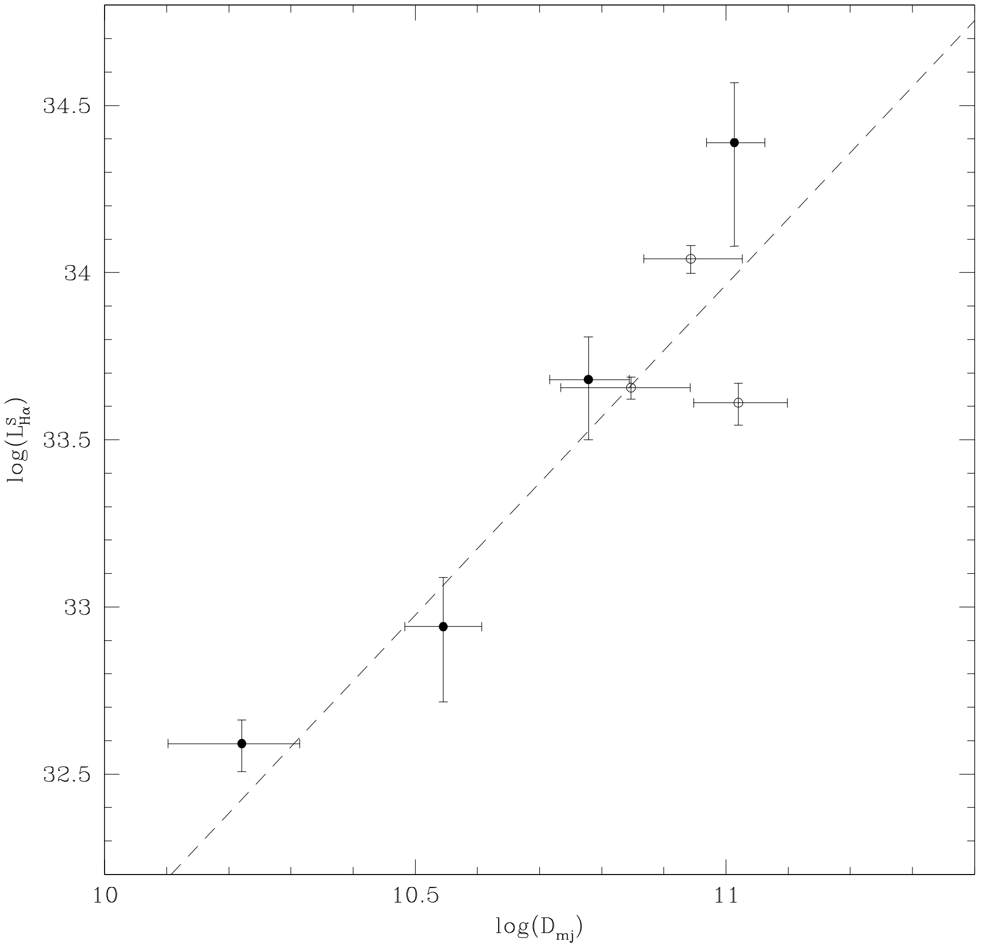

FIGURE 7.6: Same as Fig. 7.4, except that the Hα luminosity has been calculated with respect to a synthetic continuum level. A linear fit in the log-log plot produces a best-fit slope of 1.98±0.33 (*dashed line*).

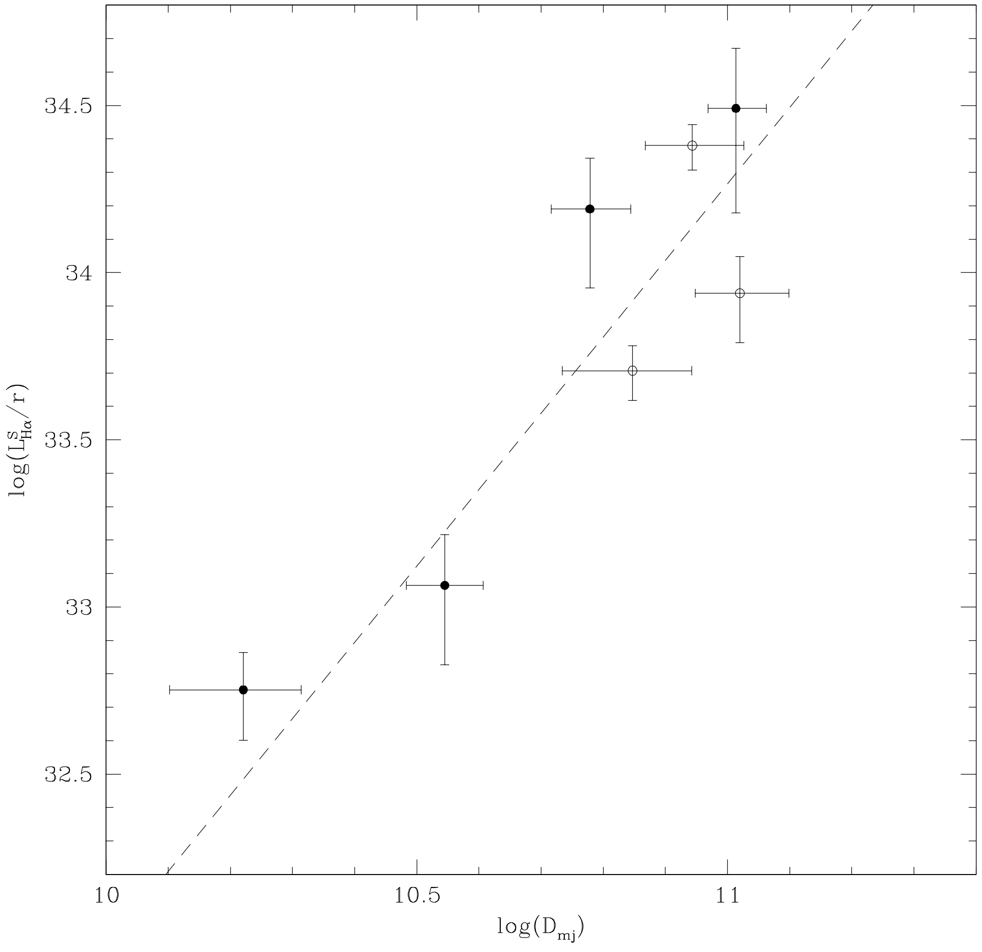

FIGURE 7.7: Same as Fig. 7.5, except that the Hα luminosity has been calculated with respect to a synthetic continuum level. A linear fit in the log-log plot produces a best-fit slope of 2.28±0.38 (*dashed line*).

Table 7.5: Rotational Velocities of Be Stars

Star	$v \sin i$ (km s^{-1})	$v_{\rm est}$ (km s^{-1})	$v_{\rm crit}$ (km s^{-1})	$v_{\rm est}/v_{\rm crit}$
γ Cas	230±23	375±40	538±54	0.70±0.10
η Tau	140±14	212±28	406±41	0.53±0.09
ζ Tau	220±22	231±28	441±44	0.52±0.08
β CMi	245±25	338±75	397±40	0.85±0.21
ϕ Per	400±40	450±46	477±48	0.94±0.14
ψ Per	280±28	317±38	428±43	0.74±0.12
48 Per	200±20	$\gtrsim 308$	458±46	$\gtrsim 0.67$

Note.— The $v \sin i$ values are from Slettebak (1982), and $v_{\rm crit}$ values are from Porter (1996).

this can also be attributed to a simple ionization effect. For example, Millar & Marlborough (1999a) considered the rates of energy gain and loss in the circumstellar regions of Be stars and concluded that, in the case of the hot Be star γ Cas, the circumstellar envelope is almost completely ionized, in contrast to the cool Be stars (like β CMi), whose envelopes in and near the equatorial plane (where most of the emission normally originates) is mostly neutral (see also Millar & Marlborough, 1998, 1999b). This suggests that the smaller Hα-emitting regions of the cooler Be stars are a result of an ionization bounded conditions in the circumstellar regions and not due to physically smaller regions.

Size versus Rotational Velocity

Another commonly examined relationship is the one between the size of the region and the rotational velocity. The connection between the two would be expected if rotation has a direct effect on the disk formation, as originally suggested by Struve (1931). In Table 7.5 we list the $v \sin i$ values from Slettebak (1982), the estimated[2] rotational velocities ($v_{\rm est}$), along with the critical velocities from Porter (1996). We find no correlation between the physical extent of the Hα emitting region and the observed $v \sin i$ value. This is in agreement with with previous studies that concluded that there is no correlation between the strength of the Hα emission and the $v \sin i$ value. There does appear to be a weak correlation (with correlation coefficient of 0.74) between the critical velocity and the size of the region (see Fig. 7.10), but this is expected based on the relationship we have seen between the size of the disk and the spectral type.

---

[2] The rotational velocity is estimated by assuming that the circumstellar envelope is a thin axisymmetric disk that is aligned with the stellar equator, in which case the axial ratio, r, can be used to estimate i.

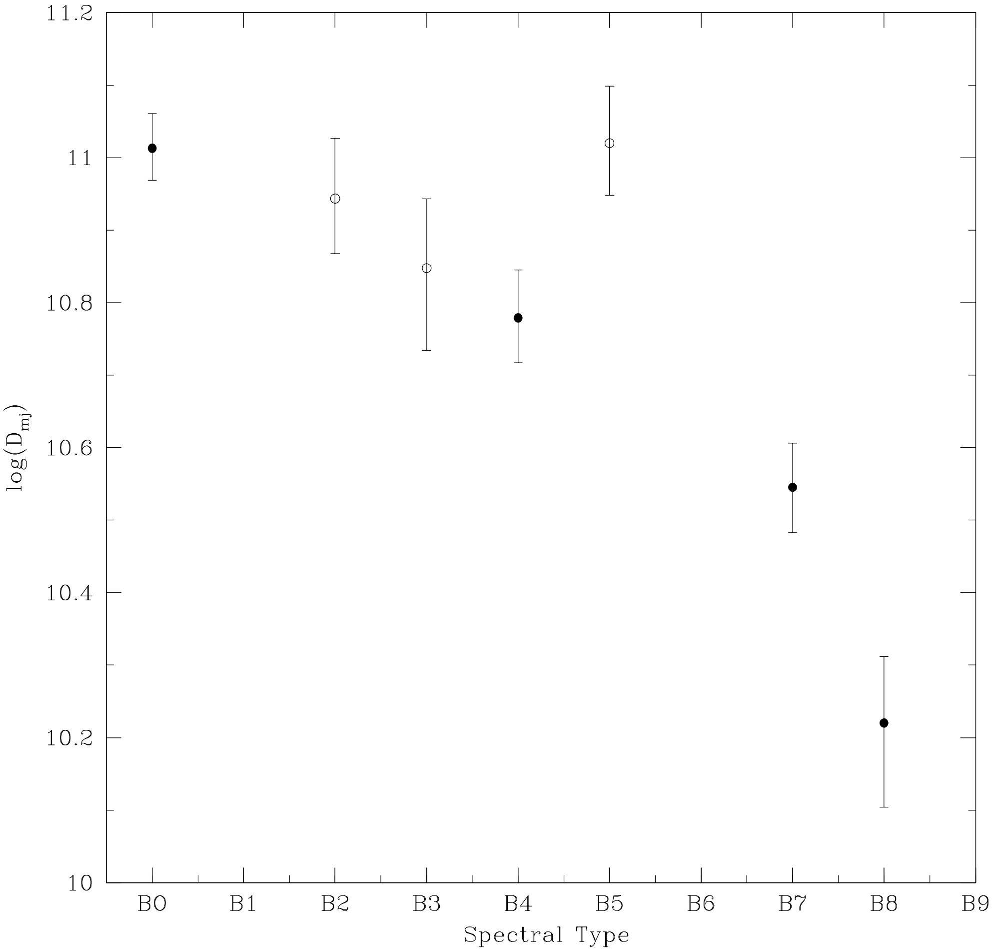

FIGURE 7.8: The size of the major axis of the disk as a function of the spectral type.

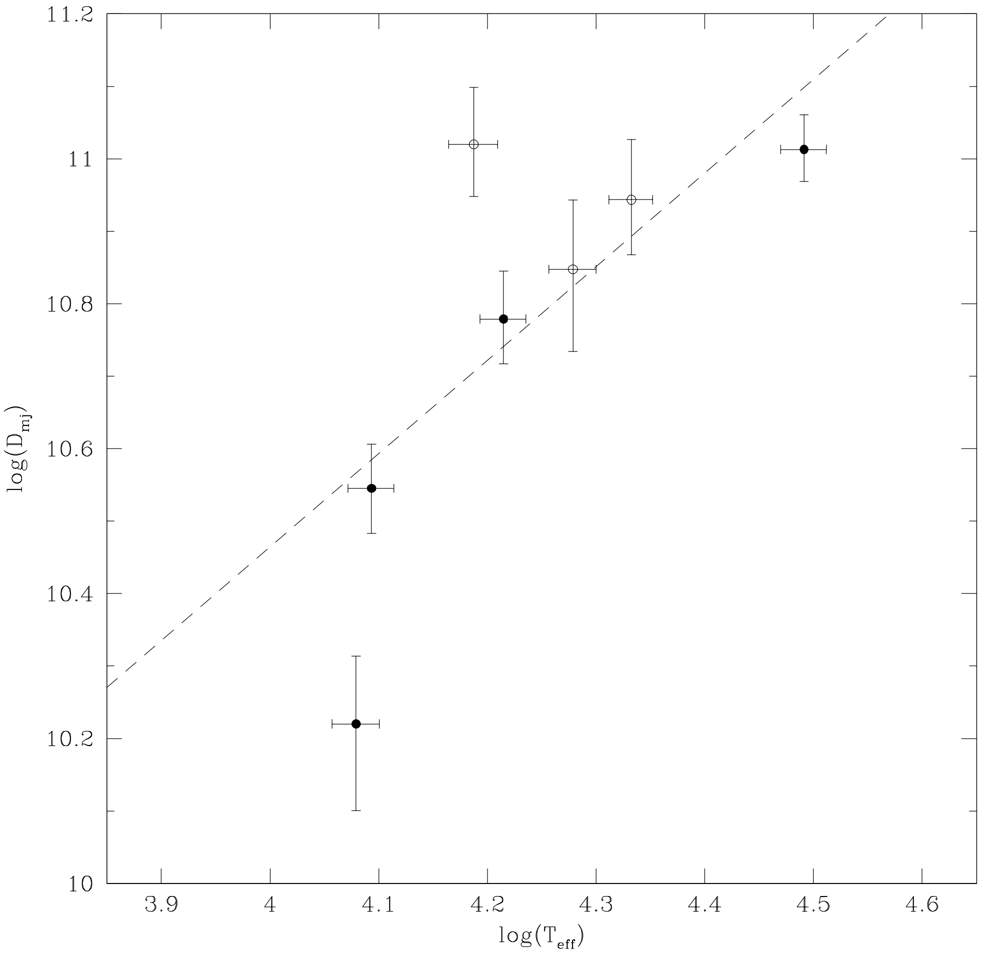

FIGURE 7.9: The size of the major axis of the disk as a function of the effective temperature of the central star.

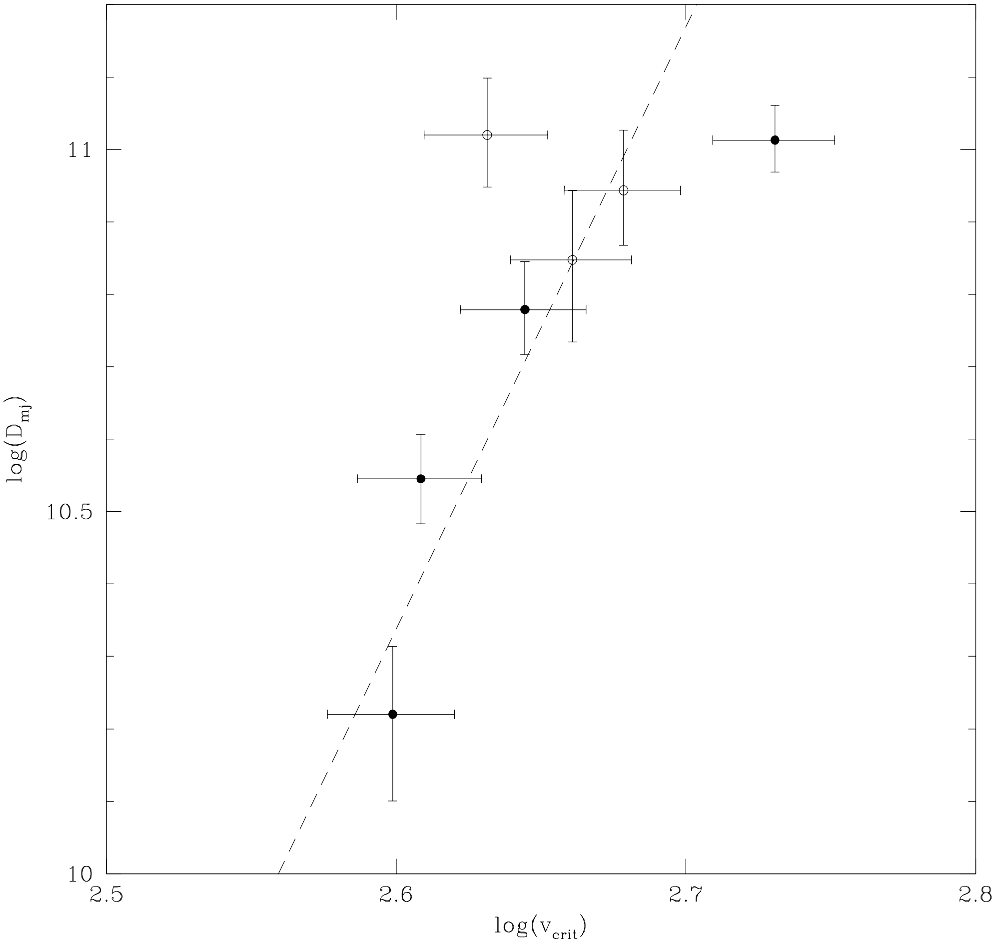

FIGURE 7.10: The the size of the major axis of the disk as a function of the critical rotational velocity.

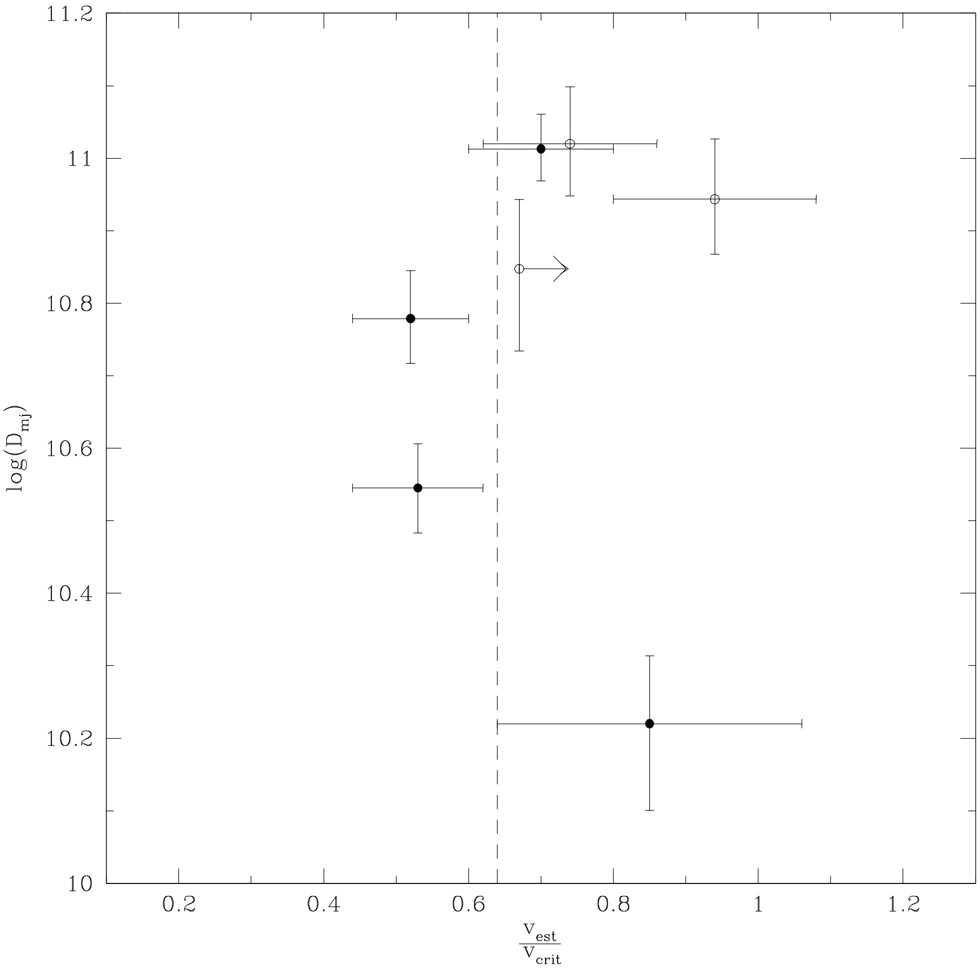

FIGURE 7.11: The the size of the major axis of the disk as a function of the estimated rotational velocity (in units of critical velocity). The weighted average value of $v_{\rm est}/v_{\rm crit}$ is shown with *dashed line.*

Because we derive an inclination angle i from the apparent ellipticity of the Hα-emitting disk, our estimates on the rotational velocities of Be stars are quite independent of the estimates that are obtained for systems that are thought to be viewed edge-on (i.e., using Be-shell stars). Therefore our estimate on the average rotational velocity, expressed as a fraction of $v_{\rm crit}$, should be independent of similar estimates obtained from observations Be-shell stars. In Table 7.5 we list the values of the ratio of $v_{\rm est}$ to $v_{\rm crit}$ for all stars, including 48 Per for which only a lower limit can be obtained (see also Fig. 7.11). We obtain a weighted average (excluding 48 Per) of 0.64±0.14 for $v_{\rm est}/v_{\rm crit}$, which is in excellent agreement with the work of Porter (1996), who concluded that the distribution of the rotational velocities is sharply peaked at $\sim 0.7 v_{\rm crit}$.

Assuming that the $v \sin i$ values obtained from spectral lines are not underestimated (for example due to the equatorial gravity darkening caused by rapid rotation), the above result suggests that Be stars are rotating well below their critical limits. On the other hand, if the $v \sin i$ values are systematically underestimated by tens of percent (as suggested by Townsend, Owocki, & Howarth, 2004), then it is still possible that these stars have near-critical rotation rates. A much more direct method for determining the rotational velocity of stars is the observation of the rotationally induced distortion of the stellar photosphere by long-baseline interferometry. In fact, the first results suggesting near-critical rotation of Be stars already exist (Domiciano de Souza et al., 2003). It is anticipated that with the advent of optical interferometric observations at baselines of hundreds of meters (such as those of the NPOI), further observational constraints on the stellar rotation and its role in Be disk formation will be possible.

Chapter 8

Conclusions

8.1 Internal Calibration of Optical Interferometric Data

We have developed a new method for calibrating optical interferometric observations, which in combination with the multi-channel capability of the NPOI allows the calibration of the squared visibilities without the need of an external calibrator. Even if the calibration with respect to an external calibrator is performed, the new method can still improve the quality of the data by an order of magnitude. The new calibration method is especially useful in the context of observations of Be stars, where the Hα emission from the circumstellar environment is restricted to only one or two spectral channels. In fact, in the case where the Hα emission is relatively weak, the internal calibration can make an observational data set that was previously unusable (due to large systematic errors) as good as the best interferometric data sets seen in the literature.

We have successfully calibrated observations of four Be stars with a range of different Hα emission equivalent widths. The observations of all four stars resulted in a detectable signature of a resolved circumstellar structure and in all cases the results appeared to be limited by the residuals resulting from the removal of the additive bias. Therefore, it appears that with a better handle on the systematic biases even higher precision calibration will be possible. Efforts on improving the bias estimation are currently being undertaken at the NPOI, and thus it is anticipated that in the very near future the effects of the additive bias should be eliminated or at least significantly suppressed.

The next step in developing the internal calibration technique is to extend its applicability to more general source structures, especially those which might not be point-symmetric. This will require modeling the effects of the atmosphere and the instrument as a function of wavelength, for both the visibility amplitude and the phase. This more general approach will also give an opportunity to calculate the *closure differential phase*, a rather new concept in optical interferometry first suggested by Monnier (2003b). Although the concept of *closure differential phase* is similar to the differential closure phase we have demonstrated in Chapter 3 (i.e., both methods require multi-channel capability), the former requires fewer assumptions about the source structure emitting at the continuum wavelengths. Therefore, a relatively simple extension of the calibration method presented in this dissertation will allow application to circumstellar regions around continuum sources that no longer have a simple (and predictable) structure.

8.2 The Circumstellar Envelopes of Be Stars

The four Be stars, γ Cas, ζ Tau, η Tau, and β CMi have been observed with the NPOI and their Hα emitting envelopes were modeled with elliptical Gaussians. By comparing our results with those already in the literature, we conclude that the model parameters describing the general characteristics of the circumstellar envelopes of all four stars are consistent with the results produced by other instruments. In fact, in some cases our results establish the first independent confirmation of the already published model parameters. In the case of ζ Tau we have also concluded that the circumstellar envelope surrounds only the primary component, and is well within its Roche lobe. Future interferometric observations of similar systems will put direct constraints on the models of disk truncation by the secondary, like the one simulated by Okazaki et al. (2002). We have also demonstrated how even a very limited set of closure phases can be used to deduce a signature of a non-point-symmetric source structure.

Our analysis of the relationship between the net Hα emission and the physical extent of the emitting circumstellar region produced some interesting results. A clear correlation between the two properties has been established for the first time, as well as the functional dependence between the parameters suggest that the emission is directly proportional to the effective surface area of the emitting disk. Our results are therefore consistent with an optically thick Hα emission from geometrically thin circumstellar disk. We also do not detect any significant degree of correlation between the size of the circumstellar region and stellar rotation rate. Within our small sample of stars it appears that hotter Be stars tend to have more extended

Hα-emitting regions. Extending our analysis to a larger sample of stars will verify if this is indeed a general property of classical Be stars.

8.3 Future Prospects

One of the more important recent achievements at the NPOI was the demonstration of the coherent combination of light from six separate telescopes (Hummel et al., 2003). This 6-way beam combination capability, combined with the reconfigurable array, gives an excellent Fourier (u,v)-plane coverage, which in turn yields more visibility and closure phase information than any other separate-element optical interferometer in operation today. The advent of the 6-way beam combination at the NPOI also coincided with the implementation of the reconfigurable stations on the imaging part of the array, which give access to much longer baselines. To date, observations have been already obtained at baselines of up to ~74 m, and thus this already represents an increase in spatial resolution of the instrument by approximately a factor of two, as compared to the observations presented in this dissertation.

Another useful instrumental capability that has been introduced recently, was the fabrication and testing of a specialized spectral filter, which can isolate Hα emission line in a single spectral channel. This will result in a much better contrast between the Hα emitting envelope and the stellar continuum, and thus will allow a more detailed and higher dynamic range modeling (or imaging) of select targets. In the future, the concept of narrowband interferometric observations can be extended to other emission lines, which are sensitive to the physical condition in other regions of the circumstellar disk.

Combining all of the new instrumental capabilities promises to bring a wealth of new and exciting observations. Because the formation of the circumstellar disks around Be stars is still one of the biggest unknowns, the interferometric investigations in the near-term will concentrate on detecting the small scale structures within the disk, as well as on constraining the spatial characteristics of the inner disk, thereby putting specific constraints on disk formation theories. For example, a detection of gaps or ring-like structures in the disk will exclude many models that do not predict a disk detachment from the stellar surface. Imaging smaller scale structures such as one-armed density waves or spiral structures will yield direct information about the instabilities in the disk, in some cases possibly in connection with the unseen binary companions. Also, combining spectroscopic and interferometric observations, especially in the context of mass ejection episodes (which in some cases might be predicted based on spectroscopy) will play a crucial role in our understanding of the mass-feeding mechanisms, and the subsequent evolution of the material in the disk. Lastly, the direct detection of the deviation from circular symmetry of the stellar surface, due to rapid rotation, will help establish the connection between the stellar rotation and the disk formation, independently of (or in conjunction with) spectroscopy.

Bibliography

Andrillat, Y. & Fehrenbach, C. 1982, A&AS, 48, 93

Armstrong, J. T., Mozurkewich, D., Rickard, L. J., Hutter, D. J., Benson, J. A., Bowers, P. F., Elias II, N. M., Hummel, C. A., Johnston, K. J., Buscher, D. F., Clark III, J. H., Ha, L., Ling, L.-C., White, N. M., & Simon, R. S. 1998, ApJ, 496, 550

Balona, L. A. 1995, MNRAS, 277, 1547

Banerjee, D. P. K., Rawat, S. D., & Janardhan, P. 2000, A&AS, 147, 229

Barnes, T. G., & Evans, D. S. 1976, MNRAS, 174, 489

Barnes, T. G., Evans, D. S., & Moffett, T. J. 1978, MNRAS, 183, 285

Beeckmans, F. & Hubert-Delplace, A. M. 1980, A&A, 86, 72

Benson, J. A., Hutter, D. J., Elias II, N. M., Bowers, P. F., Johnston, K. J., Hajian, A. R., Armstrong, J. T., Mozurkewich, D., Pauls, T. A., Rickard, L. J., Hummel, C. A., White, N. M., Black, D., & Denison, C. S. 1997, AJ, 114, 1221

Berio, P., Mourard, D., Vakili, F., Borgnino, J., & Ziad, A. 1997, JOSA A, 14, 114

Berio, P., Stee, Ph., Vakili, F., Mourard, D., Bonneau, D., Chesneau, O., Le Mignant, D., Thureau, N., & Hirata, R. 1999, A&A, 345, 203

Bjorkman, J. E. & Cassinelli, J. P. 1993, ApJ, 409, 429

Bjorkman, J. 2000, in *The Be Phenomenon in Early Type Stars*, eds. M. A. Smith, H. F. Henrichs, & J. Fabregat, ASP Conf. Ser., 214, IAU Colloq., 175, 435

Bjorkman, K. S., Miroshnichenko, A. S., McDavid, D., & Pogrosheva, T. M. 2002, ApJ, 573, 812

Böhm-Vitense, E. 1981, ARA&A, 19, 295

Born, M. & Wolf, E. 1999, Principles of Optics : Electromagnetic Theory of Propagation, Interference and Diffraction of Light 7th ed. (Cambridge: Cambridge University Press)

Božić, H., Harmanec, P., Yang, S., Žižňovský, J., Percy, J. R., Ruždjak, D., Sudar, D., Šlechta, M., Škoda, P., Krpata, J., & Buil, C. 2004, A&A, 416, 669

Bracewell, R. N. 2000, The Fourier Transform and its Applications 3rd ed. (Boston : McGraw Hill)

Brown, J. C. & McLean, I. S. 1977, A&A, 57, 141

Castle, K. G. 1977, PASP, 89, 862

Coté, J., & Waters, L. B. F. M. 1987, A&A, 176, 93

Cote, J. & van Kerkwijk, M. H. 1993, A&A, 274, 870

Cowley, A. P. & Marlborough, J. M. 1968, PASP, 80, 42

Dachs, J., Hanuschik, R., Kaiser, D., & Rohe, D. 1986, A&A, 159, 276

Doazan, V. 1982, in *B Stars With and Without Emission Lines*, ed A.B. Underhill, V. Doazan (NASA SP-456) (Washington: NASA), 370

Domiciano de Souza, A., Kervella, P., Jankov, S., Abe, L., Vakili, F., di Folco, E., & Paresce, F. 2003, A&A, 407, L47

ESA 1997, The Hipparcos and Tycho Catalogues, (ESA SP-1200) (Noordwijk:ESA)

Fabregat, J. & Torrejón, J. M. 2000, A&A, 357, 451

FitzGerald, M. P. 1970, A&A, 4, 234

Floquet, M., Hubert, A. M., Chauville, J., Chatzichristou, H., & Maillard, J. P. 1989, A&A, 214, 295

Garcia, B. 1989, Bulletin d'Information du Centre de Donnees Stellaires, 36, 27

Gies, D. R. 2000, in *The Be Phenomenon in Early Type Stars*, eds. M. A. Smith, H. F. Henrichs, & J. Fabregat, ASP Conf. Ser., 214, IAU Colloq., 175, 668

Gilbreath, G. C., Pauls, T. A., Armstrong, J. T., Mozurkewich, D., Benson, J. A., Hindsley, R. B., & Driscoll, D. 2003, in *Interferometry for Optical Astronomy II*, W.A. Traub, ed., Proc. SPIE, 4838, 573

Gray, D. F. 1992, The Observation and Analysis of Stellar Photospheres (Cambridge: Cambridge Univ. Press)

Guo, Y., Huang, L., Hao, J., Cao, H., Guo, Z., & Guo, X. 1995, A&AS, 112, 201

Hajian, A.R., Armstrong, J.A., Hummel, C.A., Benson, J.A., Mozurkewich, D., Pauls, T.A., Hutter, D.J., Elias II, N.M., Johnston, K.J., Rickard, L.J, & White, N.M. 1998, ApJ, 496, 484.

Hall, J. C., Fulton, E. E., Huenemoerder, D. P., Welty, A. D., & Neff, J. E. 1994, PASP, 106, 315

Hanuschik, R. W. 1986, A&A, 166, 185

Hanuschik, R. W. 1987, A&A, 173, 299

Hanuschik, R. W., Kozok, J. R., & Kaiser, D. 1988, A&A, 189, 147

Hanuschik, R. W., Hummel, W., Dietle, O., & Sutorius, E. 1995, A&A, 300, 163

Hanuschik, R. W. 1996, A&A, 308, 170

Hanuschik, R. W., Hummel, W., Sutorius, E., Dietle, O., & Thimm, G. 1996, A&AS, 116, 309

Harmanec, P. 1984, Bulletin of the Astronomical Institutes of Czechoslovakia, 35, 164

Hoffleit, D. & Jaschek, C. 1982, The Bright Star Catalogue, New Haven: Yale University Observatory (4th edition)

Horaguchi, T., Kogure, T., Hirata, R., Kawai, N., Matsuoka, M., Murakami, T., Doazan, V., Slettebak, A., Huang, C. C., Cao, H., Guo, Z., Huang, L., Tsujita, J., Ohshima, O., & Ito, Y. 1994, PASJ, 46, 9

Horne, K. & Marsh, T. R. 1986, MNRAS, 218, 761

Huang, S. 1972, ApJ, 171, 549

Huang, S. S. 1973, ApJ, 183, 541

Hummel, C.A., Mozurkewich, D., Armstrong, J.T., Hajian, A.R., Elias II, N.M., & Hutter, D.J. 1998, AJ, 116, 2536.

Hummel, C. A., Benson, J. A., Hutter, D. J., Johnston, K. J., Mozurkewich, D., Armstrong, J. T., Hindsley, R. B., Gilbreath, G. C., Rickard, L. J., & White, N. M. 2003, AJ, 125, 2630

Hummel, W. & Dachs, J. 1992, A&A, 262, L17

Hummel, W. 1994, A&A, 289, 458

Hummel, W. & Vrancken, M. 1995, A&A, 302, 751

Hummel, W. & Vrancken, M. 2000, A&A, 359, 1075

Jackson, J. D. 1999 Classical Electrodynamics 3 rd ed. (New York: John Wiley & Sons)

Jarad, M. M. 1987, Ap&SS, 139, 83

Johnson, H. L. 1966, ARA&A, 4, 193

Johnson, H. L., Iriarte, B., Mitchell, R. I., & Wisniewski, W. Z. 1966, Communications of the Lunar and Planetary Laboratory, 4, 99

Johnson, H. L., Wiśniewski, W. Z., & Faÿ, T. D. 1978, Rev. Mexicana Astron. Astrofis., 2, 273

Kato, S. 1983, PASJ, 35, 249

Kříž , S. 1979, Bulletin of the Astronomical Institutes of Czechoslovakia, 30, 95

Kubo, S., Murakami, T., Ishida, M., & Corbet, R. H. D. 1998, PASJ, 50, 417

Kurucz, R. L. 1993, CD-ROM 13, Atlas9 Stellar Atmosphere Programs and 2 km/s Grid (Cambridge: SAO)

Marlborough, J. M., Snow, T. P., & Slettebak, A. 1978, ApJ, 224, 157

McDavid, D. 1999, PASP, 111, 494

Merrill, P. W. 1952, ApJ, 115, 145

Millar, C. E. & Marlborough, J. M. 1998, ApJ, 494, 715

Millar, C. E. & Marlborough, J. M. 1999a, ApJ, 516, 276

Millar, C. E. & Marlborough, J. M. 1999b, ApJ, 516, 280

Millar, C. E. & Marlborough, J. M. 1999c, ApJ, 526, 400

Millar, C. E., Sigut, T. A. A., & Marlborough, J. M. 2000, MNRAS, 312, 465

Miroshnichenko, A. S., Bjorkman, K. S., & Krugov, V. D. 2002, PASP, 114, 1226

Miroshnichenko, A. S., Bjorkman, K. S., Morrison, N. D., Wisniewski, J. P., Manset, N., Levato, H., Grosso, M., Pollmann, E., Buil, C., & Knauth, D. C. 2003, A&A, 408, 305

Monnier, J. D. 2003a, Reports on Progress in Physics, 66, 789

Monnier, J. D. 2003b, EAS Publications Series, Volume 6, 2003, Observing with the VLTI, Proceedings of the conference held 3-8 February, 2002 in Les Houches, France. Edited by G. Perrin and F. Malbet, 213

Mourard, D., Bosc, I., Labeyrie, A., Koechlin, L., & Saha, S. 1989, Nature, 342, 520

Mozurkewich, D., Armstrong, J. T., Hindsley, R. B., Quirrenbach, A., Hummel, C. A., Hutter, D. J., Johnston, K. J., Hajian, A. R., Elias II, Nicholas M., Buscher, D. F., & Simon, R. S. 2003, AJ, 126, 2502

Neiner, C., Hubert, A.-M., Frémat, Y., Floquet, M., Jankov, S., Preuss, O., Henrichs, H. F., & Zorec, J. 2003, A&A, 409, 275

Nordgren, T. E., Germain, M. E., Benson, J. A., Mozurkewich, D., Sudol, J. J., Elias II, N. M., Hajian, Arsen R., White, N. M., Hutter, D. J., Johnston, K. J., Gauss, F. S., Armstrong, J. T., Pauls, T. A., & Rickard, L. J. 1999, AJ, 118, 3032

Okazaki, A. T. 1991, PASJ, 43, 75

Okazaki, A. T. 1997, A&A, 318, 548

Okazaki, A. T., Bate, M. R., Ogilvie, G. I., & Pringle, J. E. 2002, MNRAS, 337, 967

Owocki, S. P., Cranmer, S. R., & Blondin, J. M. 1994, ApJ, 424, 887

Pauls, T. A., Gilbreath, G. C., Armstrong, J. T., Mozurkewich, D., Benson, J. A., & Hindsley, R. B. 2001, American Astronomical Society Meeting, 198, 51.16

Percy, J. R., Harlow, J., Hayhoe, K. A. W., Ivans, I. I., Lister, M., Plume, R., Rosebery, T., Thompson, S., & Yeung, D. 1997, PASP, 109, 1215

Percy, J. R., Harlow, C. D. W., & Wu, A. P. S. 2004, PASP, 116, 178

Poeckert, R., & Marlborough, J. M. 1978, ApJ, 220, 940

Poeckert, R. & Marlborough, J. M. 1979, ApJ, 233, 259

Pols, O. R., Cote, J., Waters, L. B. F. M., & Heise, J. 1991, A&A, 241, 419

Porro, I. L., Traub, W. A., & Carleton, N. P. 1999, Appl. Opt., 38, 6055

Porter, J. M. 1996, MNRAS, 280, L31

Porter, J. M., & Rivinius, T. 2003, PASP, 115, 1153

Press, W. H., Teukolsky, S. A., Vetterling, W. T., & Flannery, B. P. 1992, Numerical Recipes in C (2d ed.; Cambridge: University Press)

Prinja, R. K. 1989, MNRAS, 241, 721

Quirrenbach, A., Hummel, C. A., Buscher, D. F., Armstrong, J. T., Mozurkewich, D., & Elias, N. M. 1993, ApJ, 416, L25

Quirrenbach, A., Buscher, D. F., Mozurkewich, D., Hummel, C. A., & Armstrong, J. T. 1994, A&A, 283, L13

Quirrenbach, A., Bjorkman, K. S., Bjorkman, J. E., Hummel, C. A., Buscher, D. F., Armstrong, J. T., Mozurkewich, D., Elias II, N. M., & Babler, B. L. 1997, ApJ, 479, 477

Quirrenbach, A. 2001, ARA&A, 39, 353

Riboni, E., Poretti, E., & Galli, G. 1994, A&AS, 108, 55

Rivinius, Th., Baade, D., Štefl, S., Stahl, O., Wolf, B., & Kaufer, A. 1998a, A&A, 333, 125

Rivinius, Th., Baade, D., Štefl, S., Stahl, O., Wolf, B., & Kaufer, A. 1998b, in Cyclical variability in stellar winds, ed. L. Kaper, & A. Fullerton, ESO Conf. Ser., 207

Rivinius, Th., Baade, D., Štefl, S., & Maintz, M. 2001, A&A, 379, 257

Rivinius, Th., Baade, D., & Štefl, S. 2003, A&A, 411, 229

Saad, S. M., Kubát, J., Koubský, P., Harmanec, P., Škoda, P., Korčáková, D., Krtička, J., Šlechta, M., Božić, H., Ak, H., Hadrava, P., & Votruba, V. 2004, A&A, 419, 607

Schild, R. E. 1978, ApJS, 37, 77

Schild, R. E. 1983, A&A, 120, 223

Schultz, G. V. & Wiemer, W. 1975, A&A, 43, 133

Secchi, A. 1867, Astronomische Nachrichten, 68, 63

Shao, M., & Staelin, D.H. 1980, Appl. Opt., 19, 1519

Shao, M., Colavita, M., Staelin, D. H., Johnston, K. J., Simon, R. S., Hughes, J. A., & Hershey, J. L. 1987, AJ, 93, 1280

Shao, M., Colavita, M. M., Hines, B. E., Staelin, D. H., & Hutter, D. J. 1988, A&A, 193, 357

Shao, M. & Colavita, M. M. 1992, ARA&A, 30, 457

Slettebak, A. 1982, ApJS, 50, 55

Slettebak, A. 1987, IAU Colloq. 92: Physics of Be Stars, 24

Slettebak, A., Collins, G. W., & Truax, R. 1992, ApJS, 81, 335

Smith, M. A. 1995, ApJ, 442, 812

Snow, T. P. 1981, ApJ, 251, 139

Stee, P., de Araujo, F. X., Vakili, F., Mourard, D., Arnold, L., Bonneau, D., Morand, F., & Tallon-Bosc, I. 1995, A&A, 300, 219

Stee, P., Vakili, F., Bonneau, D., & Mourard, D. 1998, A&A, 332, 268

Stee, P. & Bittar, J. 2001, A&A, 367, 532

Struve, O. 1931, ApJ, 73, 94

Tango, W. J. & Twiss, R. Q. 1980, Progress in optics. Volume, 17, 239

Taylor, A. R., Dougherty, S. M., Waters, L. B. F. M., & Bjorkman, K. S. 1990, A&A, 231, 453

Telting, J. H., Waters, L. B. F. M., Persi, P., & Dunlop, S. R. 1993, A&A, 270, 355

Telting, J. H. & Kaper, L. 1994, A&A, 284, 515

Thom, C., Granes, P., & Vakili, F. 1986, A&A, 165, L13

Thompson, A.R., Moran, J.M., & Swenson, G.W. 2001, Interferometry and Synthesis in Radio Astronomy 2nd ed. (New York: John Wiley & Sons)

Torres-Dodgen, A. V. & Weaver, W. B. 1993, PASP, 105, 693

Townsend, R. H. D., Owocki, S. P., & Howarth, I. D. 2004, MNRAS, 350, 189

Traub, W. A. 1999, in *Principles of Long Baseline Stellar Interferometry*, Course Notes from the 1999 Michelson Summer School held at the CALTECH in Pasadena, California, Editor Peter R. Lawson, 31

Tycner, C., Hajian, A. R., Mozurkewich, D., Armstrong, J. T., Benson, J. A., Gilbreath, G. C., Hutter, D. J., Pauls, T. A., & Lester, J. B. 2003, AJ, 125, 3378

Tycner, C., Hajian, A. R., Armstrong, J. T., Benson, J. A., Gilbreath, G. C., Hutter, D. J., Lester, J. B., Mozurkewich, D., & Pauls, T. A. 2004, AJ, 127, 1194

Underhill, A. B., Divan, L., Prevot-Burnichon, M.-L., & Doazan, V. 1979, MNRAS, 189, 601

Vakili, F., Mourard, D., Stee, Ph., Bonneau, D., Berio, P., Chesneau, O., Thureau, N., Morand, F., Labeyrie, A., & Tallon-Bosc, I. 1998, A&A, 335, 261

van Belle, G. T. 1999, PASP, 111, 1515

van Kerkwijk, M. H., Waters, L. B. F. M., & Marlborough, J. M. 1995, A&A, 300, 259

Waters, L.B.F.M. 1986, A&A, 162, 121

Wood, K., Bjorkman, K. S., & Bjorkman, J. E. 1997, ApJ, 477, 926

Zhang, F., Li, X.-D., & Wang, Z.-R. 2004, ApJ, 603, 663